



AFRL-OSR-VA-TR-2015-0034

A MULTI--SCALE FRAMEWORK FOR MULTI--FIELD ANALYSES OF SMART COMPOS

Anastasia Muliana
TEXAS ENGINEERING EXPERIMENT STATION COLLEGE STATION

01/15/2015
Final Report

DISTRIBUTION A: Distribution approved for public release.

Air Force Research Laboratory
AF Office Of Scientific Research (AFOSR)/ RTA
Arlington, Virginia 22203
Air Force Materiel Command

| | | | | | | | | | | | | |
|---|--------------|--|--|--|---|--------------|--------------|--------------|--|--|----------------------------------|--|
| REPORT DOCUMENTATION PAGE | | | | | Form Approved OMB No. 0704-0188 | | | | | | | |
| <p>The public reporting burden for this collection of information is estimated to average 1 hour per response, including the time for reviewing instructions, searching existing data sources, gathering and maintaining the data needed, and completing and reviewing the collection of information. Send comments regarding this burden estimate or any other aspect of this collection of information, including suggestions for reducing the burden, to the Department of Defense, Executive Service Directorate (0704-0188). Respondents should be aware that notwithstanding any other provision of law, no person shall be subject to any penalty for failing to comply with a collection of information if it does not display a currently valid OMB control number.</p> <p>PLEASE DO NOT RETURN YOUR FORM TO THE ABOVE ORGANIZATION.</p> | | | | | | | | | | | | |
| 1. REPORT DATE (DD-MM-YYYY) 10-01-2015 | | 2. REPORT TYPE Final Project | | | 3. DATES COVERED (From - To) Oct 15, 2009-Oct 14 2014 | | | | | | | |
| 4. TITLE AND SUBTITLE AFOSR PECASE Grant A multi-scale framework for multi-field analyses of smart composites | | | | 5a. CONTRACT NUMBER C09-00916 | | | | | | | | |
| | | | | 5b. GRANT NUMBER FA 9550-10-1-0002 | | | | | | | | |
| | | | | 5c. PROGRAM ELEMENT NUMBER N/A | | | | | | | | |
| 6. AUTHOR(S) Anastasia Hanifah Muliana | | | | 5d. PROJECT NUMBER A8460 | | | | | | | | |
| | | | | 5e. TASK NUMBER N/A | | | | | | | | |
| | | | | 5f. WORK UNIT NUMBER N/A | | | | | | | | |
| 7. PERFORMING ORGANIZATION NAME(S) AND ADDRESS(ES) Texas Engineering Experiment Station 1470 William D. Fitch Parkway College Station, TX 77843-4645 | | | | | 8. PERFORMING ORGANIZATION REPORT NUMBER | | | | | | | |
| 9. SPONSORING/MONITORING AGENCY NAME(S) AND ADDRESS(ES) Air Force Office of Scientific Research, Program Manager: Dr. David Stargel 801 N Randolph St., Rm. 732, Arlington VA 22203, United States | | | | | 10. SPONSOR/MONITOR'S ACRONYM(S) US AFOSR | | | | | | | |
| | | | | | 11. SPONSOR/MONITOR'S REPORT NUMBER(S) N/A | | | | | | | |
| 12. DISTRIBUTION/AVAILABILITY STATEMENT Approved for public release distribution unlimited DISTRIBUTION A | | | | | | | | | | | | |
| 13. SUPPLEMENTARY NOTES N/A | | | | | | | | | | | | |
| 14. ABSTRACT Smart composites comprising of electro-active components, are appealing for multifunctional systems with the ability to respond to various external stimuli, such as morphing structures. The differences in the responses of the constituents in the smart composites, together with various microstructural morphologies will have significant effects on the overall performance of multifunctional morphing systems. This project is aimed at understanding the effect of coupled thermal, electrical, and mechanical responses, including loading rate (time) effect, of the constituents (piezoelectric ceramics and polymers) on the overall multi-field responses of electro-active composites. For this purpose, a multi-scale framework that consists of constitutive models for the constituents incorporating field coupling and time-dependent effects; nonlinear micromechanical models for various composite reinforcements including functionally graded composites; and large scale multifunctional structural analyses is formulated. Limited experiments are conducted in order to study the effect of microstructural morphologies on the overall multi-field response of composites. The multi-scale model is able to predict the overall performance and perform active controls of smart structures under external stimuli. | | | | | | | | | | | | |
| 15. SUBJECT TERMS nonlinear electro-active, viscoelasticity, active composites, micromechanics, multi-scale, finite-element | | | | | | | | | | | | |
| 16. SECURITY CLASSIFICATION OF: <table border="1" style="width: 100%; border-collapse: collapse;"> <tr> <td style="width: 33%; padding: 2px;">a. REPORT</td> <td style="width: 33%; padding: 2px;">b. ABSTRACT</td> <td style="width: 33%; padding: 2px;">c. THIS PAGE</td> </tr> <tr> <td style="text-align: center; padding: 2px;">unclassified</td> <td style="text-align: center; padding: 2px;">unclassified</td> <td style="text-align: center; padding: 2px;">unclassified</td> </tr> </table> | | | a. REPORT | b. ABSTRACT | c. THIS PAGE | unclassified | unclassified | unclassified | 17. LIMITATION OF ABSTRACT SAR | | 18. NUMBER OF PAGES 84 | |
| a. REPORT | b. ABSTRACT | c. THIS PAGE | | | | | | | | | | |
| unclassified | unclassified | unclassified | | | | | | | | | | |
| | | | 19a. NAME OF RESPONSIBLE PERSON Anastasia Muliana | | | | | | | | | |
| | | | 19b. TELEPHONE NUMBER (Include area code) 979-458-3579 | | | | | | | | | |

Reset

Final Project Report

AFOSR PECASE Grant

A multi-scale framework for multi-field analyses of smart
composites

PI: Anastasia Muliana

Department of Mechanical Engineering,
Texas A&M University
College Station, TX 77843

January 10, 2015

1) Abstract

Smart composites comprising of electro-active components are appealing for multifunctional systems with the ability to respond to various external stimuli, such as morphing structures. Piezocomposites having piezoelectric ceramics and polymers are promising for morphing structures. The electro-mechanical performances of piezoelectric ceramics and polymers are nonlinear and time-dependent, which are significantly affected by temperatures. The differences in the responses of piezoelectric ceramics and polymers, together with various microstructural morphologies will have significant effects on the overall performance of multifunctional morphing systems.

This project is aimed at understanding the effect of coupled thermal, electrical, and mechanical responses, including loading rate (time) effect, of the constituents (piezoelectric ceramics and polymers) on the overall multi-field responses of electro-active composites. For this purpose, a multi-scale framework that consists of constitutive models for the constituents incorporating field coupling and time-dependent effects and heat conduction; nonlinear micromechanical models for various composite reinforcements including functionally graded composites; and large scale multifunctional structural analyses is formulated. Limited experiments on piezocomposites are conducted in order to provide useful information on the effect of microstructural morphologies on the overall multi-field response of composites. The constitutive and micromechanical models are capable in capturing the time-dependent multi-field responses of the smart composites. The multi-scale framework can predict the overall performance and perform active controls in order to achieve desired performance of the structures under various stimuli. For precisely controlling the shapes of structures, it is necessary to consider the different time-dependent behaviors of the constituents and microstructural morphologies in the active composites.

2) Table of Content

| | |
|---|----|
| 1) Abstract | 2 |
| 3) Statement of Problem Studied | 4 |
| 4) Summary of the Most Important Results | 5 |
| 4.1) Experimental Observation on the Nonlinear Time-dependent Response of Piezocomposites | 5 |
| 4.2) Nonlinear Time-dependent Constitutive Models | 8 |
| 4.3) Micromechanical Models | 20 |
| 4.4) Structural Analyses | 58 |
| 4.5) Concluding Remarks | 72 |
| 4.6) References | 74 |
| 5) Listing of Publication and Report | 78 |
| 6) List of participating scientific personnel | 84 |

3) Statement of Problem Studied

This project is aimed at understanding the effect of coupled thermal, electrical, and mechanical responses, including loading rate effect, of the constituents on the overall multi-field responses of electro-active composites. Laminated composites, having integrated piezocomposite transducers of piezoelectric ceramics fiber or particle and homogeneous matrix (polymers or metals), suitable for multifunctional morphing structures are studied. The ultimate goal is to formulate a multi-scale framework that consists of constitutive models for constituents incorporating coupled deformation, heat conduction, and piezoelectric analyses with stress, temperature, electric field, and time dependent responses; nonlinear micromechanical models for various composite reinforcements including functionally graded composites; and large scale multifunctional structural analyses. In addition to the multi-scale development, limited experiments on piezocomposites are conducted in order to study micro-scale response of the composite and provide useful insight into the effect of microstructural morphologies on the overall (macroscopic) multi-field response of composites.

The project consists of the following components:

- 1) Development of nonlinear time-dependent electro-mechanical constitutive models for the active constituent, i.e., piezoelectric ceramics, and nonlinear viscoelastic and/or viscoplastic models that incorporate the effect of temperatures and energy dissipations, which is used for the polymeric constituent. The constitutive models are derived based on a phenomenological approach within continuum mechanics.
- 2) Formulation of micromechanics models for fiber and particle composites. Different microstructural morphologies of composites are considered, which are simplified unit-cell models, composites with uniformly and randomly distributed inclusions (long fibers and solid spheres), and composites with microstructural details obtained from the scanning electron microscope. The micromechanical models are used to study the nonlinear coupled heat conduction and deformation in viscoelastic composites and nonlinear time-dependent thermo-electro-mechanical response of active composites.
- 3) Implementation of the constitutive models and micromechanical models within finite element (FE) and finite difference (FD). FE method is then used for analyzing smart composite structures/structural components undergoing coupled thermo-electro-mechanical stimuli, while incorporating detailed nonlinear and time-dependent responses of the constituents within the smart composite structures.

4) Summary of the Most Important Results

This project presents multi-scale analyses of smart composite structures that consist of electro-active materials and non-active components. The focus is on studying flexible smart composites with the ability to undergo shape changes in responses to external stimuli. The electro-active materials considered here are piezoelectric ceramics and piezoelectric composites that comprise of piezoelectric ceramics and ductile matrix, such as polymers and metals. The non-active structural components are made of fiber or particle reinforced composites. When subjected to mechanical and non-mechanical (thermal and electrical) stimuli, the smart composite structures would experience nonlinear and time-dependent coupling responses due to the different behaviors of the constituents. This project aims at integrating different nonlinear and time-dependent responses of the constituents in smart composites in order to predict the overall performance of smart structures.

4.1) Experimental Observation on the Nonlinear Time-dependent Response of Piezocomposites

Piezocomposites, comprising of long unidirectional piezoelectric ceramics fibers embedded in polymeric matrix, also known as active fiber composites (AFCs) are studied in terms of their electro-mechanical behaviors at different temperatures. The studied AFC specimens, which were purchased from Advanced Cerametrics Incorporated, consist of PZT 5A fibers dispersed in an epoxy matrix. Kapton layers and electrode fingers are placed on both surfaces of the specimens, resulting in electric field along the longitudinal fiber axis. The AFC's concept was developed by Bent (1994) and Hagood et al. (1993), which is illustrated in Fig. 1 (left). A photograph of the tested specimen is shown in Figure 1 (right).

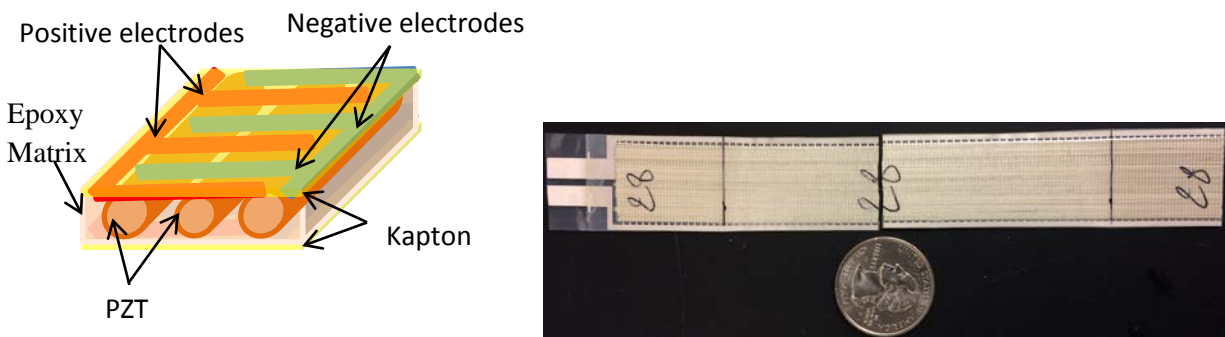


Figure 1 Microstructural representation of AFC (left) and fracture of an AFC specimen after tensile test (right)

The experimental tests are conducted in order to understand the quasi-static and hysteretic mechanical and electromechanical responses of AFC at various temperatures and loading rates (see Ben-Attitallah et al. 2014 for a discussion on experimental tests and results). First, the mechanical properties of AFCs are evaluated by applying tensile tests in the longitudinal fiber direction, at different rates and temperatures: 25°C, 50°C, and 75°C. Figure 2 shows examples of

the uniaxial stress-strain responses and Table 1 present a summary of mechanical responses, which indicate rate and temperature dependent behaviors of AFCs. The specimens are also tested under creep loadings at different stresses and temperatures, and under relaxations at various strains and temperatures. The results show significant time-dependent behaviors. Hysteretic responses of AFCs are also studied under various amplitude and frequencies of electric field input and at different temperatures. Figure 3 illustrates hysteretic polarization response of AFCs at different frequencies and temperatures. The amplitude of electric field is taken as 25 kV/cm. The responses are compared to those of pure PZT5A specimens, which shown quite different behaviors. Figure 4 presents the responses of AFCs at higher amplitude of electric field, which is 40 kV/cm. In Figs. 3 and 4, high electric fields are applied so that the piezoelectric ceramics experience polarization switching. When relatively low electric field inputs are prescribed on polarized AFCs, hysteretic electro-mechanical responses are observed, as shown in Fig. 5. The tests are also done at different temperatures and frequencies. It is seen that the mechanical, electrical, and electro-mechanical responses of AFCs depend strongly on rate of loading, temperatures, and magnitude of the mechanical and electric field inputs. Thus, in order to better understand the overall performance of active composite structures made of electro-active materials, it is necessary to include the knowledge of time-dependent and field coupling effects of the different constituents in the active structures.

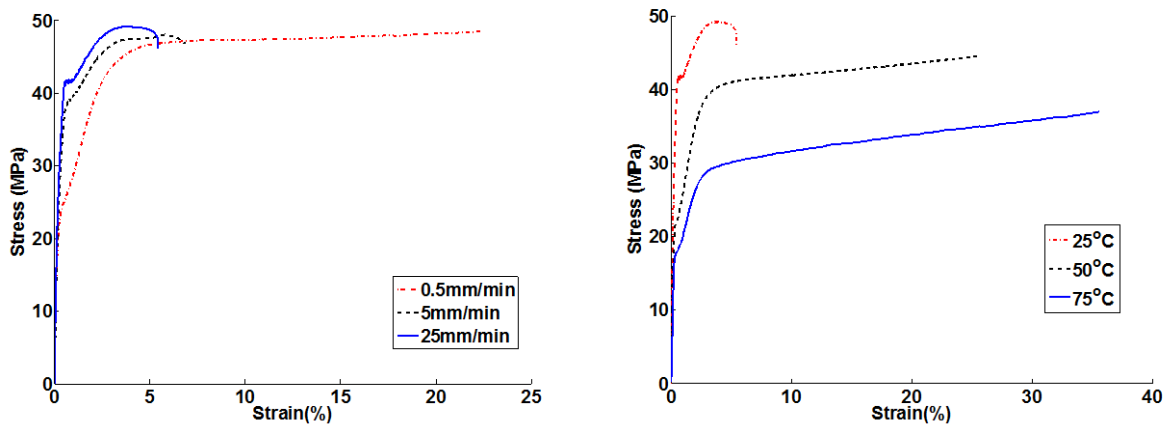


Figure 2 Uniaxial stress-strain under different rates at room temperature (left) and at different temperature and loading rate 25mm/min (right)

Table 1 Mechanical response of piezocomposites at various temperatures and high strain rate (average from 3 repeated tests)

| Displ. Rate (mm/min) | Elastic modulus (GPa) | | | Tensile strength (MPa) | | | Max strain (%) | | |
|-------------------------|-----------------------|------|------|------------------------|-------|-------|----------------|-------|-------|
| | 25°C | 50°C | 75°C | 25°C | 50°C | 75°C | 25°C | 50°C | 75°C |
| 0.5 | 9.78 | 6.25 | 5.96 | 51.29 | 44.04 | 39.90 | 17.94 | 30.94 | 34.13 |
| 5.0 | 16.58 | 7.66 | 4.05 | 43.42 | 51.13 | 44.50 | 5.37 | 21.60 | 26.24 |
| 25.0 | 16.47 | 8.49 | 6.27 | 44.68 | 47.03 | 39.15 | 4.93 | 23.80 | 36.78 |

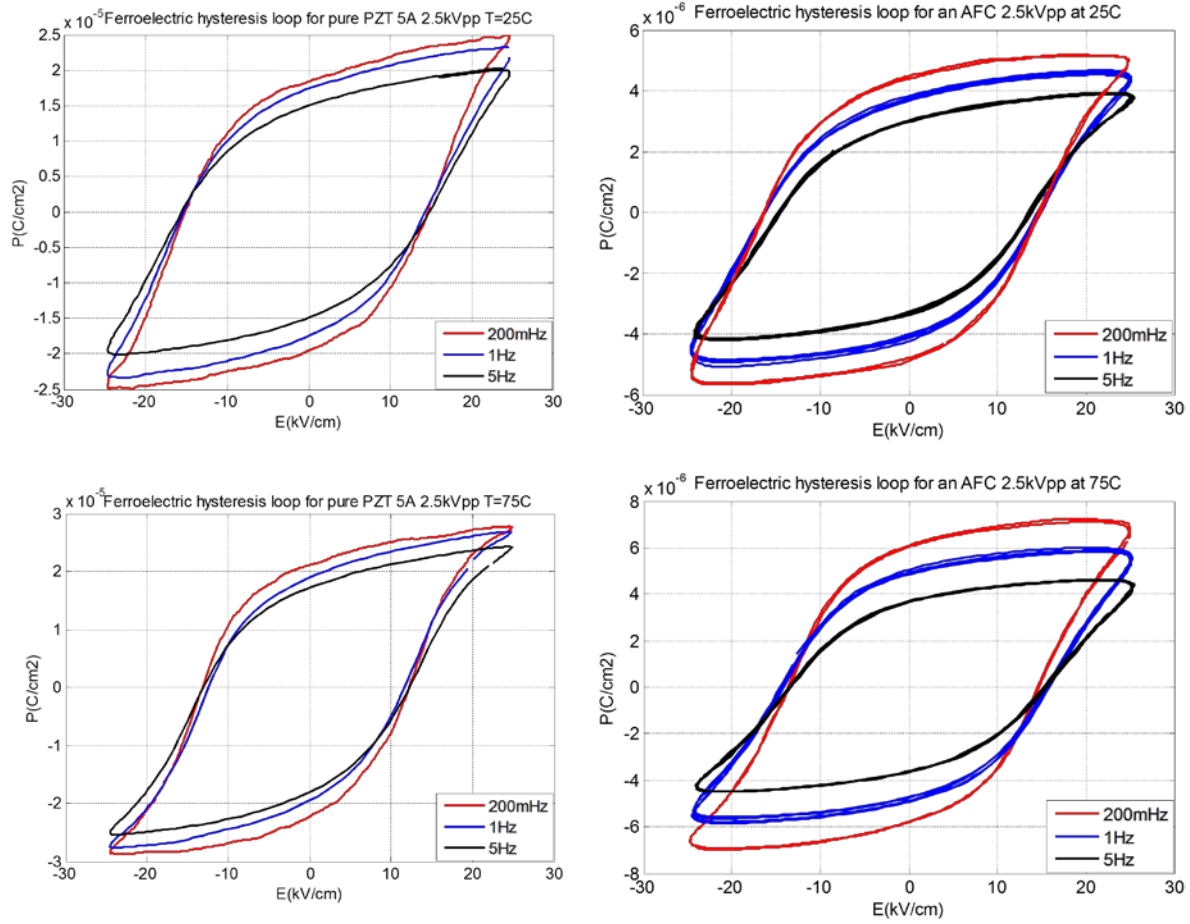


Figure 3 Hysteresis response of PZT and active fiber composites at various frequencies at temperatures 25°C and 75°C.

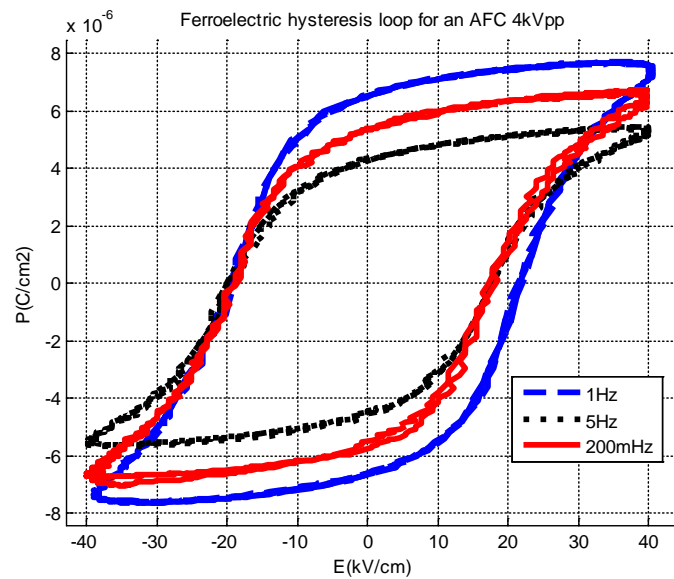


Figure 4 Hysteretic polarization at room temperature with maximum electric field 40 kV/cm

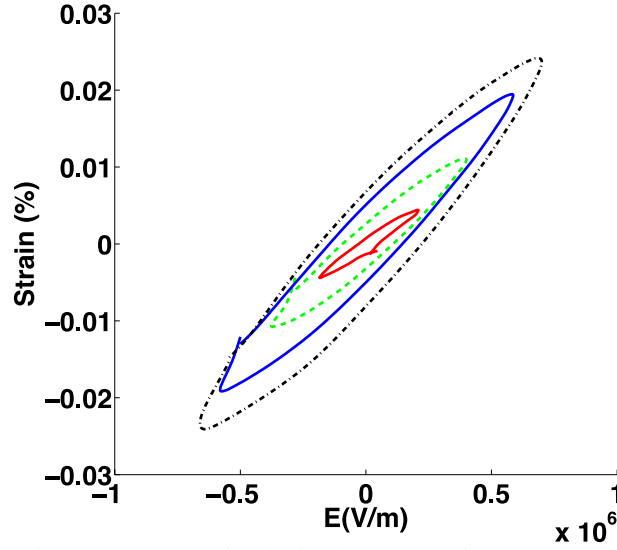


Figure 5 Electro-mechanical responses of polarized AFCs at frequency 1Hz and different amplitude of electric fields.

4.2) Nonlinear Time-dependent Constitutive Models

Polymers and piezoelectric ceramics of perovskite structures are considered in this project, and they are shown to experience nonlinear and time-dependent responses under mechanical and non-mechanical inputs, as discussed in the experimental tests above and in several literature. Nonlinear time-dependent constitutive models incorporating field coupling effects are developed for different constituents in the active composite structures. The multi-field responses of the constituents are assumed to follow general integral functions in order to incorporate histories of loading.

4.2.1 Thermo-mechanical models of polymers

In case of polymers, a nonlinear single integral model of Schapery (1969) is used to represent the viscoelastic response of polymers. The model also include the effect of temperatures and dissipation of energy that is converted into heat. The model is then extended in order to include the viscoplastic response of polymers. Linearized strain measures are considered in the model,

which are $\varepsilon_{ij} = \frac{1}{2}(u_{i,j} + u_{j,i})$, where $u_{i,j}$ is the displacement gradient. The nonlinear thermo-

viscoelastic model is given as (Muliana and Khan 2008):

$$\varepsilon_{ij}^t = g_0(\bar{\sigma}^t, T^t) D_{ijkl}^{(0)} \sigma_{kl}^t + g_1(\bar{\sigma}^t, T^t) \int_0^t dD_{ijkl} (\psi^t - \psi^s) \frac{d}{ds} (g_2(\bar{\sigma}^s, T^s) \sigma_{kl}^s) ds \quad (1)$$

where the superscript t denotes the corresponding variables at time t , D_0 and dD are the instantaneous elastic and transient compliances under a uniaxial (extensional) creep loading, respectively. The nonlinearity is incorporated through parameters g_0 , g_1 , g_2 which are functions

of current temperature T^t and the effective stress $\bar{\sigma}^t$. The reduced time ψ^t is defined as

$$\psi^t \equiv \psi(t) = \int_0^t \frac{d\xi}{a_T^\xi a_\sigma^\xi}, \text{ where the functions } a_T \text{ and } a_\sigma \text{ are the temperature- and stress dependent}$$

parameters. Using the energy equation that incorporates the viscoelastic dissipation, and stress- and temperature dependent material parameters, thermo-mechanical coupling becomes:

$$\begin{aligned} & \rho c_\sigma(T^t) \dot{T} + T^t \alpha(T^t) \dot{\sigma}_{kk}^t + T^t \frac{\partial \alpha(T^t)}{\partial T} \dot{T} \sigma_{kk}^t + T^t \frac{\partial \alpha(T^t)}{\partial T} T^t \dot{\sigma}_{kk}^t + T^t \frac{\partial g_0(\bar{\sigma}, T^t)}{\partial T} D_{ijkl}^{(0)} \dot{\sigma}_{ij}^t \sigma_{kl}^t \\ & = -q_{i,i} + g_1(\bar{\sigma}^t, T^t) \left\{ g_2(\bar{\sigma}^t, T^t) \sigma_{ij}^t - \int_0^t \sum_{m=1}^N \left[1 - \exp \left[-\lambda_m (\psi^t - \psi^\tau) \right] \right] \frac{d}{d\tau} (g_2(\bar{\sigma}^\tau, T^\tau) \sigma_{ij}^\tau) d\tau \right\} \quad (2) \\ & \quad \left(\frac{d}{dt} \int_0^t dD_{ijkl} (\psi^t - \psi^\tau) \frac{d}{d\tau} (g_2(\bar{\sigma}^\tau, T^\tau) \sigma_{kl}^\tau) d\tau \right) \end{aligned}$$

where $\alpha_{ij}(T^t)$ are the components of coefficient of thermal expansion (CTE) tensor and can depend on temperatures, ρ is the density, $c_\sigma(T^t)$ is the temperature dependent specific heat at a constant stress, and q_i is the scalar component of the heat flux. The above models are implemented within finite element, which are used to analyze coupled thermo-viscoelastic response of polymeric structures. The models are also integrated to micromechanics models and used to study fully coupled heat conduction and thermo-mechanical responses of composite structures. Detailed discussion on the model and numerical implementation are given in Khan and Muliana (2012a and b).

Figure 6 illustrates comparisons between experimental data and finite element analyses of a torsional polymeric bar under oscillations at different frequencies. The adiabatic heating is considered. It is seen that the temperature-dependent material parameters affect the heat generation in the polymeric bar due to the viscoelastic dissipation. Another example is shown on a simply supported beam subjected to a uniformly distributed load with a sinusoidal function. Three different materials are considered for the beam, which are pure polymers, particle reinforced polymers with a uniform distribution of particulate inclusions, and functionally graded materials with gradual variations of the particles in polymeric matrix. Figure 7 depicts temperature fields in the beam at two different times. Highest temperatures are generated in the polymeric beam, as expected, since the unreinforced polymer experiences a more pronounced viscoelastic behavior. Adding elastic particles to the polymers reduces the overall viscoelastic responses. Gradually varying the particle compositions can minimize the heat generations.

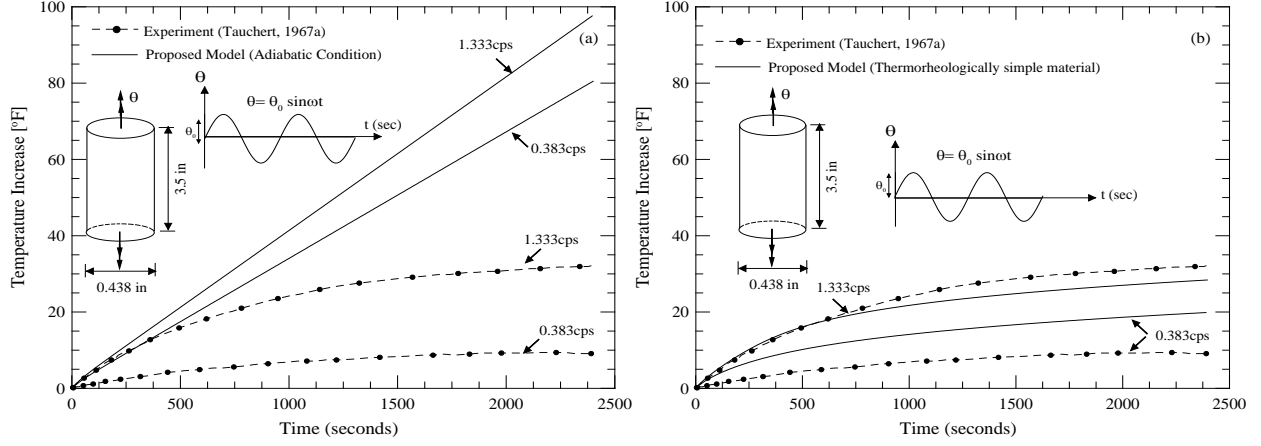


Figure 6 Comparison of experimental and finite element results under torsional oscillations at different constant frequencies and angle of twist of $\theta_0=30^\circ$: a) Adiabatic solution with temperature independent material properties, b) Adiabatic solution with temperature-dependent material properties.

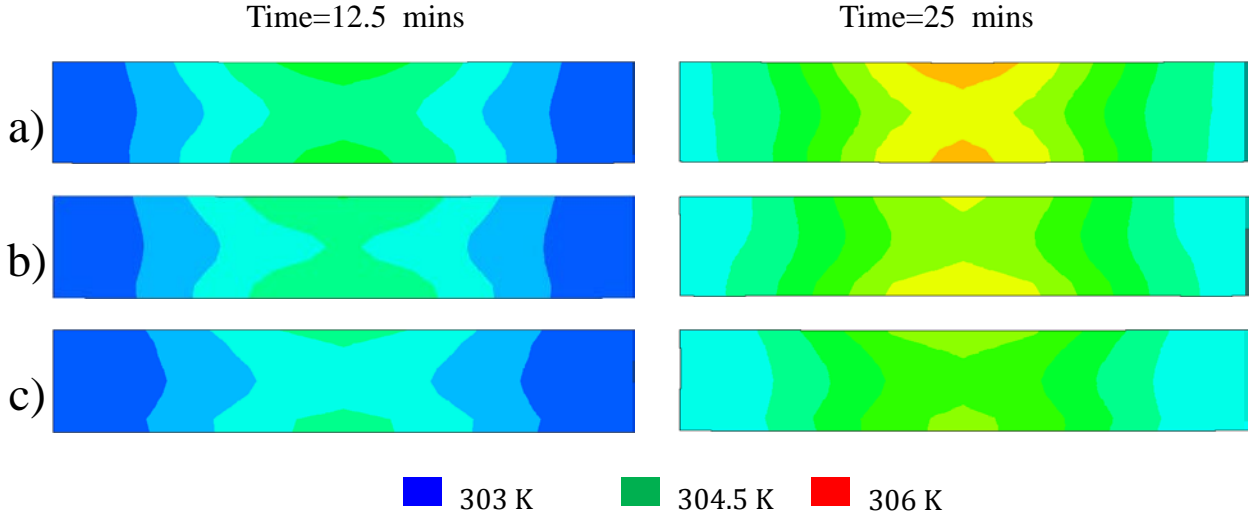


Figure 7 Temperature fields due to the dissipation effects during cyclic bending in viscoelastic beams comprising of a) homogeneous, b) composite (12.5% particle contents), and c) functionally graded material

Some polymers experience inelastic deformations when subjected to relatively large mechanical loadings, resulting in permanent deformations. In this study, the effect of inelastic deformations on the time-dependent behavior is incorporated by including the viscoplastic component. The total strain is additively decomposed into the viscoelastic and viscoplastic parts. The single integral model in Eq. (1) is used for the viscoelastic part, while the viscoplastic part follows the Perzyna (1971) model:

$$\dot{\epsilon}_{ij}^{vp,t} = \dot{\lambda}^t \frac{\partial F(\bar{\sigma}^t, k^t)}{\partial \sigma_{ij}^t} \quad (3)$$

where $\dot{\epsilon}_{ij}^{vp,t}$ is the viscoplastic strain rate at current time t and $\dot{\lambda}^t$ is the magnitude of the viscoplastic strain rate. The stress dependent yield function $F(\bar{\sigma}^t, \kappa^t)$ is expressed in terms of the

effective stress $\bar{\sigma}^t = \sqrt{\frac{3}{2} S_{ij}^t S_{ij}^t}$, where S_{ij}^t is the deviatoric stress components and the accumulated

viscoplastic strain is $\kappa^t = \int_0^t \dot{\kappa}^s ds$; $\dot{\kappa}^t = \sqrt{\frac{2}{3} \dot{\epsilon}_{ij}^{vp,t} \dot{\epsilon}_{ij}^{vp,t}}$. The normal direction at the stress point on

the yield surface F is derived as $\partial F / \partial \sigma_{ij}$ which is the direction of the viscoplastic strain rate.

Another viscoplastic model that has been considered is an endochronic viscoplastic model of Valanis (1971), which is used when the inelastic deformation occurs at relatively low stresses. The constitutive models are implemented in finite elements, which are discussed in Kim and Muliana (2010). Figures 8 and 9 illustrate the numerical results of the viscoelastic-viscoplastic models for polyethylene. Experimental data are obtained from Lai and Bakker (1995). The viscoelastic-viscoplastic model is integrated to the micromechanics models of fiber and particle reinforced polymers, which is discussed in **Section 4.3**.

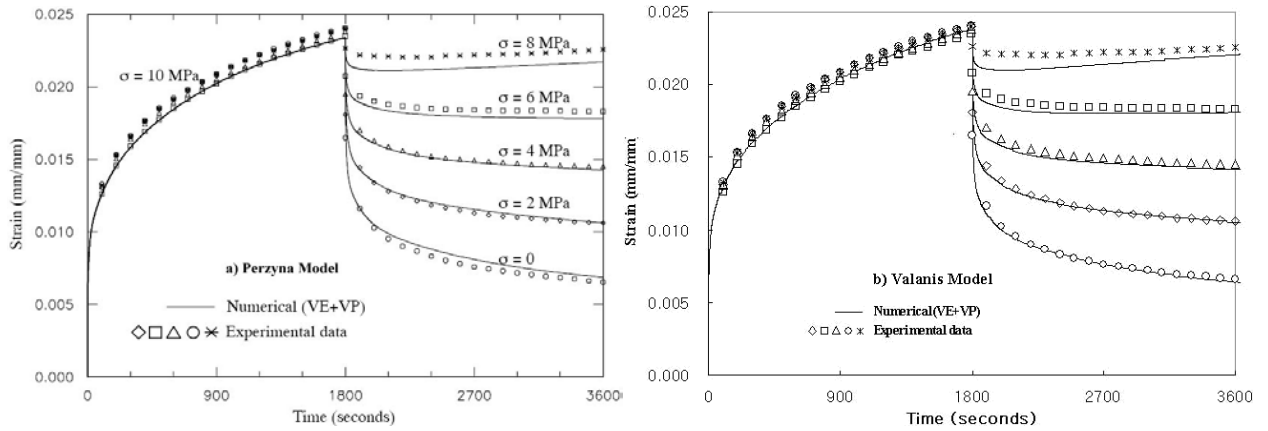


Figure 8 Strain responses under two strep loadings

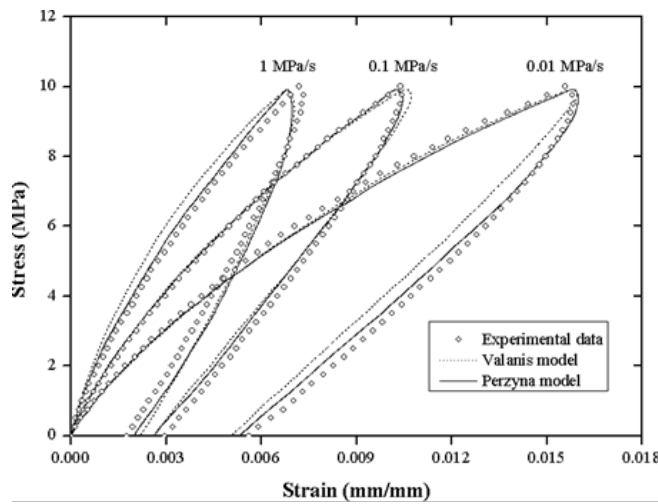


Figure 9 Stress-strain under different rates

4.2.2 Electro-mechanical models for piezoelectric ceramics

The piezoelectric ceramics considered here are of perovskite structures. Each crystallite within the polycrystalline structures can undergo spontaneous polarization, which is categorized as ferroelectric materials (see Lines and Glass 2009). Several available experimental data on lead zirconate titanate (PZT) and barium titanate shows nonlinear and time-dependent electro-mechanical responses, e.g., Crawley and Anderson (1990), Fang and Li (1999), Zhou and Kamlah (2006). The nonlinearity becomes significant under high electric field inputs, and the piezoelectric ceramics experience polarization switching when high electric fields above the coercive limit are prescribed. Nonlinear electro-mechanical constitutive models for piezoelectric ceramics incorporating time-(rate-)dependent effect are formulated for simulating responses of piezoelectric ceramics under various histories of electro-mechanical stimuli.

The rate-dependent polarization switching constitutive model for ferroelectric ceramics presented by Sohrabi and Muliana (2013) is written as:

$$\varepsilon_{ij}^t \equiv \varepsilon_{ij}(t) = s_{ijkl}\sigma_{kl}^t + 4g_{nij}^t\kappa_{nm}g_{mkl}^t\sigma_{kl}^t + 2g_{kij}^tP_k^t, \quad (4)$$

$$D_i^t = 2\kappa_{im}g_{mkl}^t\sigma_{kl}^t + P_i^t, \quad (5)$$

where the superscript t denotes the current time variable. ε_{ij}^t , σ_{ij}^t , D_i^t and P_i^t are the components of the strain, stress, electric displacement and polarization tensors at current time t , respectively. The material properties are the elastic compliance tensor s_{ijkl} determined at a constant electric field and dielectric coefficient tensor κ_{ij} calibrated at a constant stress. Here g_{ijk}^t is the scalar component of the piezoelectric coefficient, which depends on current polarization P_3^t ; x_3 direction is chosen as the poling axis. Different functions can be chosen for $g_{jk}^t(P_3^t)$ depending on the experimental data. The polarization switching is due to an application of cyclic electric field E_3^t . The macroscopic polarization P_3^t is modeled as:

$$P_3^t = R(E_3^s, t) + Q(E_3^t), \quad (1)$$

where $R(E_3^s, t)$ is the time-dependent reversible polarization at current time t with $R(0, t)=0$ while $Q(E_3^t)$ is the residual (irreversible) polarization. The reversible polarization is written as:

$$R^t = R(E_3^0, t) + \int_0^t \frac{\partial}{\partial E_3^s} R(E_3^s, t-s) \frac{dE_3^s}{ds} ds, \quad (2)$$

where

$$R(E_3^0, t) = R_0(E_3^0) + R_1(E_3^0) \left(1 - \exp\left(-\frac{t}{\tau_1}\right) \right). \quad (3)$$

Both $R_0(E_3^s)$ and $R_1(E_3^s)$ are function of E_3^s . The upper right superscript s indicates the history time variable. The characteristic time τ_1 measures the speed of the polarization changes with time. The irreversible polarization is given as:

$$Q^t = \int_0^{E_3^t} \frac{dQ^s}{dE_3^s} dE_3^s. \quad (4)$$

The rate of the residual polarization during the polarization switching response is:

$$\frac{dQ^t}{dE_3^t} = \begin{cases} 0, & 0 \leq E_3^t < E_m, dE_3^t < 0 \quad \text{or} \quad -E_m < E_3^t \leq 0, dE_3^t > 0, \\ \lambda \left| \frac{E_3^t}{E_c} \right|^n, & -E_c \leq E_3^t < 0, dE_3^t \leq 0 \quad \text{or} \quad 0 < E_3^t \leq E_c, dE_3^t \geq 0, \\ \mu \exp\left[-\omega \left(\left| \frac{E_3^t}{E_c} \right| - 1 \right)\right], & -E_m \leq E_3^t < -E_c, dE_3^t \leq 0 \quad \text{or} \quad E_c < E_3^t \leq E_m, dE_3^t \geq 0, \end{cases} \quad (5)$$

where λ , μ , ω , n are the material parameters that are calibrated from experiments. E_c and E_m are the coercive and maximum electric field, respectively. It is also necessary to define a state of polarization, which is $f(P_3^t, P_c) = (P_3^{t2} - P_c^2)$, where P_c is the current polarization state, analogous to the yield stress in the overstress plasticity theory. It is assumed that the irreversible polarization, Eq. (9) is formed when $f(P_3^t, P_c) = 0$ and $E_3^t \dot{P}_3^t > 0$. In a non-polarized sample, the current polarization state $P_c = 0$, and once the ferroelectric sample is completely polarized the current polarization state is equal to the saturated polarization ($P_c = P_s$ or $P_c = -P_s$). When the materials undergo unloading or neutral loading, $E_3^t \dot{P}_3^t \leq 0$, or loading that results in $f(P_3^t, P_c) < 0$, there is no further update on the polarization state. The other two components of polarization are expressed as $P_1^t = \kappa_{11} E_1^t$, and $P_2^t = \kappa_{22} E_2^t$.

The above constitutive equations (Eqs. (4)-(10)) are solved numerically and implemented in continuum based finite element. Discussion on the numerical algorithm can be found in Sohrabi and Muliana (2013). The electro-mechanical constitutive model in Eqs. (4) and (5) is validated using the experimental data of PZT51 reported by Fang and Li (1999). Figure 10a shows the polarization hysteretic response (D_3 - E_3) of PZT-51 subject to a cyclic electric field at zero stress. The amplitude of the electric field is 1.2 MV/m with a frequency of 1 Hz. The test started from an unpolarized condition and with increasing the electric field, polarization takes place. The loop in the first cycle is higher by about 0.03 C/m². After several cycles, the saturated polarization converges to a constant value, which shows a slightly smaller value than the one in the first cycle. The material parameters for the time-dependent polarization in are calibrated from this hysteretic polarization response. The corresponding butterfly hysteretic responses during the first and saturated cycles at zero stresses are shown in Fig. 10b. It is seen from Fig. 10b that at the coercive electric fields the strains from the experimental tests are nonzero, which is about 500 $\mu\epsilon$ higher. This might be due to the accumulated strain from the first cycle loading. In this study,

the piezoelectric constant is modeled as $g_{ijk}^t \equiv g_{ijk}(P_3^t) = \frac{P_3^t}{P_r} e^{-|P_3^t|/C_1} g_{ijk}^r$ and the parameter C_1 is

calibrated from the saturated butterfly curve in Fig. 11a after shifting the strain response obtained from the simulation 500 $\mu\epsilon$ higher. Tables 2-4 report the electro-mechanical coupling parameters and elastic constants, respectively, for PZT-51. The corresponding transverse butterfly strain response is shown in Fig. 11b. The nonlinear electro-mechanical coupling model is capable of simulating the hysteretic polarization switching electro-mechanical response. Figures 12 and 13 shows the hysteretic polarization and butterfly strain responses under cyclic electric fields and

constant compressive stresses along the electric field lines. The model is capable in capturing the nonlinear electro-mechanical responses of PZT.

Table 2 Material parameters for the time-dependent polarization of PZT-51

| E_c^o (MV/m) | κ_0 ($\times 10^{-9}$ F/m) | κ_1 ($\times 10^{-9}$ F/m) | τ_1 (sec) | λ ($\times 10^{-6}$ F/m) | n | μ ($\times 10^{-6}$ F/m) | ω |
|-------------------|---------------------------------------|---------------------------------------|-------------------|--------------------------------------|-----|----------------------------------|----------|
| 0.67* | 70 | 225 | 1.0 | 0.35 | 3.0 | 1.6 | 4 |

* from Fang and Li (1999)

Table 3 Electro-mechanical coupling parameters for PZT-51

| d_{333}^r ($\times 10^{-12}$ m/V) | d_{311}^r ($\times 10^{-12}$ m/V) | κ_{11}^r ($\times 10^{-9}$ F/m) | κ_{33}^r ($\times 10^{-9}$ F/m) | P_r (C/m ²) | C_1 |
|---|---|--|--|------------------------------|-------|
| 1520* | -570* | 38 | 42 | 0.194* | 0.19 |

* from Fang and Li (1999)

Table 4 Elastic constants for PZT-51 (Muliana 2010)

| $E_{11} = E_{22}$ | E_{33} | G_{12} (GPa) | $G_{13} = G_{23}$ | ν_{12} | $\nu_{13} = \nu_{23}$ |
|-------------------|----------|-------------------|-------------------|------------|-----------------------|
| 34.48 | 33 | 13.19 | 12.37 | 0.307 | 0.334 |

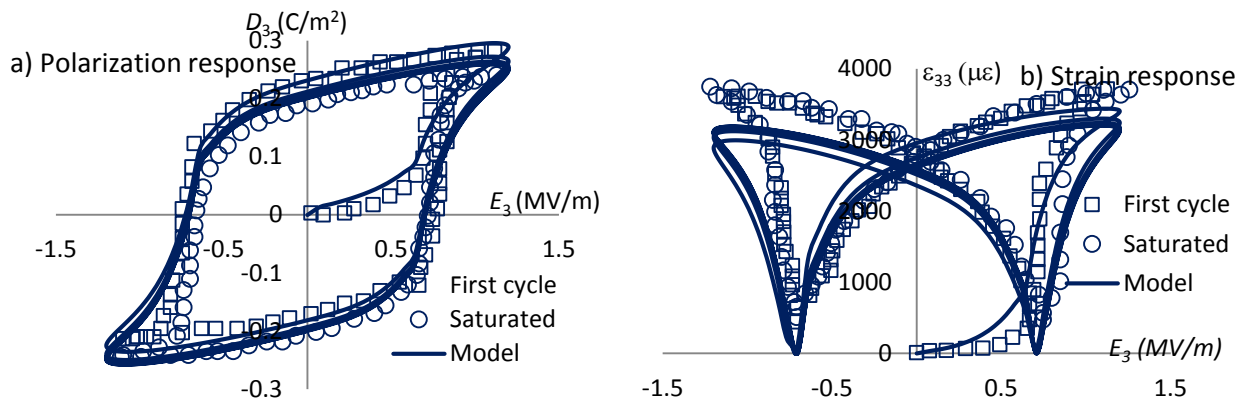


Figure 10 Hysteresis polarization and butterfly strain responses for PZT51 at zero stress

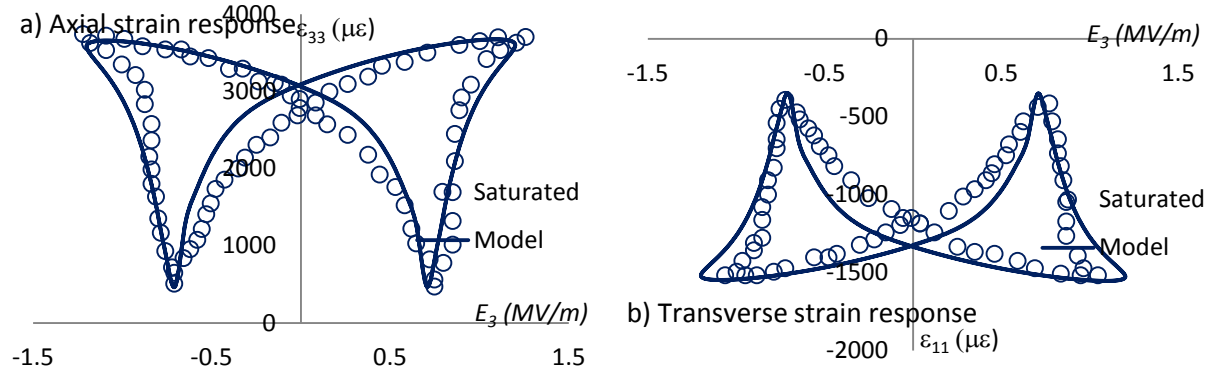


Figure 11 Saturated strain responses for PZT51 at zero stress

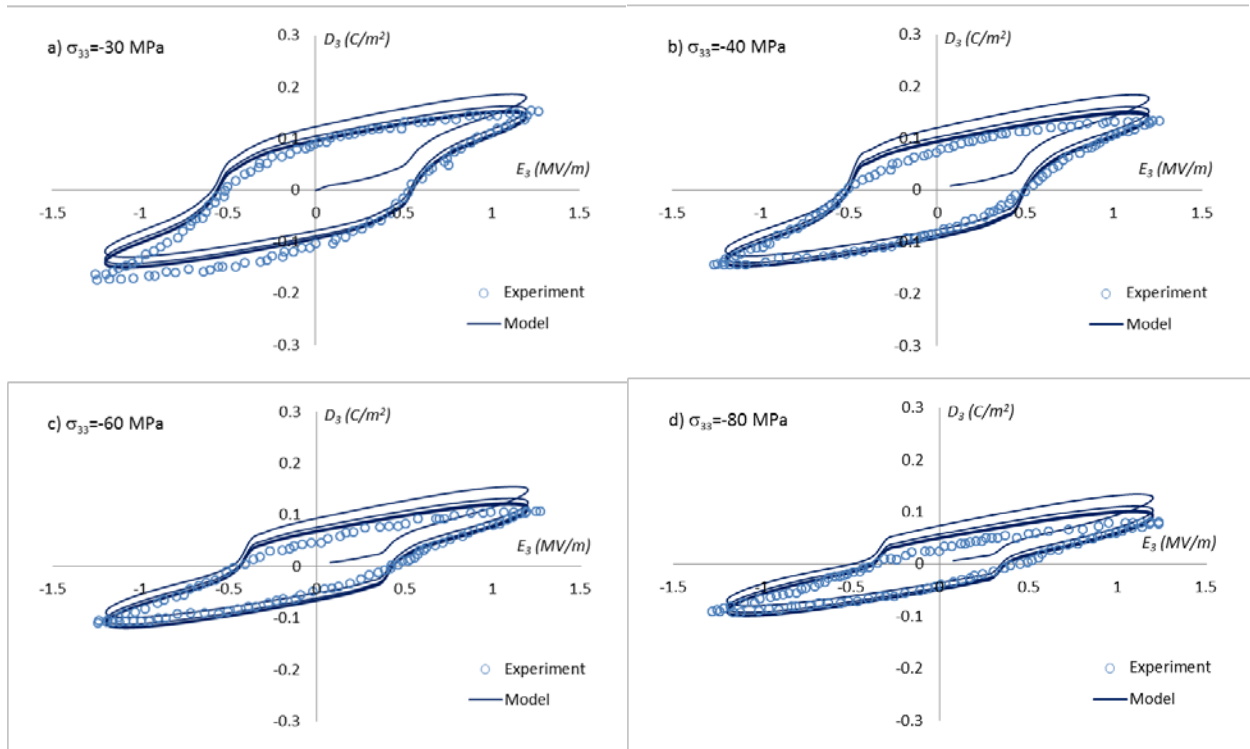


Figure 12 Hysteresis polarization responses under constant compressive stresses above the coercive stress

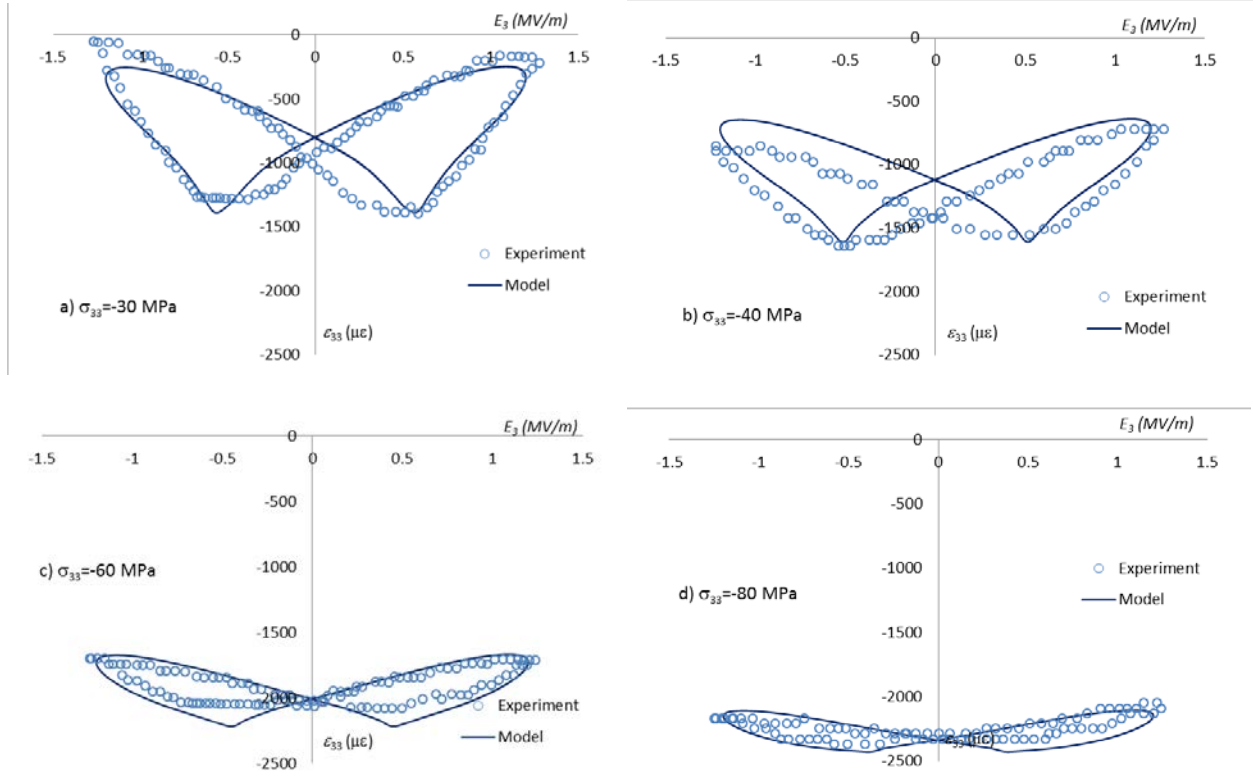


Figure 13 Butterfly strain responses under constant compressive stresses above the coercive stress

The time-dependent polarization model is extended in order to simulate polarization switching response of PZT 5A at temperatures: -75-250°C. Hooker (1998) examined the electro-mechanical properties and polarization switching response of four different PZTs at various isothermal temperatures. Experimental tests on the polarization switching response were done at frequency of 1 Hz and at amplitude of electric field of 2 MV/m. In order to determine material parameters in the time-dependent polarization model, for each available data temperature-dependent material parameters were calibrated by matching the overall polarization switching response. Thus, it is possible to have different sets of material parameters that predict the experimental data. Figure 14 illustrates the polarization switching response of PZT-5A at various isothermal temperatures. It is seen that the model is capable of capturing different shapes of the major hysteresis curves. The calibrated material parameters are given in Table 5, except for the values of E_c which are obtained from Hooker (1998).

Table 5 Material parameters for PZT-5A at various temperatures

| T (°C) | E_c (MV/m) | κ_0 ($\times 10^{-9}$ F/m) | κ_1 | τ_1 (sec) | λ ($\times 10^{-6}$ F/m) | n | μ ($\times 10^{-6}$ F/m) | ω |
|-----------|-----------------|---------------------------------------|------------|-------------------|--------------------------------------|-----|----------------------------------|----------|
| -75 | 1.41 | 10 | 10 | 1.0 | 0.12 | 2.0 | 0.12 | 3.0 |
| 0 | 1.2 | 20 | 25 | 1.0 | 0.38 | 2.0 | 0.38 | 3.0 |
| 25 | 1.15 | 20 | 35 | 1.0 | 0.58 | 2.0 | 0.58 | 3.0 |
| 100 | 1 | 30 | 55 | 0.5 | 1.10 | 4.0 | 1.10 | 5.0 |
| 250 | 0.38 | 65 | 25 | 0.1 | 2.20 | 4.0 | 2.20 | 6.0 |

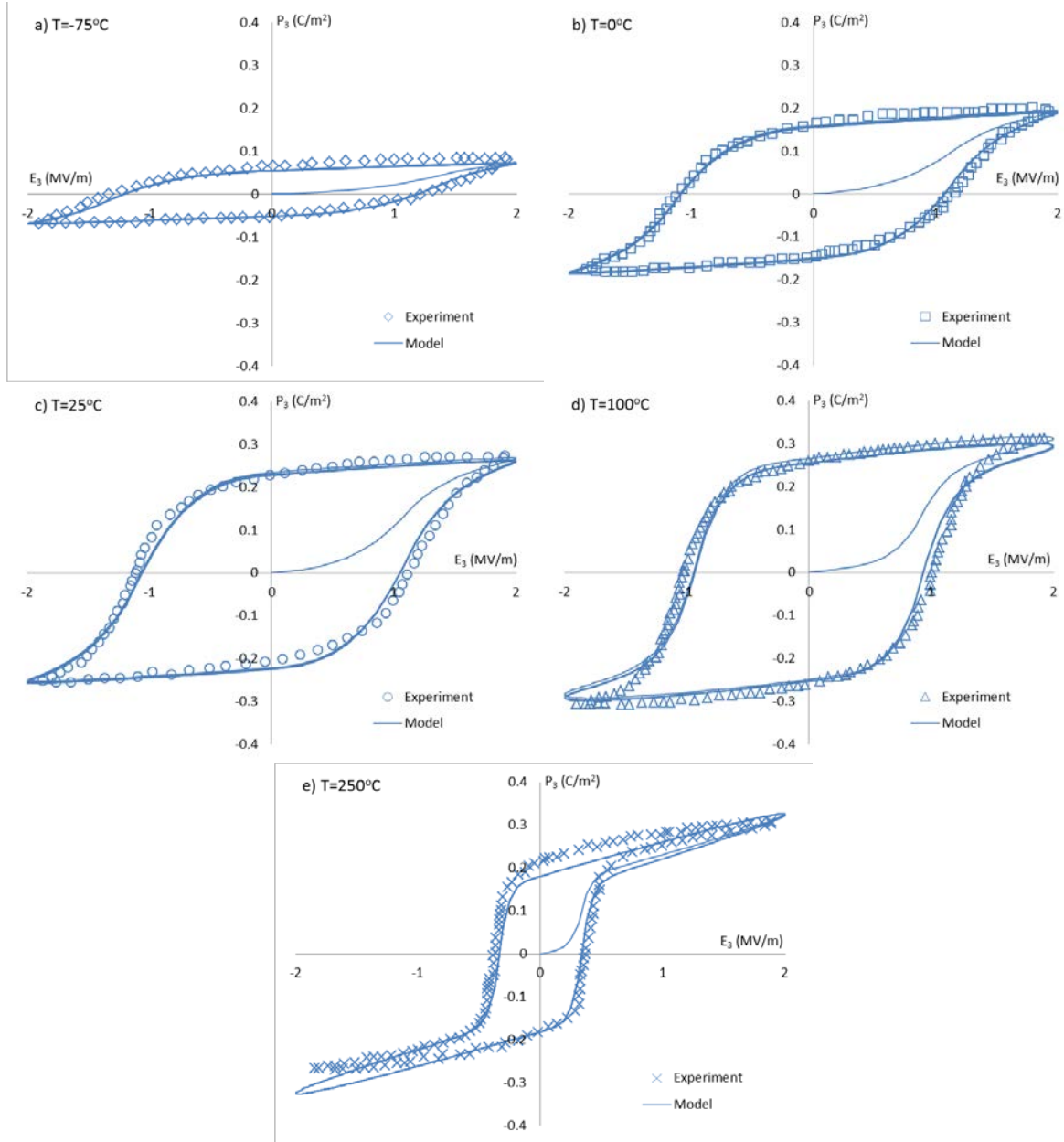


Figure 14 Temperature-dependent polarization switching response of PZT-5A (experimental data are obtained from Hooker 1998)

Another type of nonlinear electro-mechanical behavior is when the electric field input is prescribed on polarized piezoelectric materials with magnitude of electric field below the coercive electric limit of the materials. The model is represented by the reversible polarization part in Eq. (7). A single integral with a nonlinear integrand is adopted, which is written as:

$$\boldsymbol{\varepsilon}' \equiv \boldsymbol{\varepsilon}(t) = \int_0^t \frac{\partial \boldsymbol{\varepsilon}}{\partial \boldsymbol{\sigma}}(t-s, \boldsymbol{\sigma}(s)) \dot{\boldsymbol{\sigma}}(s) ds + \int_0^t \frac{\partial \boldsymbol{\varepsilon}}{\partial \mathbf{E}}(t-s, \mathbf{E}(s)) \dot{\mathbf{E}}(s) ds \quad (11)$$

$$\mathbf{D}' \equiv \mathbf{D}(t) = \int_0^t \frac{\partial \mathbf{D}}{\partial \boldsymbol{\sigma}}(t-s, \boldsymbol{\sigma}(s)) \dot{\boldsymbol{\sigma}}(s) ds + \int_0^t \frac{\partial \mathbf{D}}{\partial \mathbf{E}}(t-s, \mathbf{E}(s)) \dot{\mathbf{E}}(s) ds \quad (12)$$

Alternatively, one can also consider the following expressions:

$$\boldsymbol{\sigma}' \equiv \boldsymbol{\sigma}(t) = \int_0^t \frac{\partial \boldsymbol{\sigma}}{\partial \boldsymbol{\varepsilon}}(t-s, \boldsymbol{\varepsilon}(s)) \dot{\boldsymbol{\varepsilon}}(s) ds - \int_0^t \frac{\partial \boldsymbol{\sigma}}{\partial \mathbf{E}}(t-s, \mathbf{E}(s)) \dot{\mathbf{E}}(s) ds \quad (13)$$

$$\mathbf{D}' \equiv \mathbf{D}(t) = \int_0^t \frac{\partial \mathbf{D}}{\partial \boldsymbol{\varepsilon}}(t-s, \boldsymbol{\varepsilon}(s)) \dot{\boldsymbol{\varepsilon}}(s) ds + \int_0^t \frac{\partial \mathbf{D}}{\partial \mathbf{E}}(t-s, \mathbf{E}(s)) \dot{\mathbf{E}}(s) ds \quad (14)$$

The time-dependent kernel functions inside the above equations are determined based on experimental data on the time-dependent response of materials. In this study, a series of exponential function is used for the time-dependent kernel functions. A recursive integral model is used to solve the above integral models, which is implemented at each material point within finite elements. Detailed numerical procedures can be found in Sohrabi and Muliana (2014).

The experimental data of a piezoelectric ceramics plate reported in Crawley and Anderson (1990) are first used to validate the constitutive model. A cyclic electric field is applied through the thickness direction of the plate and the corresponding strain in the transverse direction is

measured. The strain from Eq. (11) becomes $\varepsilon_{11}(t) = \int_0^t K(t-s) \frac{\partial \varepsilon_{11}}{\partial E_3} \frac{dE_3(s)}{ds} ds$. The time kernel

function is taken as $K(t) = 1 - 0.6e^{-t/1.2}$. Linear and nonlinear functions are used for the $\frac{\partial \varepsilon_{11}}{\partial E_3}$ part,

which are $\frac{\partial \varepsilon_{11}}{\partial E_3} = d_{311}$ and $\frac{\partial \varepsilon_{11}}{\partial E_3} = d_{311} + f_{33311} E_3 E_3 E_3$, respectively. Figure 15 depicts the electro-

mechanical responses under cyclic electric field with frequency 0.1Hz at three different amplitude of electric fields, which are 250, 500, and 750 V/mm. Unlike the linear time-dependent electro-mechanical response, the nonlinear time-dependent model can capture the hysteretic electro-mechanical response of PZT.

In order to validate the finite element implementation of the nonlinear time-dependent electro-mechanical model of polarized piezoelectric ceramics, responses of piezoelectric telescopic actuators are studied. Electro-mechanical responses of two telescopic actuators reported in Alexander et al. (2001, 2003) are studied. Figure 16 presents the hysteretic axial deflection and voltage input of PZT-568 actuator. Frequency of 0.1Hz is considered in the simulation. Slight nonlinear response is shown. The electric potential and displacement fields at maximum and minimum voltages in the actuator is also shown. Another actuator, MSI-53, is considered, whose electro-mechanical response under electric field input is illustrated in Fig. 17. The response shows mainly linear hysteretic behavior, which is most likely due to relatively small voltage

applied. The contours of axial displacement and electric potential are also given in Fig. 17. Overall the time-dependent electro-mechanical model is capable in capturing the hysteretic response of piezoelectric materials and structures.

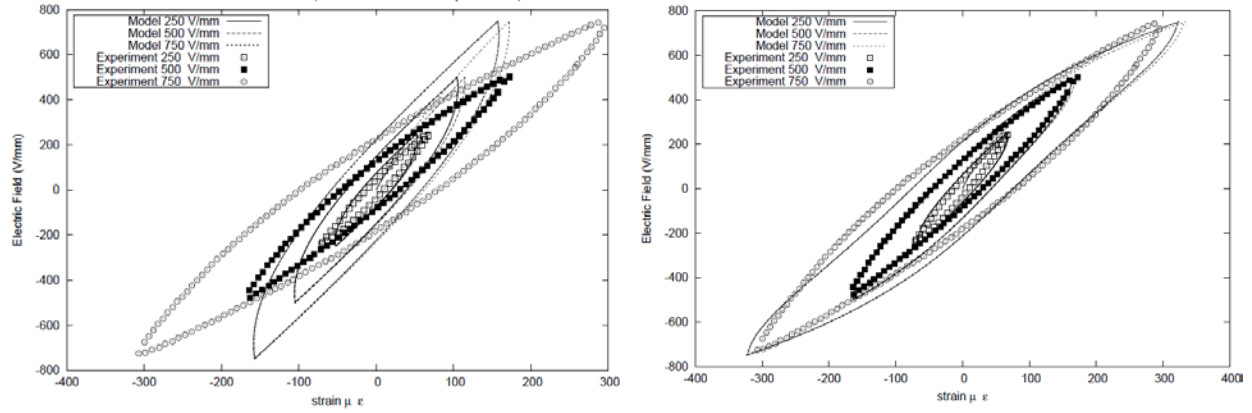


Figure 15 Linear (left) and nonlinear (right) time-dependent electro-mechanical response of PZT under cyclic electric field.

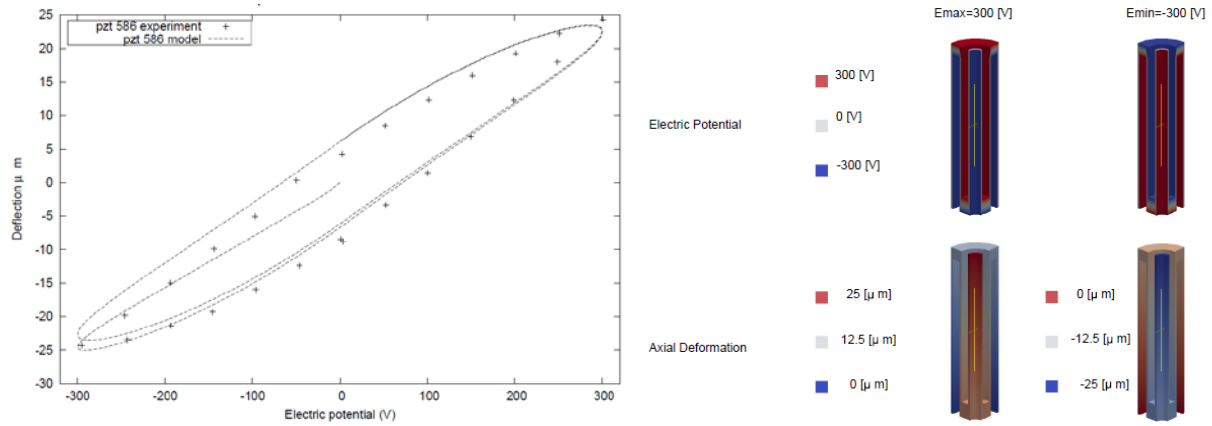


Figure 16 Electro-mechanical response of PZT-568 telescopic actuator

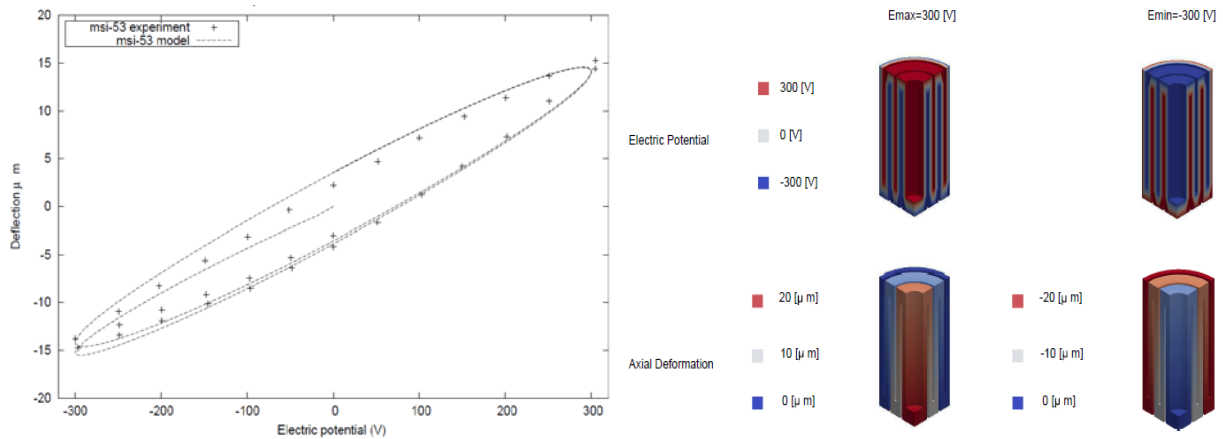


Figure 17 Electro-mechanical response of MSI-53 telescopic actuator

In order to be able to reasonably predict the overall behaviors of smart structures under various thermo-electro-mechanical stimuli, it is necessary to incorporate responses of the constituents in the smart composites. Two main constituents, which are polymers and piezoelectric ceramics, are considered for the smart composites. Since polymers and piezoelectric ceramics often experience nonlinear and time-dependent responses under various histories of thermo-electro-mechanical external stimuli, nonlinear and time-dependent constitutive models are developed for polymers and piezoelectric ceramics. The nonlinearity is considered due to high magnitude of stimuli. Numerical methods are also developed for obtaining solutions to the nonlinear and time-dependent constitutive models, which are implemented within finite elements. The constitutive models are also integrated to several micromechanical models in order to study performance of smart composites. For convenience in solving the nonlinear time-dependent constitutive equations, an incremental formulation is used and within each time increment a linearized relation is considered. The linearized relation for a thermo-electro-mechanical response is:

$$\begin{aligned}\mathbf{Z} &= \mathbf{\Omega} \mathbf{\Gamma} \\ \mathbf{\Gamma}^T &= \{\Delta \varepsilon_{11}, \Delta \varepsilon_{22}, \Delta \varepsilon_{33}, \Delta \varepsilon_{12}, \Delta \varepsilon_{12}, \Delta \varepsilon_{23}, \Delta E_1, \Delta E_2, \Delta E_3, \Delta T\} \\ \mathbf{Z}^T &= \{\Delta \sigma_{11}, \Delta \sigma_{22}, \Delta \sigma_{33}, \Delta \sigma_{12}, \Delta \sigma_{12}, \Delta \sigma_{23}, \Delta D_1, \Delta D_2, \Delta D_3, \Delta S\} \\ \mathbf{\Omega} &= \begin{bmatrix} \mathbf{C} & -\mathbf{h} & -\mathbf{\beta} \\ \mathbf{e} & \mathbf{g} & \mathbf{p} \\ \mathbf{\beta} & \mathbf{p} & C_v \end{bmatrix}\end{aligned}\tag{15}$$

where $\mathbf{\Omega}$ is the consistent tangent matrix that relate the incremental field variables. In case of nonlinear response, an iterative method is also included within the incremental formulation.

4.3) Micromechanical Models

Several micromechanical models for fiber and particulate composites are formulated in order to determine the overall (macroscopic) response of composites due to conduction of heat, thermo-mechanical inputs, and thermo-electro-mechanical stimuli. The constitutive models discussed in **Section 4.2** are implemented for the constituents in the micromechanical models. First, simplified unit-cell models are formulated for fiber and particle composites, shown in Fig. 18a and b. The simplified unit-cell models consist of several subcells. In case of fiber composites, four fiber and matrix subcells are considered, while for particle composites, there are eight subcells. Other idealized micromechanical models include detailed cylindrical fiber of circular cross-section and solid spherical particle arrangements in homogeneous matrix. Uniform and random distributions of the inclusions (fibers and particles) are considered. The overall responses determined from the unit-cell models are compared to the ones obtained from the micromechanical models with detailed fiber and particle arrangements, and also with available experimental data. The unit-cell model for particle reinforced composites is also used to study overall performance of functionally graded materials. The third micromechanical model for particle composites incorporate detailed microstructural morphologies, i.e., shapes of inclusions, pores, and distributions of inclusions in the matrix, shown in Fig. 18c. This is done to mimic more realistic microstructures and examine the effect of detailed microstructural morphologies of composites on the overall macroscopic responses of composites. In this project, perfectly bonded interfaces between inclusions and matrix are considered.

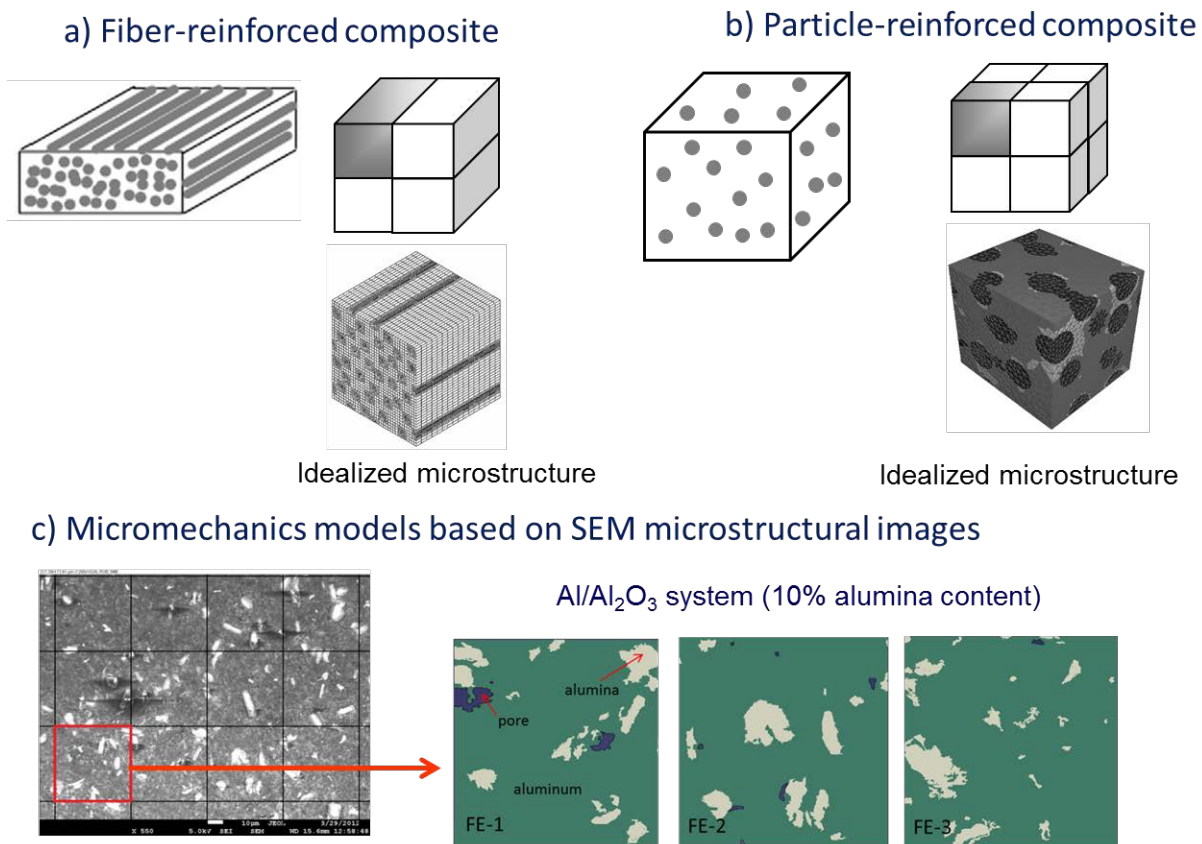


Figure 18 Several micromechanical models for composites

4.3.1) Heat conduction and deformation analyses

Micromechanical models for fiber and particle composites are formulated in order to determine the overall response of composites undergoing heat conduction and deformations. Sequentially and fully coupled heat conduction and deformation analyses are considered at multiple length scales. In the sequentially coupled analysis it is assumed that the temperature field influences the deformation field; thus, the governing equations for the conduction of heat are solved first in order to determine the temperature field in the composite bodies followed by solving the governing equations for the deformation. In the case of fully coupled thermo-mechanical analysis, the temperature field affects the deformations in the composite bodies and the dissipation of energy from the viscoelastic responses also influence the temperature field. In such situation, coupled governing equations for the heat conduction and deformation are solved concurrently at multiple length scales. It is noted that the problems considered here are under small deformation gradients, in which a linearized strain measure is considered, and the thermal and mechanical properties of the constituents are allowed to vary with temperatures, stresses, and time, leading to nonlinear responses of the composites.

The unit-cell models for fiber and particle reinforced composites are first considered in order to determine the macroscopic thermo-mechanical behaviors of homogenized composites. The unit-cell models consist of inclusion and matrix constituents, which are represented by subcells, and the nonlinear thermo-mechanical constitutive models discussed in **Section 4.2** are used for the subcells. The unit-cell models are implemented in continuum finite elements and used to study temperature and deformation fields in the homogenized composite medium. The second type micromechanical model treats heterogeneous composites explicitly. Heterogeneous composites that consist of inclusions (particles or fibers) randomly distributed in homogeneous matrix are generated using 3D continuum elements in FE framework. For each volume fraction (VF) of inclusions, the models of heterogeneous composites with different sizes of inclusions and arrangements are generated such that these models represent more realistic volume elements.

In deriving the unit-cell models, the following assumptions are made. The microstructural scale, which is represented by the unit-cells, is much smaller than the macroscopic scale so that the transient heat conduction at the microstructural scale can be neglected. Each inclusion is fully surrounded by homogeneous matrix and perfectly bonded to the matrix. In each subcell within the unit-cell, the variations of field variables are assumed uniform. The effective field variables for the unit-cell models are determined based on the volume averaging scheme (Aboudi 2005):

$$\bar{\mathbf{q}} = \frac{1}{V} \sum_{m=1}^N \int_{V^{(m)}} \mathbf{q}^{(m)}(\mathbf{x}^{(m)}) dV^{(m)} \approx \frac{1}{V} \sum_{m=1}^N V^{(m)} \mathbf{q}^{(m)} \quad (16-1)$$

$$\bar{\boldsymbol{\phi}} = \frac{1}{V} \sum_{m=1}^N \int_{V^{(m)}} \boldsymbol{\phi}^{(m)}(\mathbf{x}^{(m)}) dV^{(m)} \approx \frac{1}{V} \sum_{m=1}^N V^{(m)} \boldsymbol{\phi}^{(m)} \quad (16-2)$$

$$\bar{\boldsymbol{\sigma}} = \frac{1}{V} \sum_{m=1}^N \int_{V^{(m)}} \boldsymbol{\sigma}^{(m)}(\mathbf{x}^{(m)}) dV^{(m)} \approx \frac{1}{V} \sum_{m=1}^N V^{(m)} \boldsymbol{\sigma}^{(m)} \quad (16-3)$$

$$\bar{\boldsymbol{\varepsilon}} = \frac{1}{V} \sum_{m=1}^N \int_{V^{(m)}} \boldsymbol{\varepsilon}^{(m)}(\mathbf{x}^{(m)}) dV^{(m)} \approx \frac{1}{V} \sum_{m=1}^N V^{(m)} \boldsymbol{\varepsilon}^{(m)} \quad (16-4)$$

where \mathbf{q} , $\boldsymbol{\phi}$, $\boldsymbol{\sigma}$, and $\boldsymbol{\varepsilon}$, are the heat flux, temperature gradient, stress, and strain fields, respectively. An overbar denotes the average (macroscopic) response of the unit-cell, $V^{(m)}$ denotes the volume fraction of each subcell, the total volume fraction of the unit-cell is

$V = \sum_{m=1}^N V^{(m)}$ and N is the number of subcells. Equations (16-1)-(16-4) are exact only for linear

thermo-elastic responses of composites. Due to the nonlinear and time-dependent responses in the constituents, the solutions for the deformation fields are determined incrementally. The incremental forms of the effective field variables at the current time are $\bar{\mathbf{q}}^t = \bar{\mathbf{q}}^{t-\Delta t} + \Delta \bar{\mathbf{q}}^t$, $\bar{\boldsymbol{\phi}}^t = \bar{\boldsymbol{\phi}}^{t-\Delta t} + \Delta \bar{\boldsymbol{\phi}}^t$, $\bar{\boldsymbol{\sigma}}^t = \bar{\boldsymbol{\sigma}}^{t-\Delta t} + \Delta \bar{\boldsymbol{\sigma}}^t$ and $\bar{\boldsymbol{\varepsilon}}^t = \bar{\boldsymbol{\varepsilon}}^{t-\Delta t} + \Delta \bar{\boldsymbol{\varepsilon}}^t$. The superscript $(t-\Delta t)$ denotes previous converged solutions and the prefix Δ indicates the incremental variables within a current time increment Δt . A linearized relation is first imposed to the incremental parts of the field variables. An iterative corrector scheme is then performed in order to satisfy both the micromechanical constraints and the nonlinear constitutive equations.

The micromechanical models and constitutive equations are implemented within finite elements, in which displacement and temperature fields are defined at the nodes. Using the spatial derivatives of the shape functions, the average temperature gradient and strain are determined at

each material (Gaussian) point within finite elements. The macroscopic (average) temperature gradient and strain are related to the temperature gradient and strain in each subcell in the unit-cell models by the following relations:

$$\Delta\boldsymbol{\phi}^{(m)} = \mathbf{F}^{(m)} \Delta\bar{\boldsymbol{\phi}} \quad \text{and} \quad \Delta\boldsymbol{\epsilon}^{(m)} = \mathbf{B}^{(m)} \Delta\bar{\boldsymbol{\epsilon}} \quad (17)$$

where the second order concentration tensor $\mathbf{F}^{(m)}$ relates the temperature gradient in each subcell to the average temperature gradient of the unit-cell and the fourth order concentration tensor $\mathbf{B}^{(m)}$ relates the strain in each subcell to the average strain of the unit-cell. In order to define the concentration tensors, micromechanical relations and constitutive equations for each constituents are used, which are discussed in Muliana and Kim (2010), Muliana and Lin (2011), Khan and Muliana (2012b). Using linearized constitutive relations for the heat conduction and mechanical deformation, the relations between the micro-macro scale field variables, and the volume averaging scheme, the effective linearized constitutive relations are:

$$\Delta\bar{\mathbf{q}} \approx \frac{1}{V} \sum_{m=1}^N V^{(m)} \mathbf{k}^{(m)} \mathbf{F}^{(m)} \Delta\bar{\boldsymbol{\phi}} \quad (18-1)$$

$$\Delta\bar{\boldsymbol{\sigma}} \approx \frac{1}{V} \sum_{m=1}^N V^{(m)} \mathbf{C}^{(m)} \mathbf{B}^{(m)} \Delta\bar{\boldsymbol{\epsilon}} \quad (18-2)$$

and the effective linearized thermal conductivity and stiffness are $\bar{\mathbf{k}} \approx \frac{1}{V} \sum_{m=1}^N V^{(m)} \mathbf{k}^{(m)} \mathbf{F}^{(m)}$ and

$\bar{\mathbf{C}} \approx \frac{1}{V} \sum_{m=1}^N V^{(m)} \mathbf{C}^{(m)} \mathbf{B}^{(m)}$, respectively. It is noted that when nonlinear behaviors are considered, the linearized micromechanical models are used as trial (predictor) solutions, and an iteration is added in order to minimize residual from linearizing the nonlinear responses.

The following cases have been considered in order to examine the average (macroscopic) response of the homogenized composites obtained from the unit-cell models.

a) Heat conduction in fiber reinforced composites

The unit-cell model with four subcells that represent fiber reinforced polymer (FRP) composites is used to analyze heat conduction in composites. Experimental data available in literature are used to validate the effective thermal conductivity of fiber composites (see Muliana and Kim 2010 for a detailed discussion). Figure 19 depicts the effective thermal conductivities in the axial and transverse the fiber directions of carbon/epoxy composites. Experimental data are obtained from McIvor et al. (1990). Good predictions are observed.

Next, heat conduction behaviors obtained from the unit-cell model are compared to the ones of heterogeneous bodies incorporating detailed fiber arrangements. Figure 20 illustrates the finite element meshes for homogenized FRP and heterogeneous FRP with detailed fiber arrangements. In case of heterogeneous FRP, random and uniform fiber arrangements are considered. Figure 21 shows the temperature fields during heat conduction in the axial fiber direction for composites with 50% fiber volume content. Relatively small fiber cross-sectional area, i.e., 0.1 mm^2 , is considered in the heterogeneous FRP. Figure 22 shows the comparisons between temperature fields in the homogenized and heterogeneous FRP composites when a larger fiber cross-sectional

area is considered. The steady state time for the transient heat conduction in the axial and transverse fiber directions determined from the homogenized and heterogeneous composites with several fiber volume fractions are summarized in Table 6. The heterogeneous response is denoted by microstructural fiber (MF) model. The central processing unit (CPU) times needed to complete the heat conduction analyses to reach steady state for both models are also reported. As expected, the unit-cell model requires significantly less CPU time to complete the analyses.

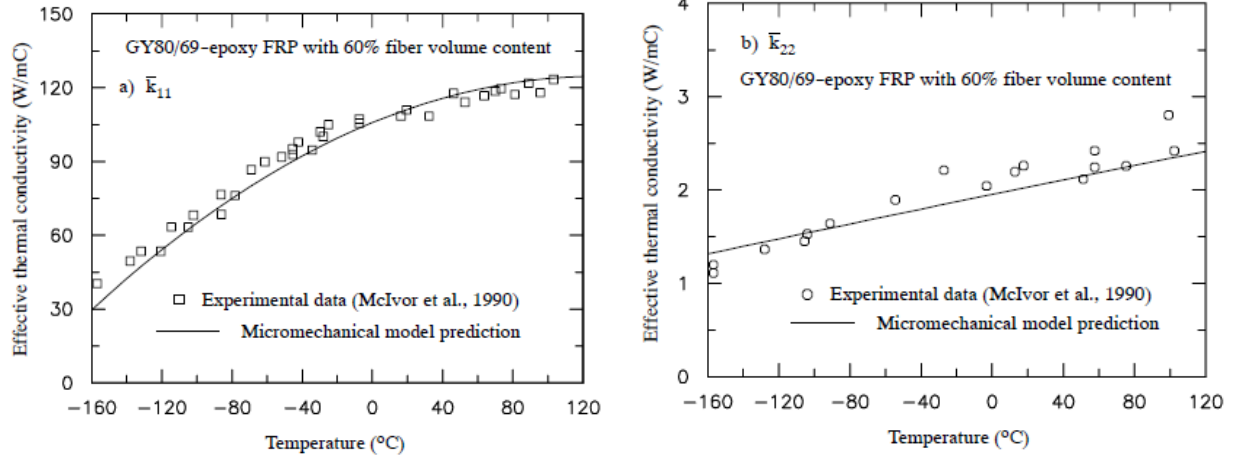


Figure 19. Temperature-dependent thermal conductivity of GY80 carbon/69epoxy

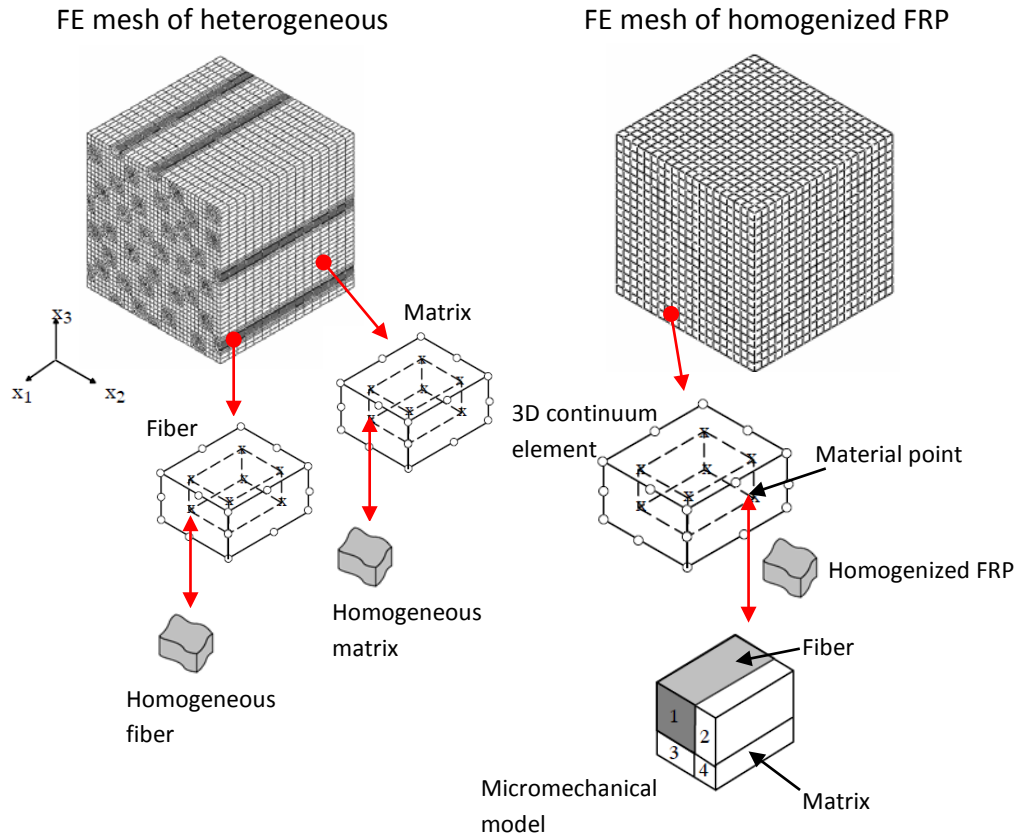


Figure 20. FE microstructures for heterogeneous and homogenized FRP systems

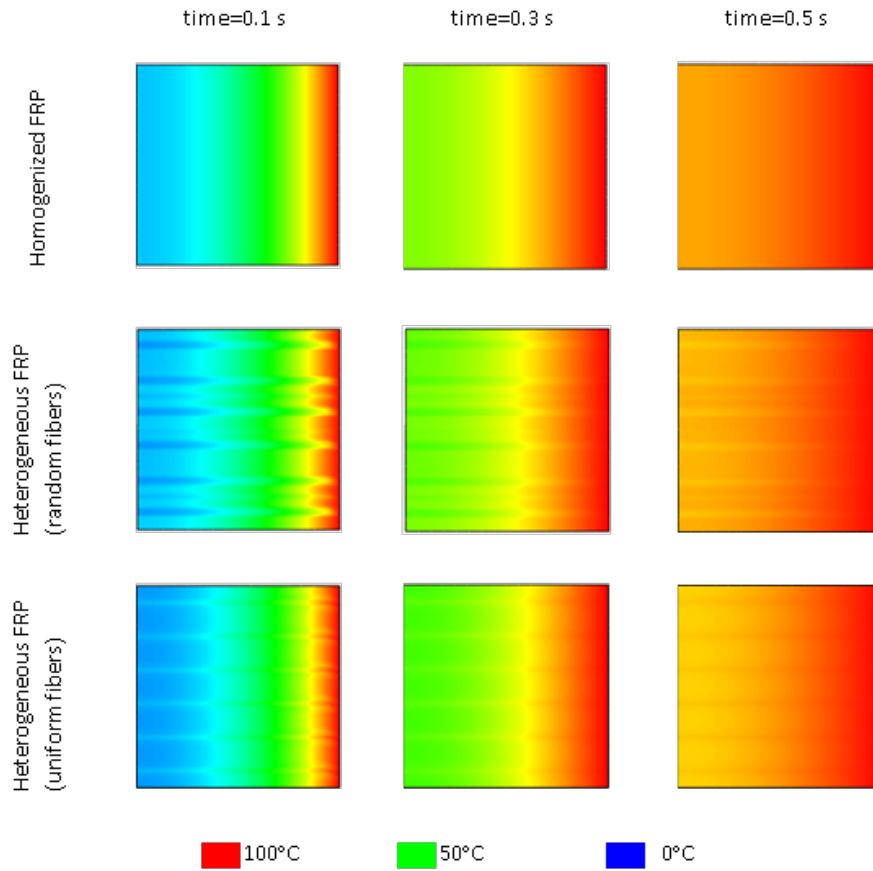


Figure 21 Temperature profile due to conduction along the fiber direction

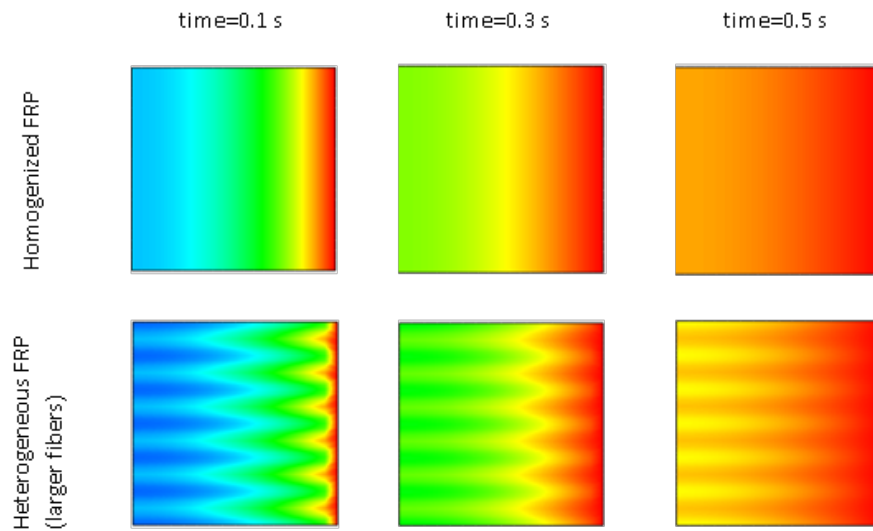


Figure 22 Temperature profile due to conduction along the fiber direction

Table 6 Times to steady state for transient heat transfer analyses, comparison of the two models

| Direction of heat conduction | Model | Fiber Volume Fraction | | | | | |
|--------------------------------------|--------------|-----------------------|-------|-------|-------|-------|-------|
| | | 10 | 20 | 40 | 50 | 67 | 75 |
| Steady State time (Longitudinal) [s] | UC model | 220 | 191.5 | 157.5 | 146 | 131.5 | 126 |
| | CPU time [s] | 781.5 | 688.1 | 565.8 | 526.5 | 473.8 | 459.9 |
| | MF model | 219 | 189 | 153.5 | 143.5 | 129 | 124 |
| | CPU time [s] | 8686 | 15833 | 8666 | 4150 | 5175 | 4987 |
| % Difference to reach steady state | | 0.46% | 1.32% | 2.61% | 1.74% | 1.94% | 1.61% |
| Steady State time (Trans) [s] | UC model | 263 | 253.5 | 226.5 | 209.5 | 179 | 163 |
| | CPU time [s] | 935.5 | 911.6 | 810.5 | 754.1 | 642.5 | 590.3 |
| | MF model | 254 | 240 | 214 | 206.5 | 173.5 | 154 |
| | CPU time [s] | 10077 | 20175 | 12045 | 5968 | 6916 | 6091 |
| % Difference to reach steady state | | 3.54% | 5.63% | 5.84% | 1.45% | 3.17% | 5.84% |

b) Coupled heat conduction and deformation in particle reinforced composites

In this section sequentially and fully coupled heat conduction and deformation are presented for particle reinforced composites. The unit-cell model is used to determine the average (macroscopic) response in the case of homogenized composites are considered. The responses are also compared to the heterogeneous model with detailed particle arrangements. Figure 23 shows the homogenized and heterogeneous composites. In the case of heterogeneous model is considered, different particle sizes are also considered for composites at fixed particle volume contents. The composites are subjected to temperature gradient on the opposite left and right surfaces and the left surface with lower temperature is constraint so that the displacement is zero. Figures 24 and 25 show the temperature and displacement profiles during the transient heat conduction process. Responses from the unit-cell model (homogenized composites) are compared to the ones of the heterogeneous bodies. The corresponding thermal stresses during heat conduction are also presented in Fig. 26. As expected the homogenized composites give smooth variations in thermal stresses, while the heterogeneous bodies can capture stress discontinuities and variations at the interfaces between particles and matrix. The unit-cell model is also used to predict fully coupled heat conduction and deformation in composites and functionally graded systems, as depicted in Fig. 7.

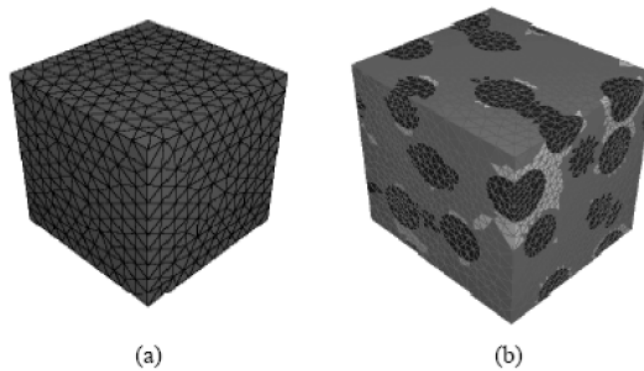


Figure 23 Finite element meshes of a) homogenized and b) heterogeneous particle composites.

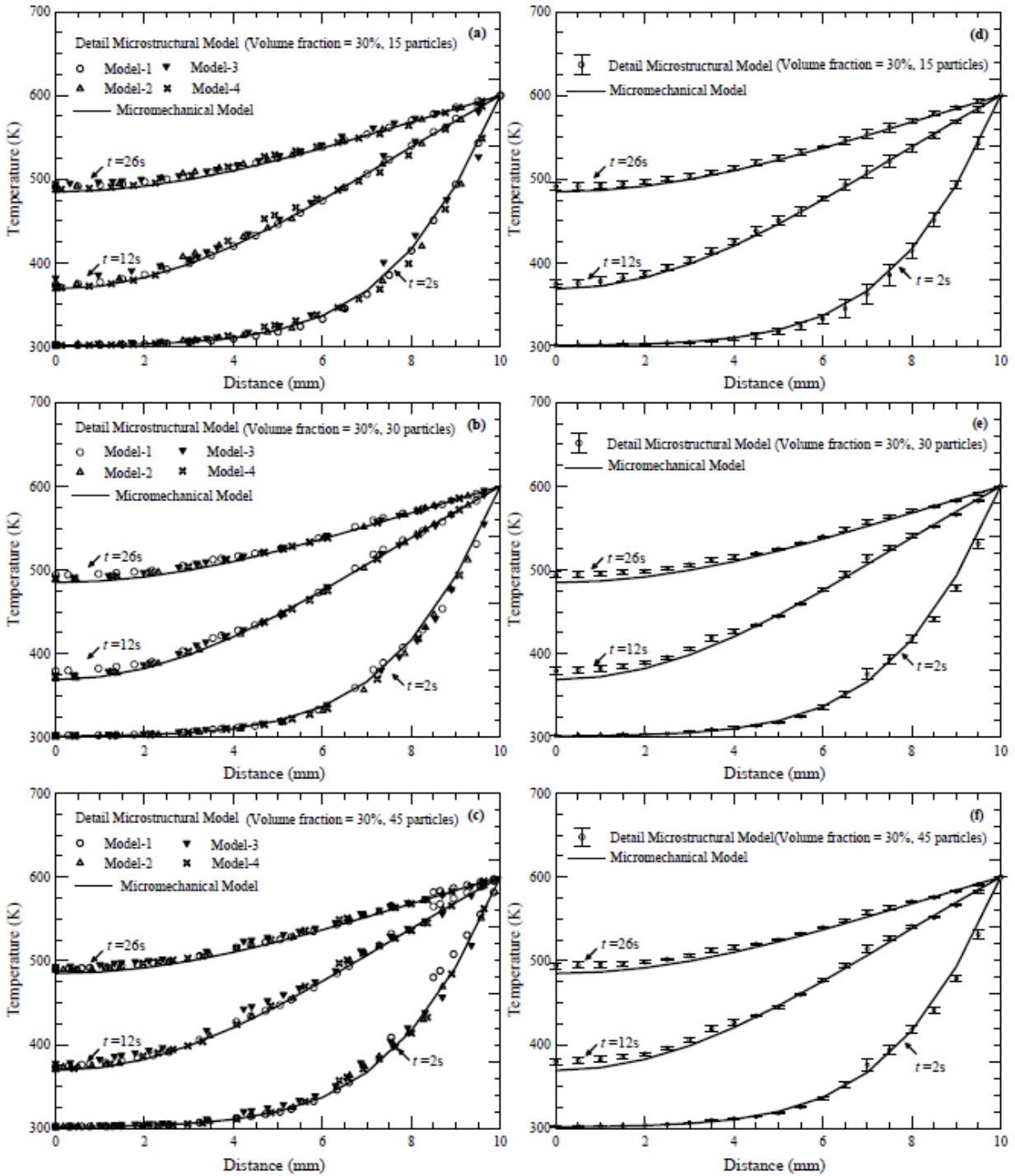


Figure 24 Temperature profiles for composites with 30% particle content: a, b, and c are actual values measured at the top surface; d, e, and f are mean values measured from top and bottom surfaces

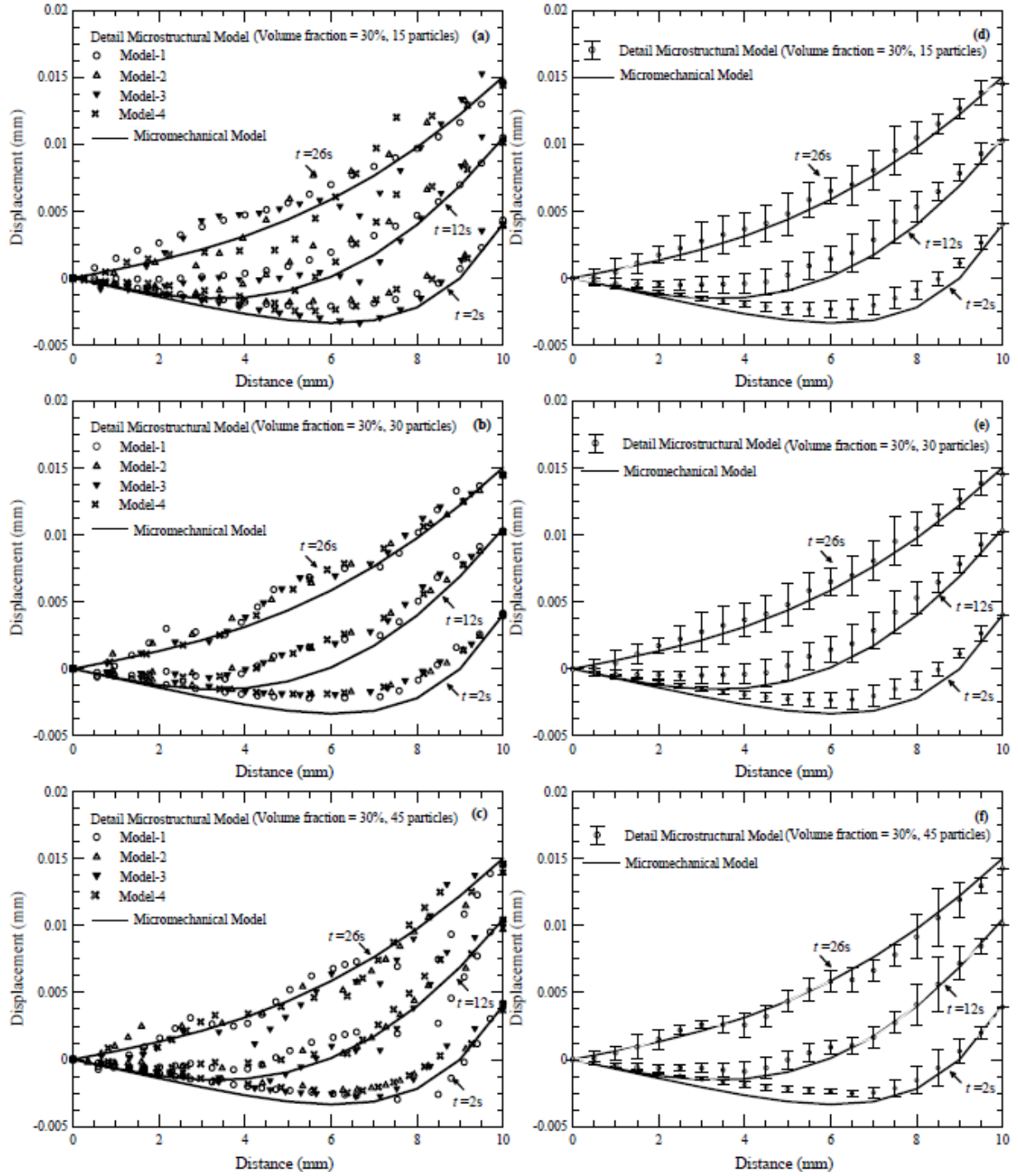


Figure 25 Displacement profiles for composites with 30% particle content: a, b, and c are actual values measured at the top surface; d, e, and f are mean values measured from top and bottom surfaces

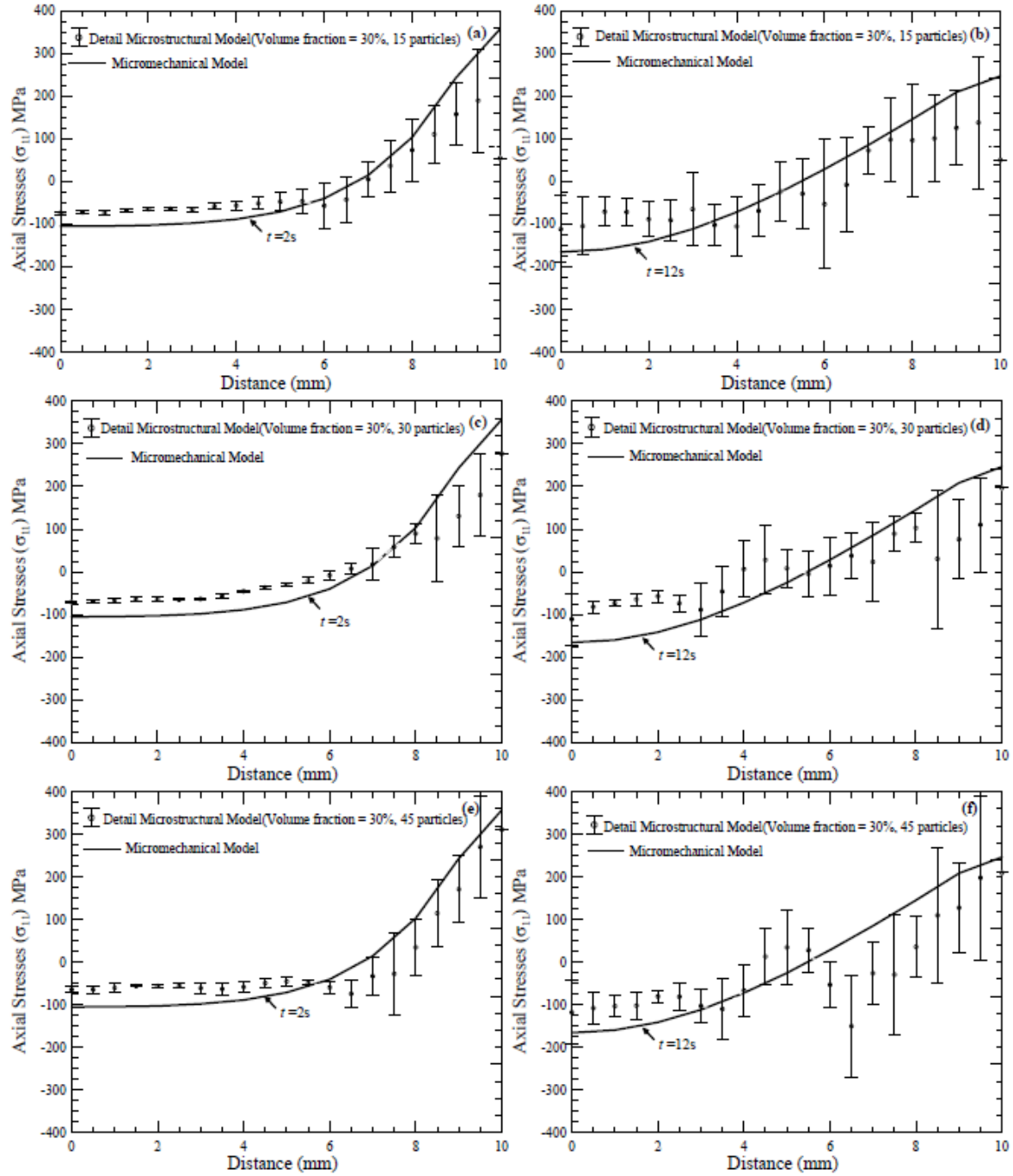


Figure 26 Thermal stress in the direction of temperature gradient during the transient process for composites with 30% particle content and different particle sizes.

c) Viscoelastic and viscoplastic responses of particle and fiber reinforced composites

The unit-cell models for the particle and fiber composites are now used to study the viscoelastic and viscoplastic responses of composites. The constitutive models for viscoelastic-viscoplastic responses are integrated to unit-cell models and also to finite elements. The overall responses

from the unit-cell models are compared to the ones determined from the composites with detailed arrangements of inclusions and/or with experimental data available in literature.

Figure 27 shows the creep-recovery behaviors of particle composites from the unit-cell (homogenized composite) and composite with detailed particles. The viscoplastic models of Valanis and Perzyna are also considered. It is seen that the unit-cell model can capture the average (macroscopic) viscoelastic-viscoplastic responses of the composites. The micromechanics models are also use to study a uniaxial tensile response of a composite bar. Both unit-cell model and microstructural model with detailed particle arrangements are considered. As seen in Fig. 28, the homogenized responses can predict the overall tensile behavior of the composites. The stress (von Mises) fields of the two composite models under a uniaxial tensile loading at different times are illustrated in Fig. 29. The limitation in the homogenized model is in capturing detailed stress variations and concentrations in the composites as the unit-cell model gives the average quantities of field variables.

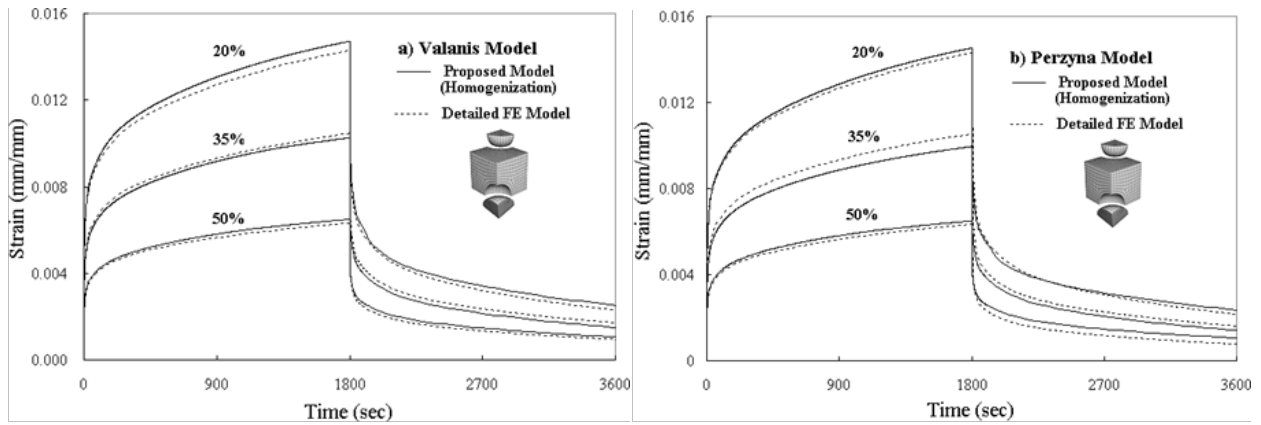


Figure 27 Creep recovery responses of particle composites with different particle volume fraction

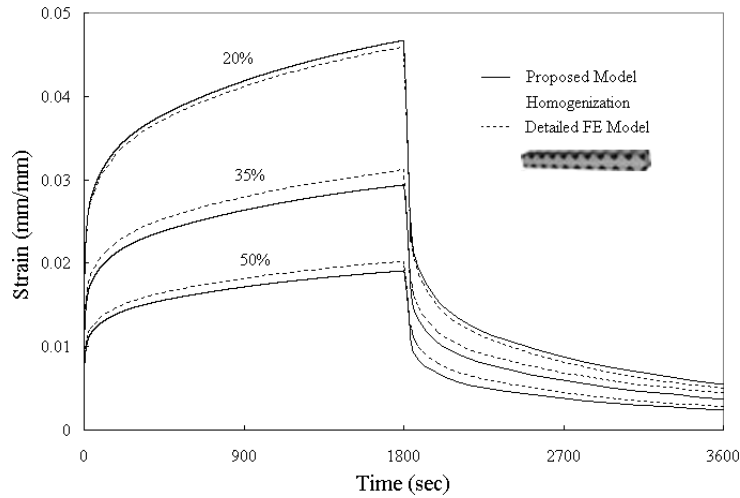
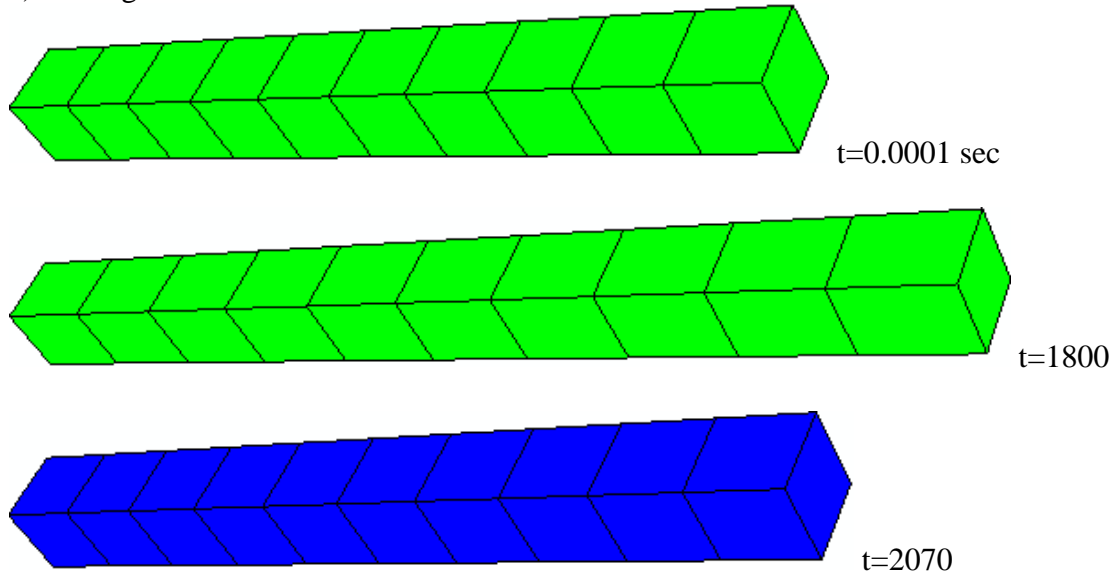


Figure 28 Creep responses under uniaxial tension of 30 MPa

a) Homogenized model



b) Heterogeneous model

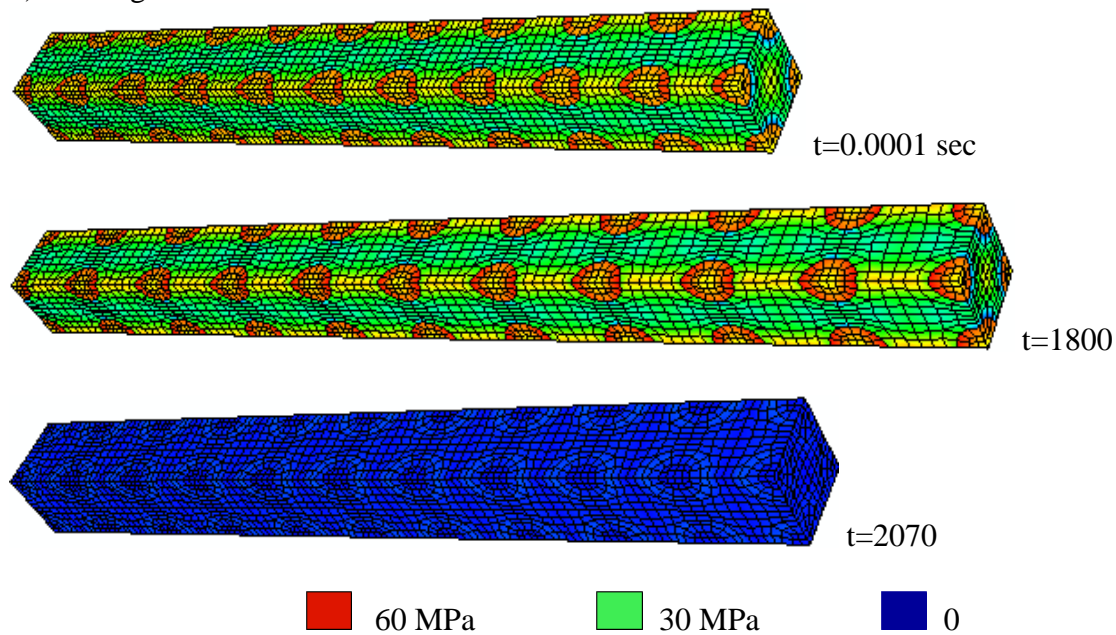


Figure 29 von-Mises stress distribution of creep-recovery responses under 30 MPa
a) homogenized model b) heterogeneous model

Next, the unit-cell model for fiber composites is used to study viscoelastic-viscoplastic responses of composites. Experimental data on the viscoelastic-viscoplastic response of glass FRP unidirectional composites reported by Megnis and Varna (2003) are used to validate the unit-cell model. The tests were performed on several off-axis composite specimens: 20° , 30° , 45° , 90° and 0° and stress levels. The viscoplastic parameters in the Perzyna's model were characterized by fitting the shear strain experimental data of the off-axis specimens at high stress levels. The remaining data of the off-axis specimens that were not used in the calibration are used to validate

the unit-cell model. Figure 30 shows the strain responses along the loading and transverse to the loading directions for composites with 90° off-axis fiber angle. Responses from the 90° composite show mainly viscoelastic behaviors. Figure 31 presents the responses for 20° off-axis fiber and significant viscoplastic response are seen in the shear component. Detailed discussion on the model and material calibration can be found in Jeon and Muliana (2012).

The responses from the homogenized composite model are also compared to those from the micromechanics models with detailed fiber arrangements (heterogeneous model), as illustrated in Fig. 20. Uniform and random fiber arrangements are considered in the heterogeneous model. For this simulation, carbon fiber is used for the fiber constituent and the high-density polyethylene (HDPE) is used for the matrix. Creep recovery behaviors of homogenized and heterogeneous composites with different fiber volume fractions are shown in Fig. 32. Loading is prescribed in the transverse fiber direction, and the corresponding strain outputs in the transverse and axial directions are compared. Again, the unit-cell model which represents the homogenized (average) behaviors of the composites can capture the overall time-dependent and inelastic responses. Tables 7 and 8 summarize percent differences in the strain responses calculated from the unit-cell and micromechanical model with detailed fiber arrangements, which in this study the largest difference is around 7%. One of the main advantages of using the unit-cell model is in reducing the computational cost since the stress and strain fields are sampling at several subcells instead of over the entire domain of composites. Table 9 presents the central processing unit (CPU) time needed in analyzing the time-dependent responses of composites using the unit-cell and detailed micromechanical models.

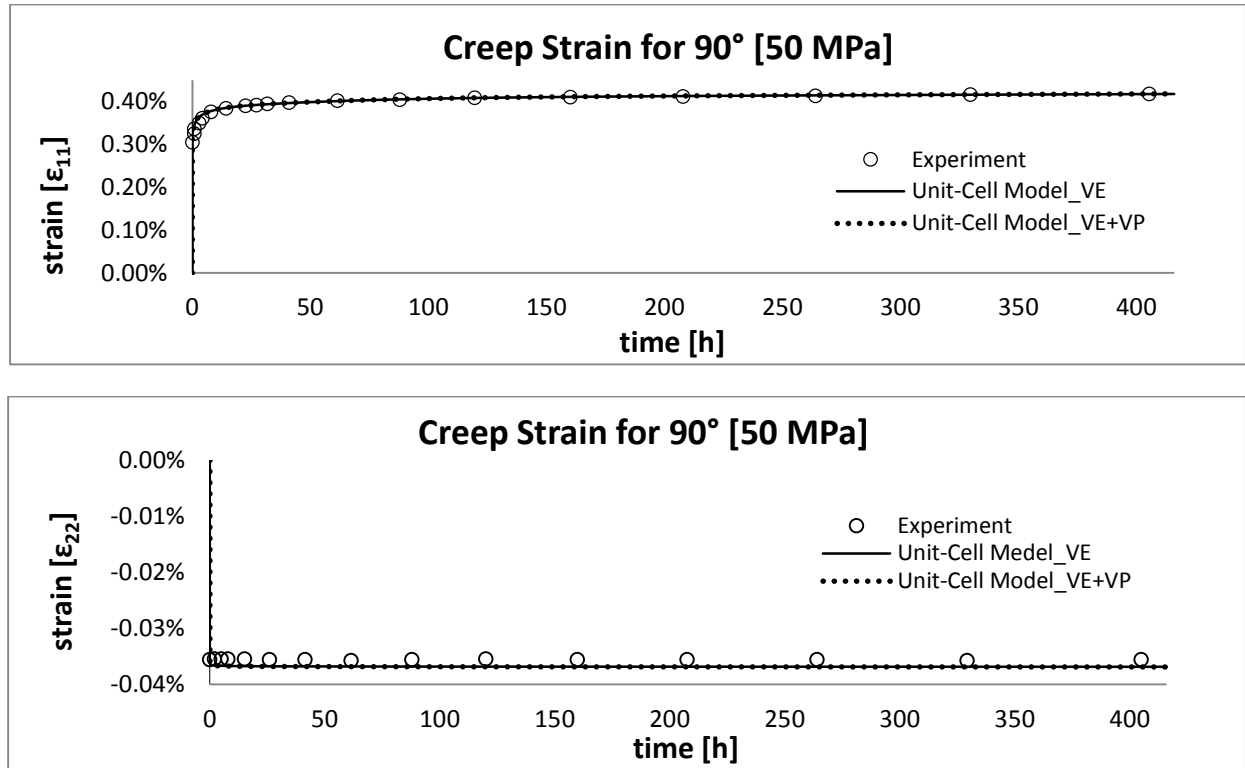


Figure 30 Creep strain for $[90]_m$ laminate. (○) experiment strain data, (—) calculated viscoelastic strain. Applied stress=50MPa (Transverse of fiber direction).

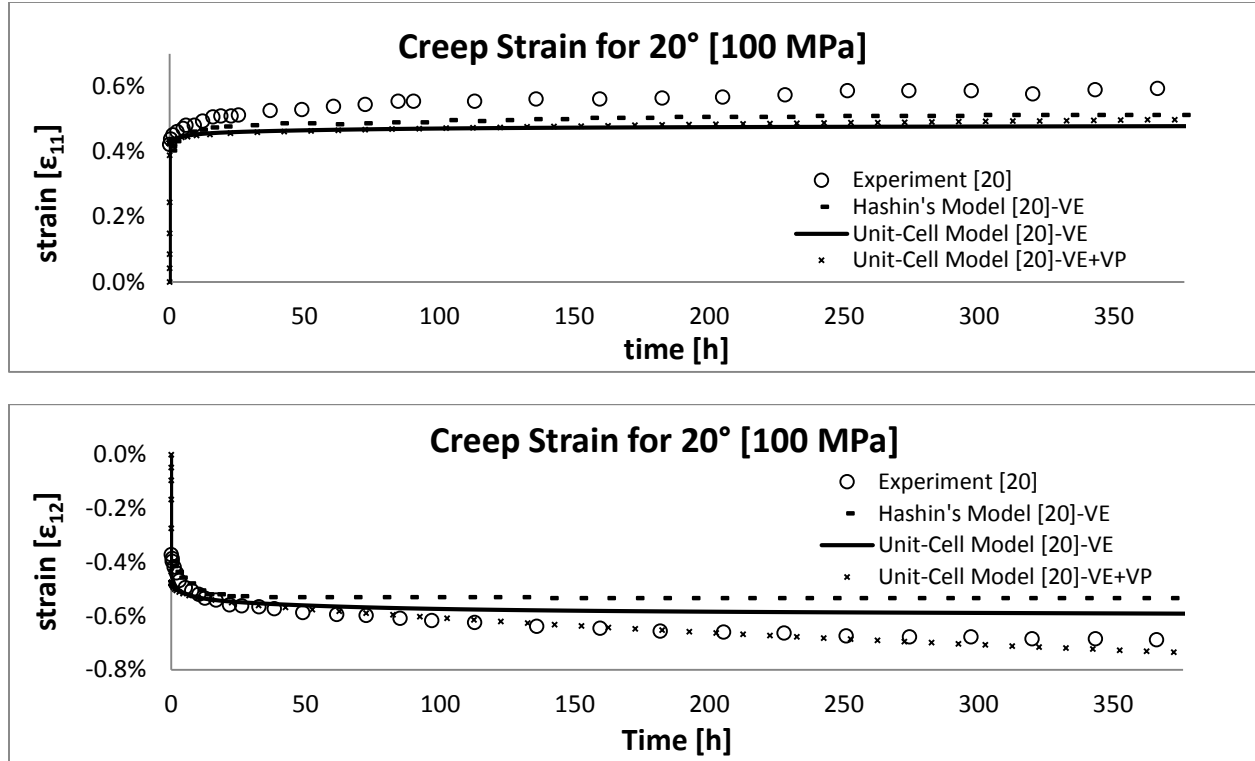


Figure 31 Creep strain for $[20]_m$ laminate.

Table 7 Percent difference of the strains from the unit-cell and FE micromechanical models

| Fiber Array | | Time [s] | Loading Direction | Strain | Difference % | | |
|-------------------------------------|-------|----------|-------------------|-----------------|--------------|--------------|--------------|
| | | | | | [10% V_f] | [20% V_f] | [50% V_f] |
| Unit-cell Model / Detailed FE Model | VE | 1800 | Fiber | ϵ_{11} | 2.43% | 2.49% | 4.45% |
| | | | | ϵ_{22} | 2.05% | 1.82% | 5.52% |
| | | | Transverse | ϵ_{11} | 1.67% | 1.79% | 4.86% |
| | | | | ϵ_{22} | 1.99% | 2.03% | 5.37% |
| | VE+VP | 1800 | Fiber | ϵ_{11} | 2.42% | 2.49% | 4.46% |
| | | | | ϵ_{22} | 2.05% | 1.82% | 5.54% |
| | | | Transverse | ϵ_{11} | 0.02% | 6.31% | 5.02% |
| | | | | ϵ_{22} | 0.31% | 3.90% | 5.69% |

Table 8 Percent difference of the strains from the unit-cell and FE micromechanical models with uniform detailed fiber arrangements

| Loading Direction | Model | | V _f 40 | V _f 54 | V _f 67 | V _f 75 |
|--------------------|--|-------------|-------------------|-------------------|-------------------|-------------------|
| Axial Loading | ε_{11} [mm/mm] (1800 s) | Unit-Cell | 1.08E-04 | 8.01E-05 | 6.51E-05 | 5.79E-05 |
| | | Detailed FE | 1.11E-04 | 8.21E-05 | 6.68E-05 | 5.94E-05 |
| | % Difference | | 2.53% | 2.54% | 2.53% | 2.53% |
| Transverse Loading | ε_{22} [mm/mm] (1800 s) | Unit-Cell | 1.73E-03 | 1.26E-03 | 9.17E-04 | 7.27E-04 |
| | | Detailed FE | 1.77E-03 | 1.34E-03 | 9.87E-04 | 7.58E-04 |
| | % Difference | | 2.47% | 6.05% | 7.12% | 4.10% |
| Number of Elements | | | 244590 | 240630 | 234360 | 247290 |
| Fiber Arrangement | | | 12*12 | 13*15 | 15*16 | 15*18 |
| Arrangement Ratio | | | 1.000 | 0.867 | 0.938 | 0.833 |

Table 9 CPU time for VE and VE+VP in homogeneous and heterogeneous models

| | FE Models | V_f [%] | Total Elements | CPU Time [s] | |
|-------|--------------------------------------|-----------|----------------|----------------|---------------------|
| | | | | Fiber Dir. | Transverse Dir. |
| VE | Unit-cell model | 10 | 1 | 2.1 | 75.4 |
| | | 20 | 1 | 2.0 | 75.6 |
| | | 50 | 1 | 1.6 | 168.7 |
| | Detailed FE model [Uniform Array] | 10 | 73728 | 41170 [11 Hr] | 534776 [149 Hr] |
| | | 20 | 73728 | 10952 [3 Hr] | 164220 [46 Hr] |
| | | 50 | 137490 | 25724 [7 Hr] | 20632 [6Hr] |
| VE+VP | Unit-cell model | 10 | 1 | 1.9 | 78.6 |
| | | 20 | 1 | 1.9 | 79.7 |
| | | 50 | 1 | 1.8 | 3836.6 |
| | Detailed FE model [Uniform Array] | 10 | 73728 | 92753 [26 Hr] | 11059224 [128 Days] |
| | | 20 | 73728 | 137217 [38 Hr] | 2095620 [24 Days] |
| | | 50 | 137490 | 24582 [7 Hr] | 3539790[41 Days] |

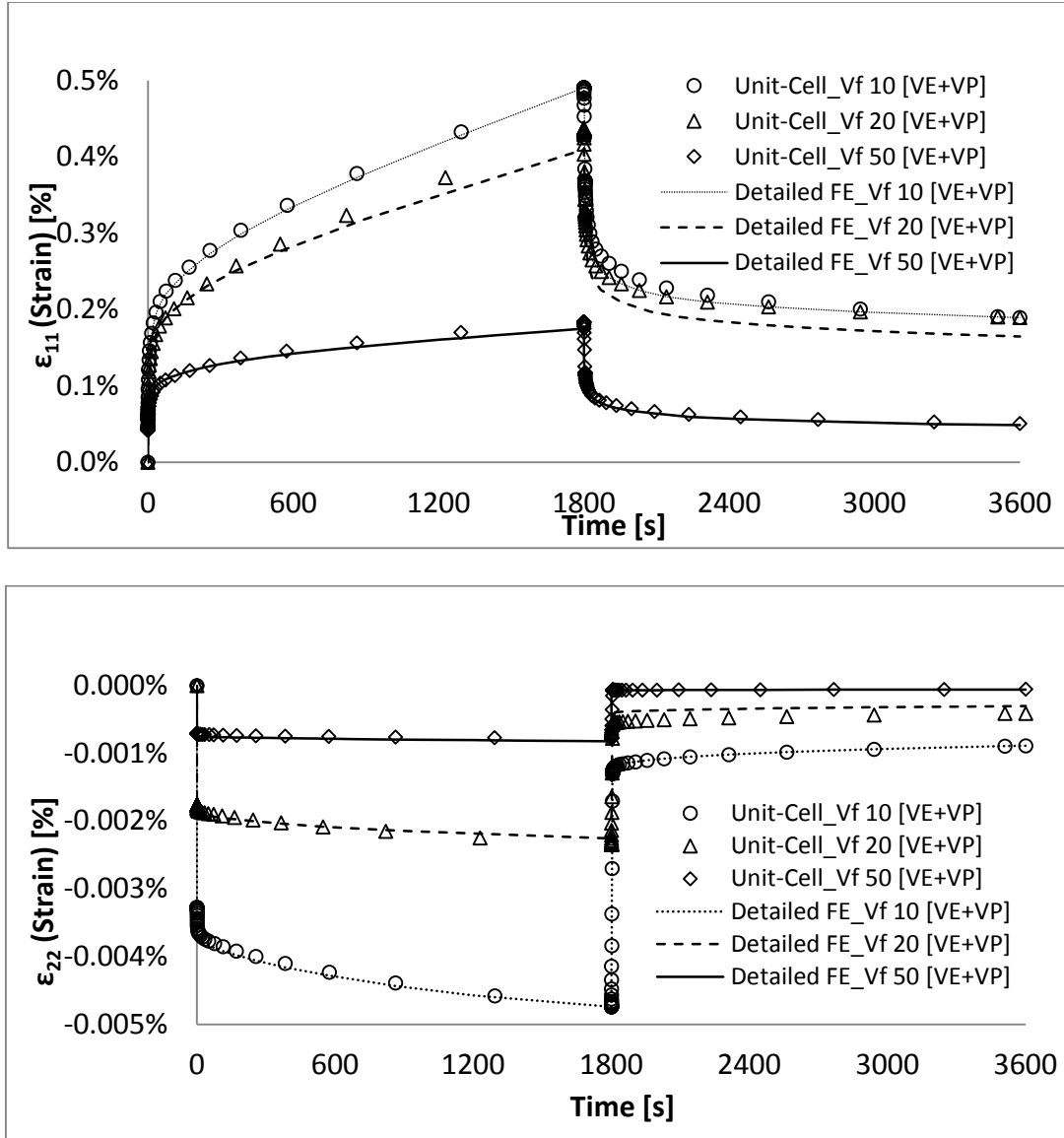


Figure 32 Creep recovery under loading in the transverse fiber direction. Top: response in the loading direction and Bottom: response in the perpendicular direction to loading

The unit-cell model is also used to study the thermo-mechanical responses of FRP composites. Examples of prediction of the coefficients of thermal expansion in the axial and transverse fiber directions are shown in Fig. 33. Experimental data are obtained from Karadeniz and Kumlutas (2007). The unit-cell model can capture the thermal expansion in the axial fiber direction, while some mismatches are seen in the transverse fiber directions. The reason of the mismatches are due to the thermal stress effects in the constituents due to temperature changes. The unit-cell model is limited in capturing the detailed stress distributions in the constituents.

Figure 34 illustrates the unit-cell predictions of stress relaxation behaviors in AFCs at different temperatures and strain levels. The AFCs consist of piezoelectric ceramic long fibers and epoxy matrix. The relaxation responses are due to the viscoelastic matrix, which are more pronounced

at elevated temperatures and higher strain levels. The unit-cell model is capable in capturing the relaxation responses of AFCs when damage/degradation is absent. A significant mismatch between the model and experimental data is observed under a strain of 1.61%, in which damage/cracking in the brittle ceramic fiber is observed in the specimen.

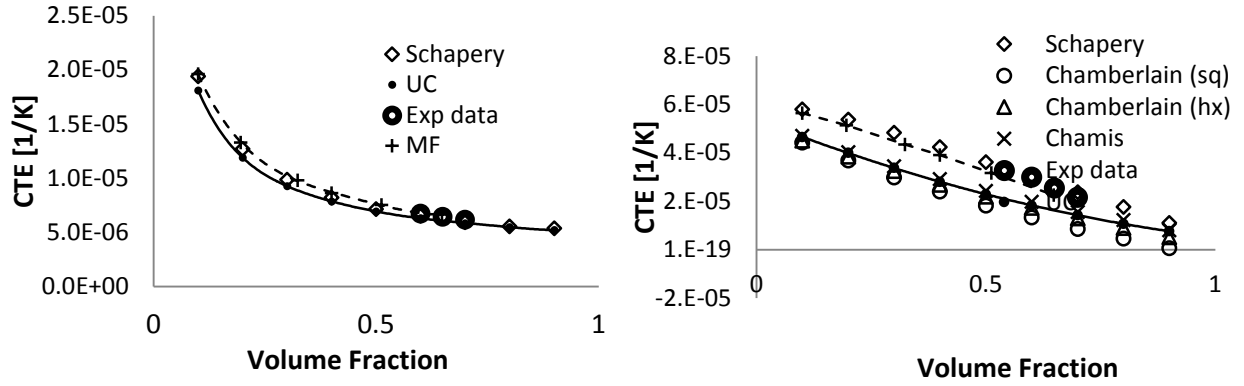


Figure 33 Thermal expansion coefficients in the axial (left) and transverse (right) fiber directions.

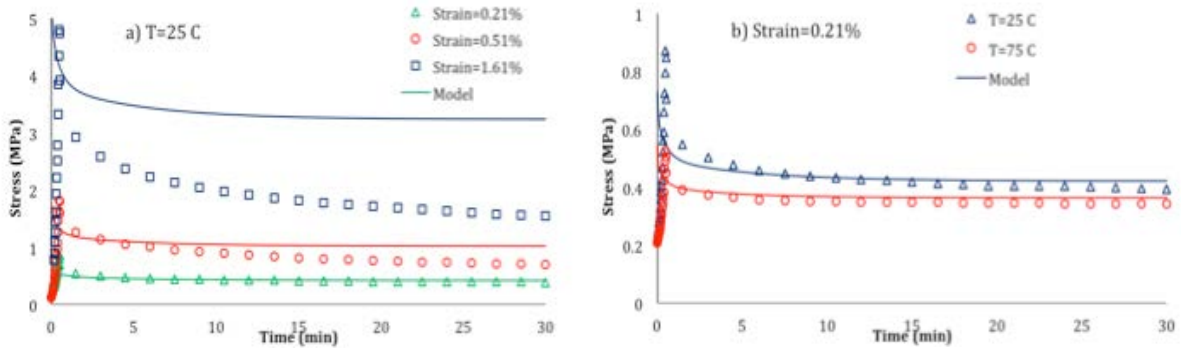


Figure 34 Stress relaxation responses of AFC at different temperatures and strain levels.

4.3.2) Thermo-electro-mechanical analyses

Micromechanical models for fiber and particle composites are formulated in order to determine the overall thermo-electro-mechanical response of composites undergoing heat conduction and electro-mechanical stimuli. Unit-cell models are first considered. A general linearized constitutive relations written in Eq. (15) is adopted and used within a volume averaging scheme in the unit-cell model. Micromechanical models with detailed fiber and particle arrangements are also generated and used to study the thermo-electro-mechanical response of active composites. Furthermore, the responses from the unit-cell models are compared to currently available micromechanics models such as Mori-Tanaka and Self Consistent models.

Following a linearized constitutive model in Eq. (15), the average (effective) field variables, indicated by an over-bar, in the unit-cell models are defined as:

$$\bar{\Gamma} = \frac{1}{V} \sum_{m=1}^N \int_{V^{(m)}} \Gamma^{(m)}(\mathbf{x}) dV^{(m)} \approx \frac{1}{V} \sum_{m=1}^N V^{(m)} \Gamma^{(m)} \quad (19-1)$$

$$\bar{\mathbf{Z}} = \frac{1}{V} \sum_{m=1}^N \int_{V^{(m)}} \mathbf{Z}^{(m)}(x) dV^{(m)} \approx \frac{1}{V} \sum_{m=1}^N V^{(m)} \mathbf{Z}^{(m)} \quad (19-2)$$

The variables $\Gamma^{(m)}$ and $\mathbf{Z}^{(m)}$ are the components of the average field quantities in each subcell.

The unit-cell volume V is defined by $V = \sum_{m=1}^N V^{(m)}$. This study deals with nonlinear electro-

mechanical response for the inclusions and viscoelastic response of the matrix constituent, which requires incorporating history of loading to determine the overall response of the composites.

The solutions for the field variables are performed incrementally. The incremental forms of the effective and local field variables at current time are:

$$\begin{aligned} \bar{\Gamma}^t &= \bar{\Gamma}^{t-\Delta t} + \Delta \bar{\Gamma}^t \\ \bar{\mathbf{Z}}^t &= \bar{\mathbf{Z}}^{t-\Delta t} + \Delta \bar{\mathbf{Z}}^t \\ \Gamma^{(m),t} &= \Gamma^{(m),t-\Delta t} + \Delta \Gamma^{(m),t} \\ \mathbf{Z}^{(m),t} &= \mathbf{Z}^{(m),t-\Delta t} + \Delta \mathbf{Z}^{(m),t} \end{aligned} \quad (20)$$

where the superscript $t-\Delta t$ denotes the previous time and all the field variables associated with $t-\Delta t$ are considered as history variables. At each time increment Δt , it is necessary to calculate the incremental field variables at current time. A linearized micromechanical relation is imposed to the incremental parts of the field variables and a residual arises from the linearization is corrected incrementally to satisfy both micromechanical constraints and constitutive equations for the inclusions and matrix. For simplicity, the superscript related to time is dropped and the rest of the incremental formulation are presented at current time t . The local average independent field variables can be expressed in terms of effective (homogenized) field variables which in the incremental form are written as:

$$\Delta \Gamma^{(m)} = \mathbf{F}^{(m)} \Delta \bar{\Gamma} \quad (21)$$

where $\mathbf{F}^{(m)}$ is the concentration tensor for the subcell (m).

The above averaging schemes give an exact effective response of the homogenized composites only when linear constitutive equations are used for all constituents (subcells) in the unit-cell model. In the case of nonlinear constitutive models are considered for the constituents, imposing the linearized micromechanical relations for the incremental field variables could lead to residual. At every instant of time a corrector scheme is added to minimize the residual. This study uses the Newton-Raphson iterative method as a corrector scheme. Once the residual has been minimized, the components of the concentration matrices $\mathbf{F}^{(m)}$ are determined and the field variables $\Delta \Gamma^{(m)}$ in each subcell due to the prescribed boundary conditions at the macro (homogenized composite) level are calculated using Eq. (21). Finally, the constitutive equations in **Section 4.2** are used to obtain the field variables $\Delta \mathbf{Z}^{(m)}$ in each subcell and the effective field variables at every instant of time are evaluated using the volume average scheme in Eq. (19). From the micro-macro scale relation in Eq. (21) and constitutive relation for each subcell in Eq. (15), the effective field variables from Eq. (19) is given as:

$$\Delta \bar{\mathbf{Z}} \approx \frac{1}{V} \sum_{m=1}^N V^{(m)} \boldsymbol{\Omega}^{(m)} \mathbf{F}^{(m)} \Delta \bar{\boldsymbol{\Gamma}} \quad (22)$$

and the effective linearized properties are $\bar{\boldsymbol{\Omega}} \approx \frac{1}{V} \sum_{m=1}^N V^{(m)} \boldsymbol{\Omega}^{(m)} \mathbf{F}^{(m)}$.

a) Nonlinear response of polarized active inclusions

First the effective responses of active fiber composites under a uniaxial tensile creep of 10 MPa are simulated using the unit-cell model. Micromechanical models with detailed fiber arrangements, which are implemented in FE, are also considered for comparisons. Figures 35 and 36 illustrate the corresponding axial and transverse strains and electric flux in PZT-7A/LaRC-Si composites during creep loading at different temperatures. The viscoelastic matrix induces time-dependent changes in the electric flux of the composites. The unit-cell model is capable in capturing the overall thermo-electro-mechanical responses of active composites.

Next, field variables, i.e., temperature, displacement, stress, electric field, and electric flux, in active fiber during transient heat conduction throughout the composite body are examined using the unit-cell model. The unit-cell model allows incorporating different time- and field dependent behaviors for the constituents during the conduction of heat and deformation in the composite body. Consider an active fiber composite panel where the longitudinal fibers are aligned in the x_3 direction undergoing conduction of heat along the longitudinal fiber axis. It is assumed that the composite panel is perfectly insulated so that the amount of heat loss is ignored. The analytical solutions are obtained by imposing a plane stress condition. Figure 37 depicts the axial displacements, stresses, electric fluxes, and electric fields at several instants of time during the transient heat conduction. The non-uniform temperature profiles at early times lead to relatively high axial stress, electric field, and electric flux. As time progresses and steady state condition is reached, the axial stress and electric field should drop to zero, while the electric flux approaches a constant value. On the other hand, the transverse stress increases as time progresses and the maximum value is at the steady state condition, which is expected.

Next, the unit-cell models for electro-active composites are compared to available experimental data and other micromechanics models, i.e., Mori Tanaka (MT) and Self-consistent (SC) models. Detailed formulations of the MT and SC models with nonlinear electro-mechanical constitutive models for the inclusions are given in Lin and Muliana (2013). The overall electro-mechanical properties determined using the micromechanics models are first compared with existing experimental data with linear piezoelectric properties. Chan and Unsworth (1989) experimentally examined a piezoelectric FRC with continuous fiber reinforcement PZT-7A embedded in an Araldite D medium. Figure 38 illustrates the comparisons of effective electrical and mechanical properties of active fiber composites. All micromechanics models are in agreements with the experimental data over the whole range of volume fractions. Figure 39 depicts the micromechanics models predictions of the piezoelectric particle composites, which was experimentally studied by Furukawa et al. (1976). The piezoelectric composite consists of spherical PZT-5 particles embedded in an epoxy medium. Finally, Fig. 40 shows the linear and nonlinear electro-mechanical responses determined from the UC and MT models. As seen in the figure, at high electric field input, the nonlinear responses lead to higher strains in the

composites. The micromechanics models are capable in predicting the linear and nonlinear responses.

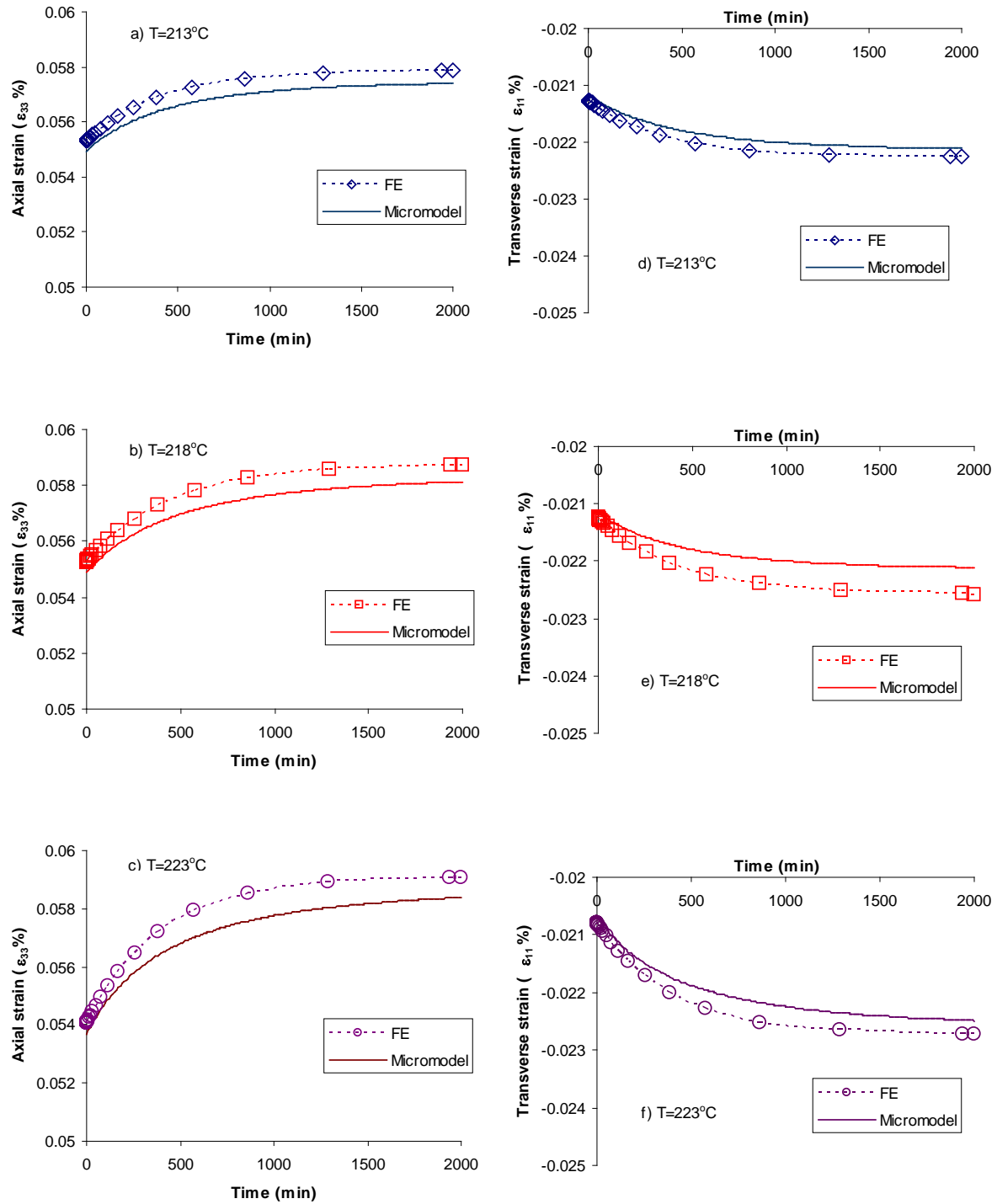


Figure 35 Axial creep strain (ϵ_{33}) and transverse creep strain (ϵ_{11}) of PZT-7A/LaRC-Si composites with 19.6% fiber volume contents due to a constant stress $\sigma_{33} = 10$ MPa

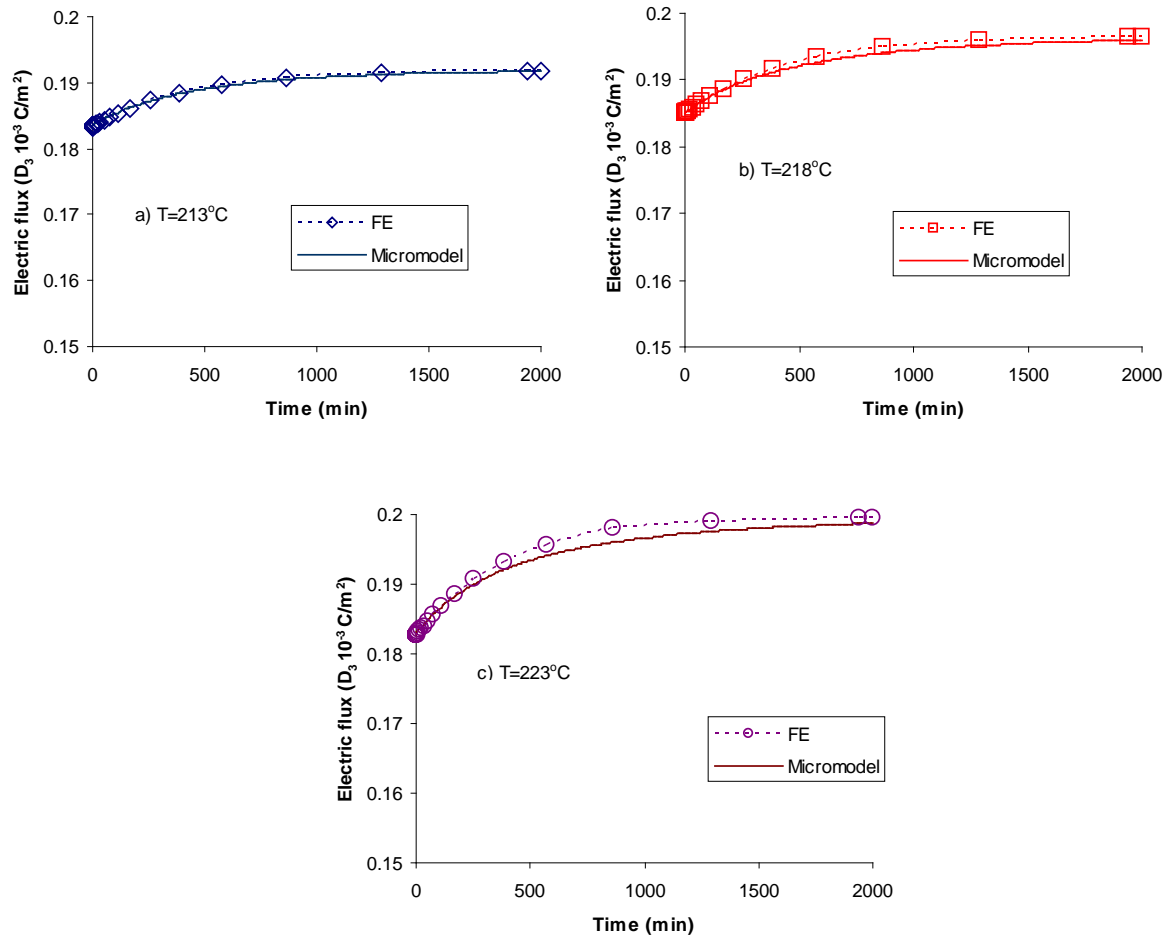


Figure 36 Electric flux along the polarization axis (D_3) of PZT-7A/LaRC-Si composites with 19.6% fiber volume contents due to a constant stress $\sigma_{33} = 10 \text{ MPa}$

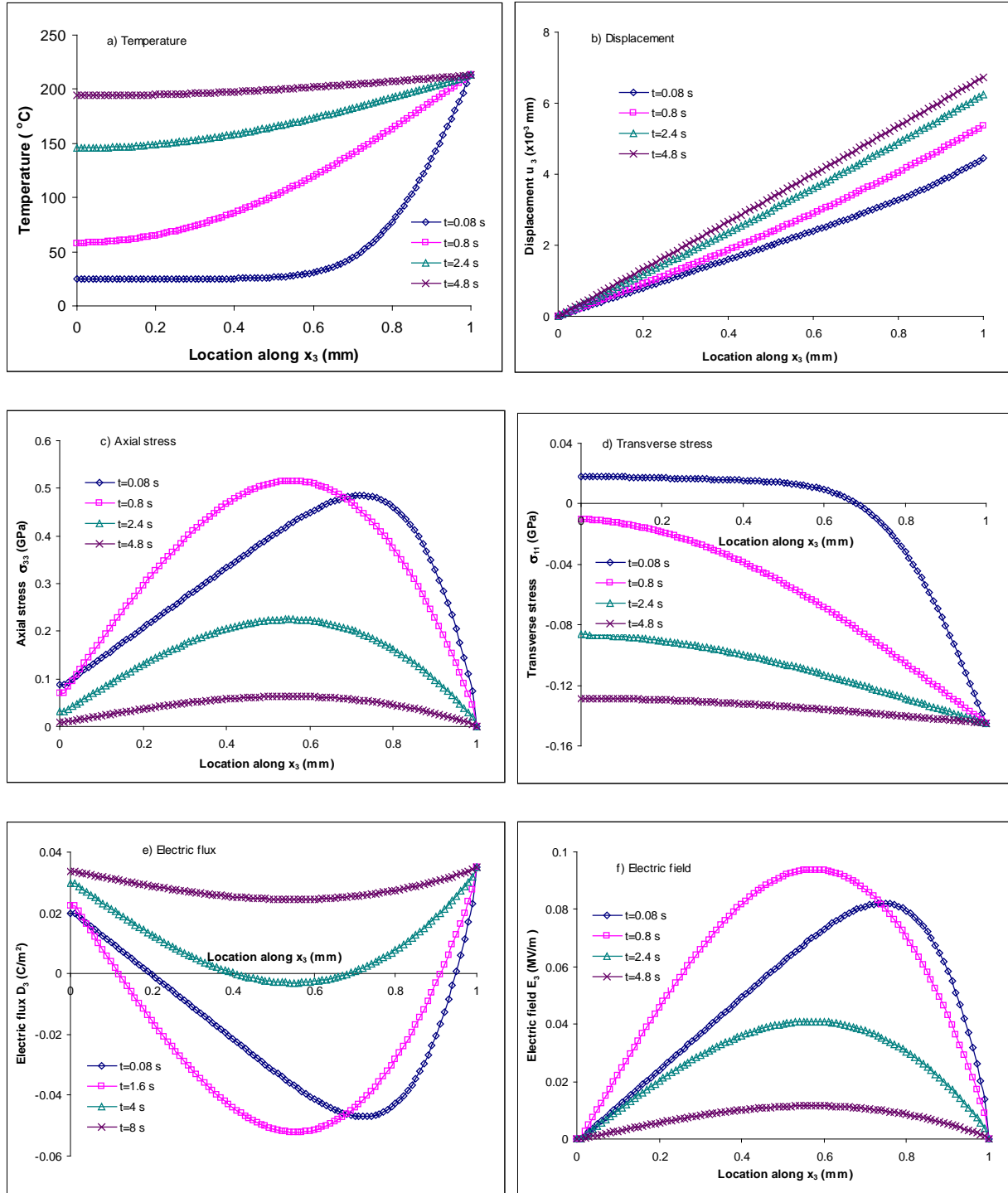


Figure 37 Field variables of the active PMC panel during transient heat conduction process

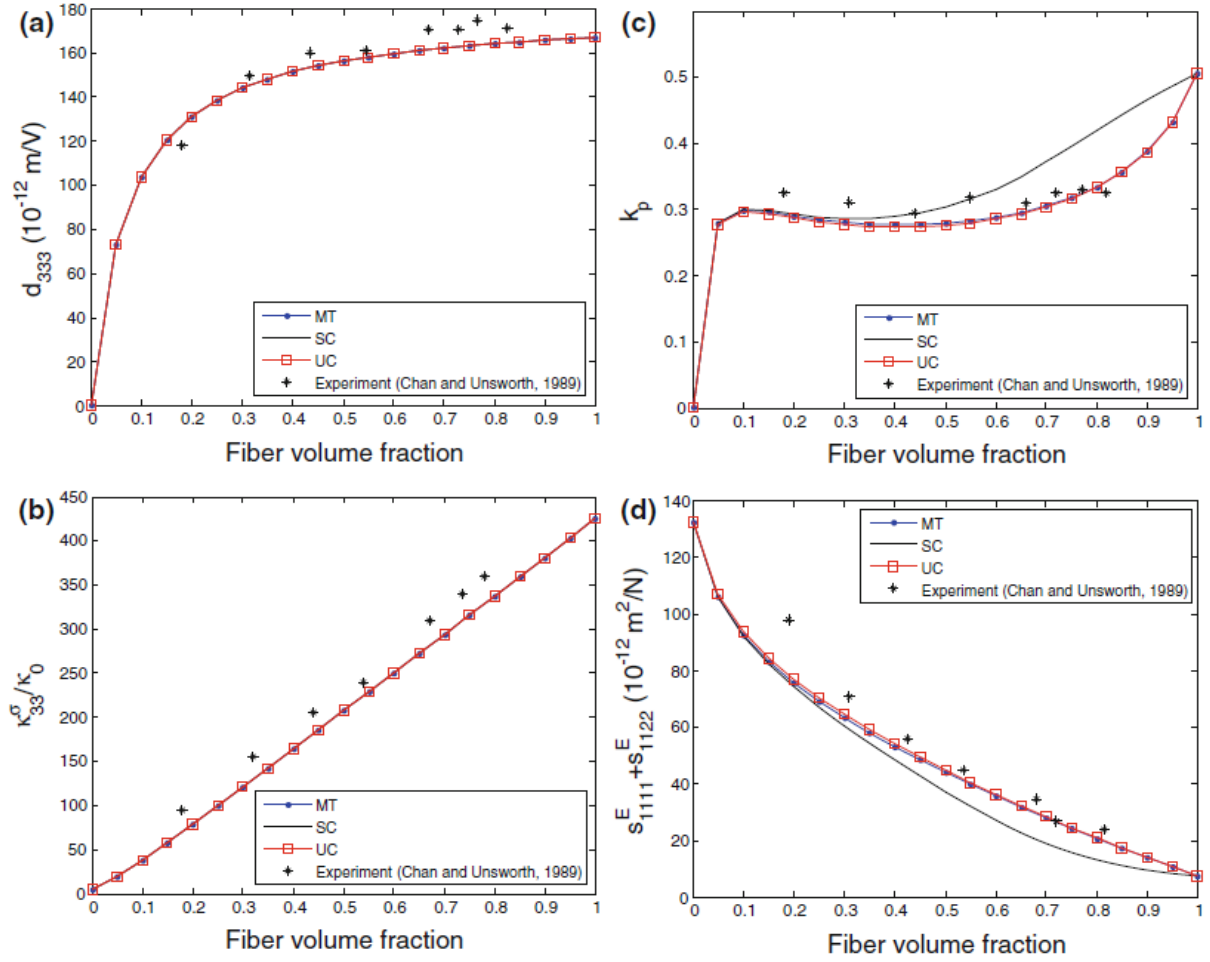


Figure 38 Comparison of electro-mechanical properties of various micromechanics models with experimental data (Chan and Unsworth, 1989) for the PZT-7A/Araldite D fibrous composite with fiber volume fraction.

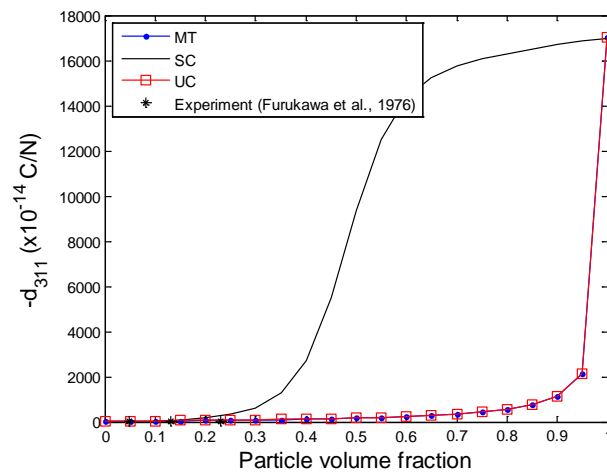


Figure 39 Comparison of piezoelectric constant of various micromechanics models with experimental data (Furukawa et al., 1976) for the PZT-5/epoxy particulate composite.

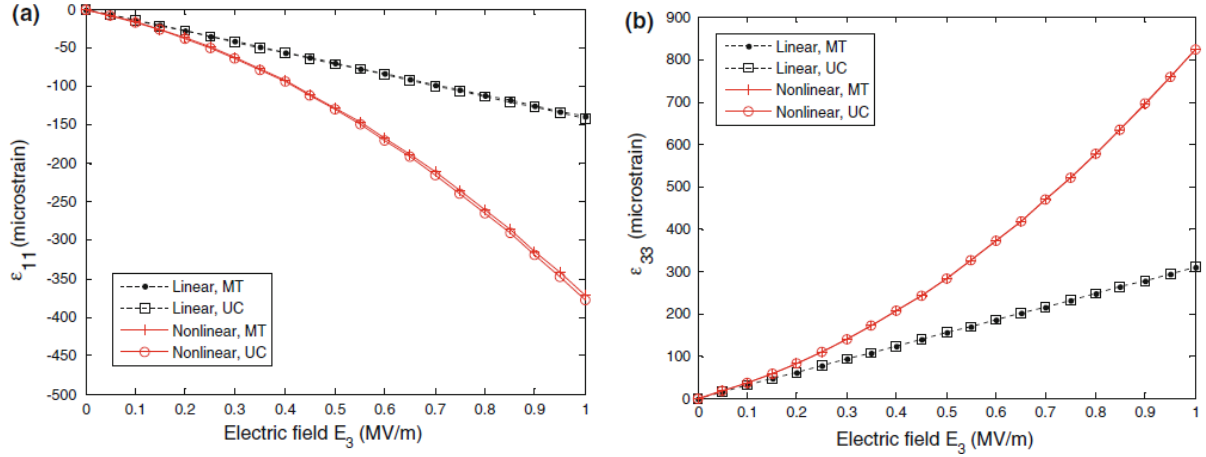


Figure 40 Comparisons of effective responses from MT and UC models for active fiber composite with fiber volume fraction 0.5 under and applied electric field in the fiber direction

b) Nonlinear polarization switching responses

The fiber-unit-cell and particle-unit-cell models are formulated to determine the effective hysteretic polarization and butterfly strain responses of 1-3 and 0-3 ferroelectric composites, respectively. A phenomenological constitutive model that accounts for the rate-dependent polarization under coupled mechanical and electrical effects, proposed by Sohrabi and Muliana (2013) and discussed in **Section 4.2.2**, is used for the ferroelectric constituent while the matrix is considered as a linear elastic or viscoelastic solid. An incremental formulation is used for the constitutive relations and unit-cell models. In order to account for history-dependent response from the time-dependent ferroelectric and viscoelastic matrix, history variables are introduced. The linearized constitutive relation for each constituent is written as:

$$\begin{aligned} \Xi^t &= \mathbf{O}^t \Delta \mathbf{T}^t + \Xi^{t-\Delta t} \\ \Xi^t &= \begin{Bmatrix} \epsilon^t \\ \mathbf{D}^t \end{Bmatrix}, \quad \mathbf{O}^t = \begin{bmatrix} \tilde{\mathbf{s}}^t & \tilde{\mathbf{d}}^t \\ \tilde{\mathbf{d}}^t & \tilde{\kappa}^t \end{bmatrix}, \quad \Delta \mathbf{T}^t = \begin{Bmatrix} \Delta \sigma^t \\ \Delta \mathbf{E}^t \end{Bmatrix}. \end{aligned} \quad (23)$$

where the superscript $t - \Delta t$ denotes previous time and $\Xi^{t-\Delta t}$ is the history variables of the dependent field variables Ξ^t . The components of \mathbf{O}^t and $\Xi^{t-\Delta t}$ for the ferroelectric ceramics and viscoelastic materials can be found in Lin and Muliana (2014).

Using the volume averaging scheme, the linearized effective field variables, denoted by an overbar, of the UCs at current time t are:

$$\bar{\Xi}^t = \sum_{m=1}^N V^{(m)} \Xi^{(m),t} \quad (24)$$

where N is the number of subcells (e.g. $N=4$ for a fiber UC and $N=8$ for a particle UC). The variable $\Xi^{(m),t}$ is the average field variable within each subcell with a volume fraction $V^{(m)}$. Following a linearized constitutive relation for each constituent in Eq. (23), a linearized constitutive relation for the overall response of composites at current time t is written as:

$$\bar{\Xi}^t = \bar{\mathbf{O}}^t \Delta \bar{\mathbf{T}}^t + \bar{\Xi}^{t-\Delta t} \quad (25)$$

In order to relate the effective incremental independent field variable in the UC, $\Delta \bar{\mathbf{T}}^t$, to the corresponding incremental field variable in its subcells, $\Delta \mathbf{T}^{(\alpha),t}$, a concentration matrix $\mathbf{B}^{(m),t}$ and a vector of history variables $\mathbf{X}^{(m),t}$ at current time t are defined as follows:

$$\Delta \mathbf{T}^{(m),t} = \mathbf{B}^{(m),t} \Delta \bar{\mathbf{T}}^t + \mathbf{X}^{(m),t}. \quad (26)$$

Using Eq. (26) and (24), the effective field variables in Eq. (24) are written as:

$$\begin{aligned} \bar{\mathbf{\Xi}}^t &= \sum_{m=1}^N V^{(m)} \mathbf{O}^{(m),t} \mathbf{B}^{(m),t} \Delta \bar{\mathbf{T}}^t + \sum_{m=1}^N V^{(m)} \left(\mathbf{O}^{(m),t} \mathbf{X}^{(m),t} + \bar{\mathbf{\Xi}}^{(m),t-\Delta t} \right) \\ \bar{\mathbf{O}}^t &= \sum_{m=1}^N V^{(m)} \mathbf{O}^{(m),t} \mathbf{B}^{(m),t}, \quad \bar{\mathbf{\Xi}}^{t-\Delta t} = \sum_{m=1}^N V^{(m)} \left(\mathbf{O}^{(m),t} \mathbf{X}^{(m),t} + \bar{\mathbf{\Xi}}^{(m),t-\Delta t} \right) \end{aligned} \quad (27)$$

In order to evaluate the concentration matrices and history variables $\mathbf{B}^{(m),t}$ and $\mathbf{X}^{(m),t}$ the constitutive relations for the different constituents together with the linearized micromechanical relations from the fiber and particle model are used (see Lin and Muliana, 2014).

The predictions of the effective hysteretic polarization and butterfly strain responses of active fiber composites are compared with existing experimental data reported by Jayendiran and Arockiarajan (2013). PZT-5A1/epoxy fiber composites having various PZT-5A1 fiber volume fractions (VFs) were studied. The composites were subjected to cyclic electric field with amplitude of $\bar{E}_3 = \pm 2$ MV/m, along x_3 direction. The material properties of the PZT-5A1 are first calibrated from the experimental data of PZT-5A1 (100% fiber content) under a cyclic electric field, shown in Figures 41a and 41b. Jayendiran and Arockiarajan (2013) also reported the experimental results for the pure PZT-5A1 subject to both a cyclic electric field and a constant mechanical stress (i.e., $\bar{\sigma}_{33} = -15$ MPa) shown in Figure 42 (circles). The existence of the compressive stresses influences the polarization response of materials. The coercive electric field under a constant compressive stress 15 MPa, $E_c = 0.76$ MV/m, is determined when the polarization is zero as shown in Figure 41a. From the experimental evidences the coercive electric fields vary with the compressive stresses. Detailed material parameter characterizations are given in Lin and Muliana (2014). Micromechanical model predictions of composite with VF = 0.8 subjected to both a cyclic electric field and various constant mechanical stresses are shown in Fig. 43. Figure 44 presents responses under a constant compressive stress and cyclic electric fields for composites with different fiber contents. The agreements on the effective hysteretic polarization between the micromechanical predictions and experimental data are good for each compressive stress while the estimations of the effective butterfly strain responses show some discrepancies with the experimental results. The height of the butterfly strain response of the experimental measurements of the active composite is larger than the one of the pure PZT-5A1. One would expect that the height of the hysteretic polarization (saturated polarization) decreases as the volume content of the active fiber decreases and similarly for the height of the strain in the butterfly strain curves.

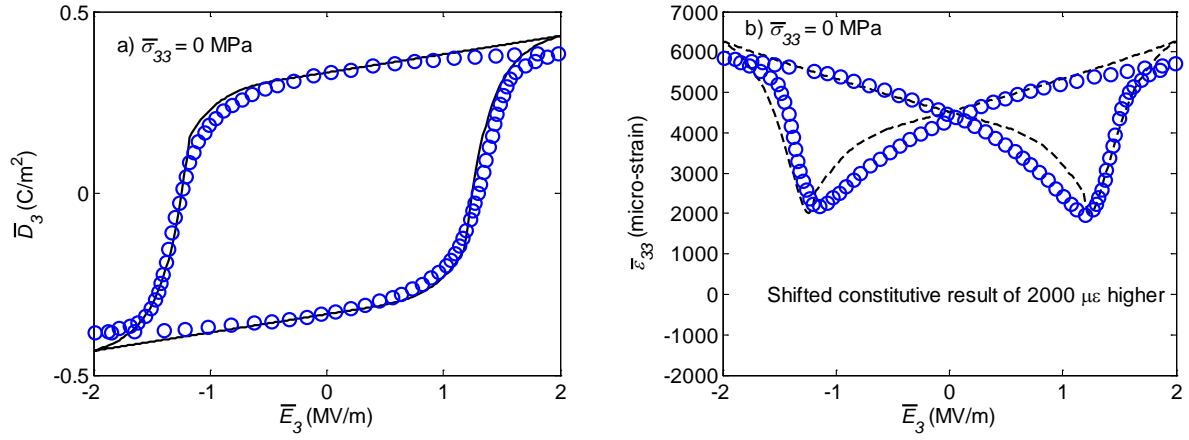


Figure 41 a) Hysteretic polarization and b) butterfly strain responses for the stress free PZT-5A1 due to a cyclic electric field.

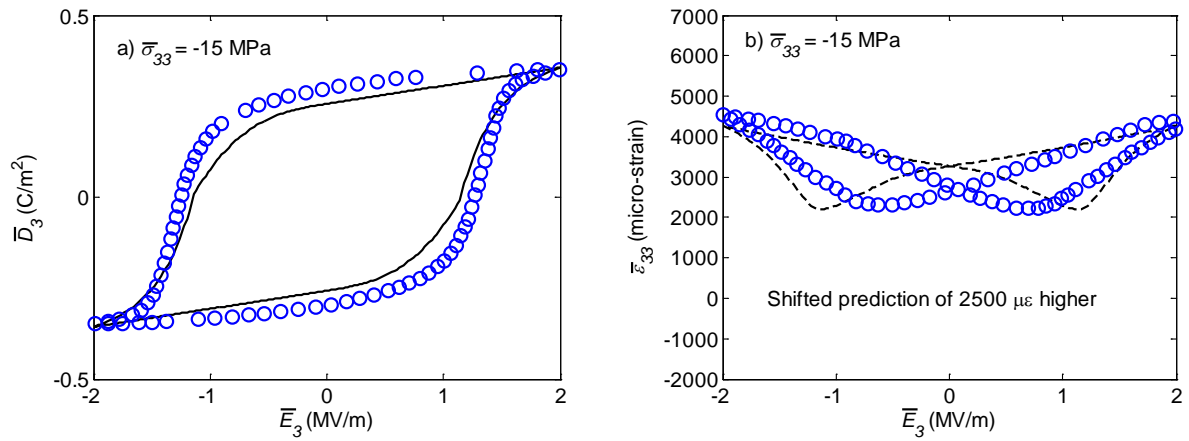


Figure 42 a) Hysteretic polarization and b) butterfly strain responses for the PZT-5A1 due to a cyclic electric field and a constant compressive stress.

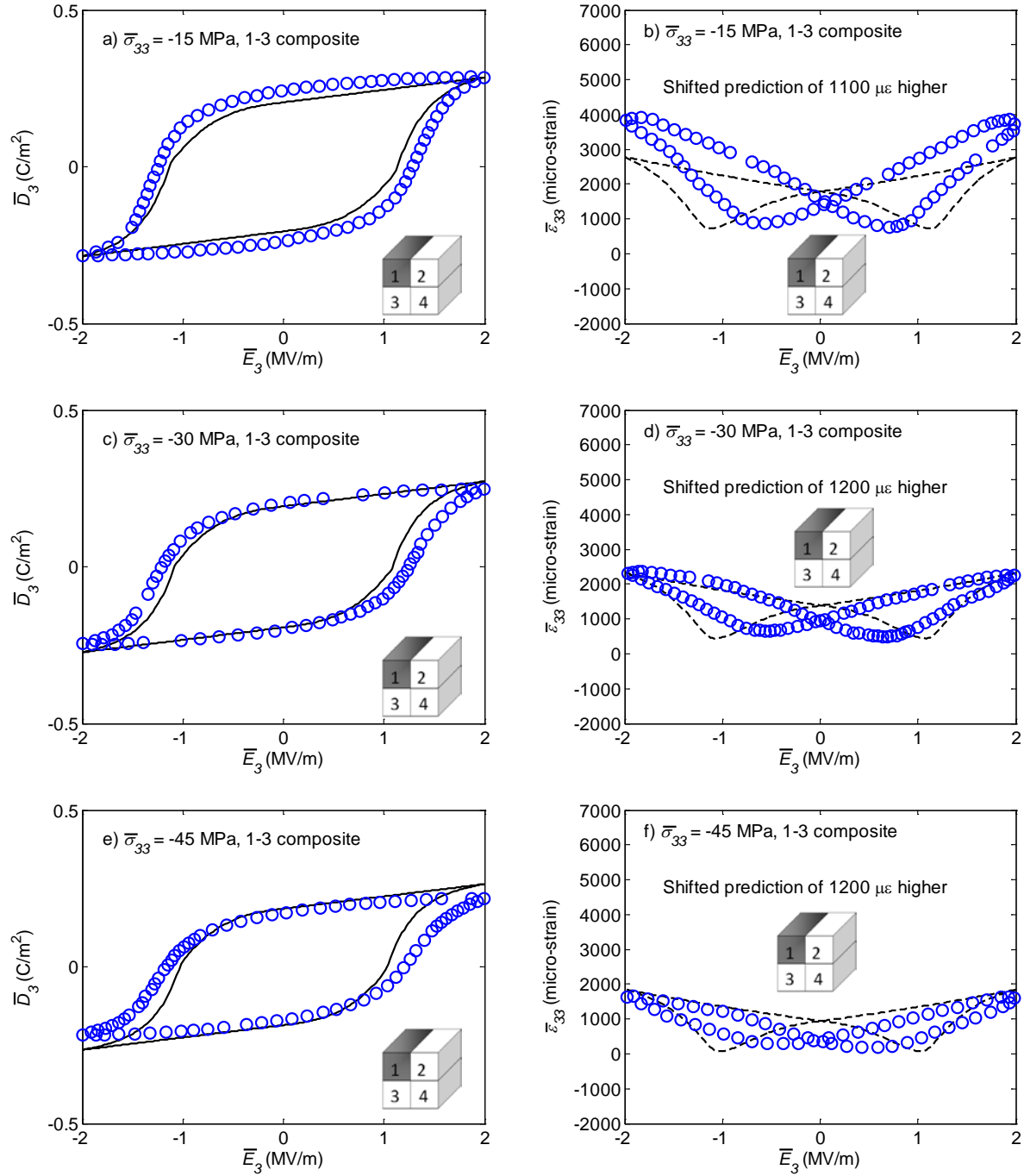


Figure 43 Comparison of micromechanical predictions (solid and dashed lines) to experimental data (circles) of Jayendiran and Arockiarajan (2013) for the hysteretic polarization and butterfly strain responses for the PZT-5A1/epoxy 1-3 active composite with PZT-5A1 fiber VF = 0.8 subjected to both a cyclic electric field and various constant mechanical stresses.

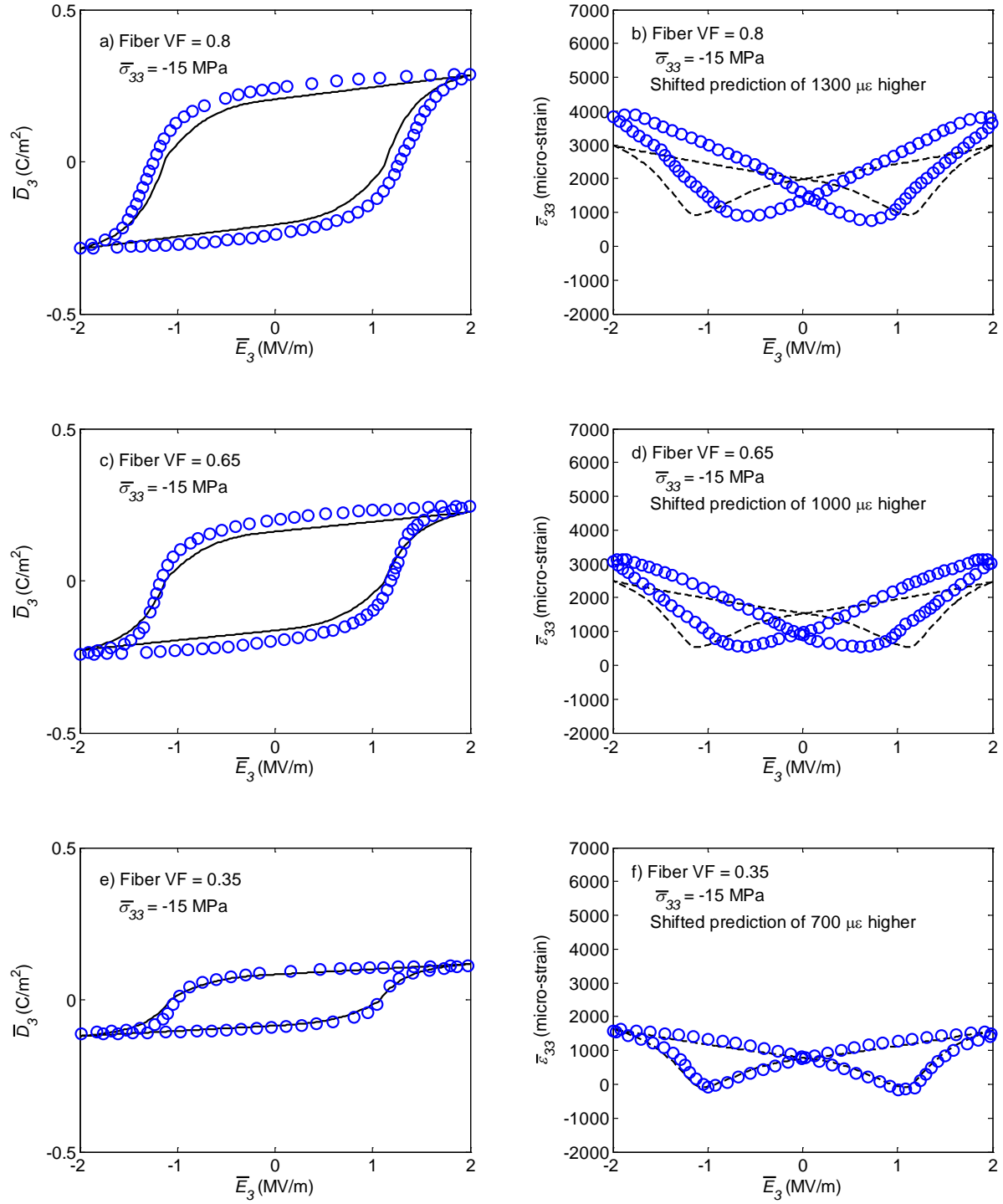


Figure 44 Comparison of micromechanical predictions (solid and dashed lines) to experimental data (circles) of Jayendiran and Arockiarajan (2013) for the hysteretic polarization and butterfly strain responses for the PZT-5A1/epoxy 1-3 active composite with various PZT-5A1 fiber VFs subjected to both a cyclic electric field and a constant mechanical stress.

Parametric studies are conducted in order to understand the electric-field transfers in the particle composites as the active inclusions are not necessarily in direct contact with the electrodes, unlike in active fiber composites. Particle composites with epoxy and silver matrix are considered. Epoxy has relatively low dielectric constants, while silver is a conductive material. Figures 45 and 46 illustrate the polarization and strain responses in particle composites with epoxy and silver matrix, respectively, under cyclic electric fields and a constant compressive stress. As seen in Fig. 45, very small values of effective polarization and strain are generated in the composites, which are due to a low dielectric matrix (non-conductive), and as a result the epoxy matrix is unable to pass significant amount of charges to the active ferroelectric particles. When silver (conductive) matrix is used, significant hysteretic polarization and butterfly strain responses are observed in the composites, even when high compressive stress that can suppress the polarization is prescribed to the composite. This shows that high dielectric constant of the conductive matrix causes the electric charges easily pass through the conductive matrix and eventually large amount of electric fields reaches the PZT-5A1 particles.

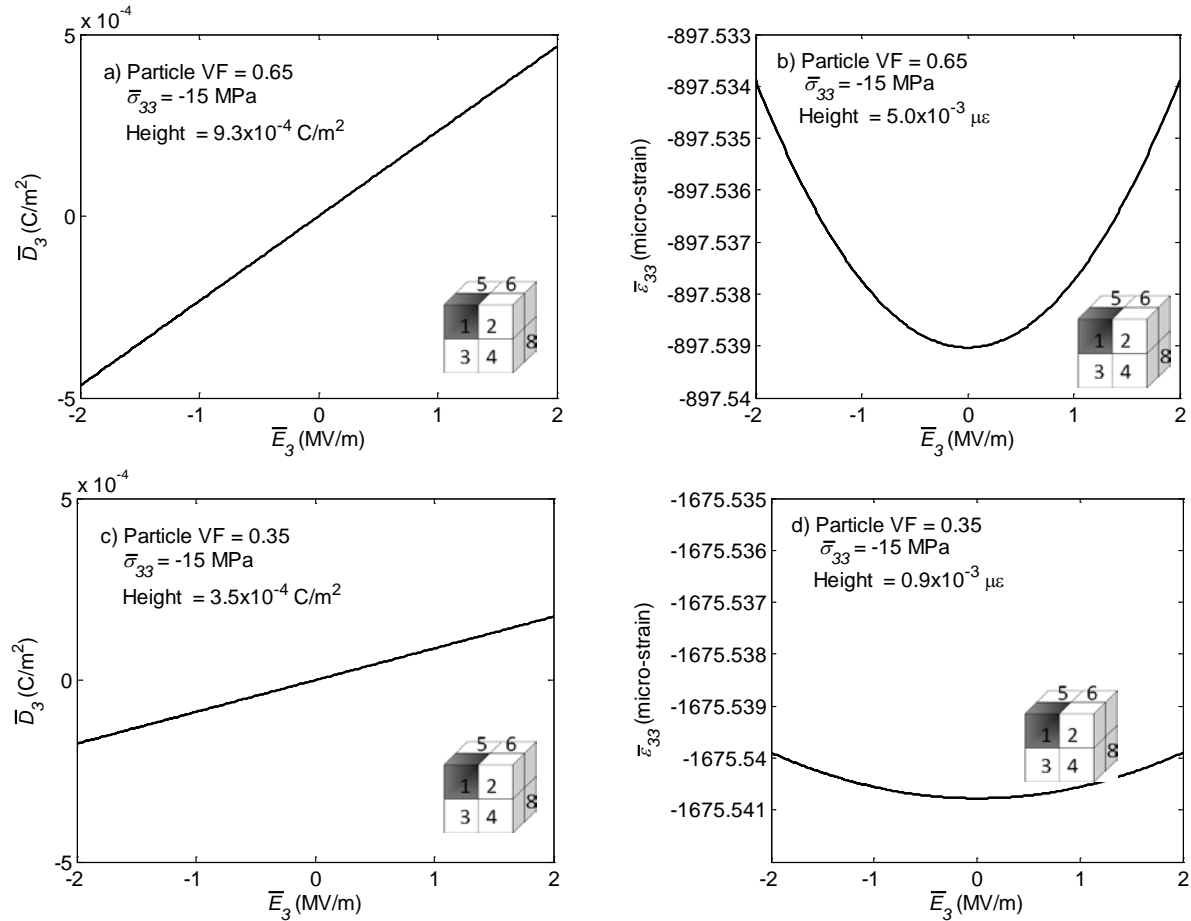


Figure 45 The effective polarization and strain responses for the stress free PZT-5A1/epoxy 0-3 active composite with matrix dielectric constant of 0.04×10^{-9} F/m.

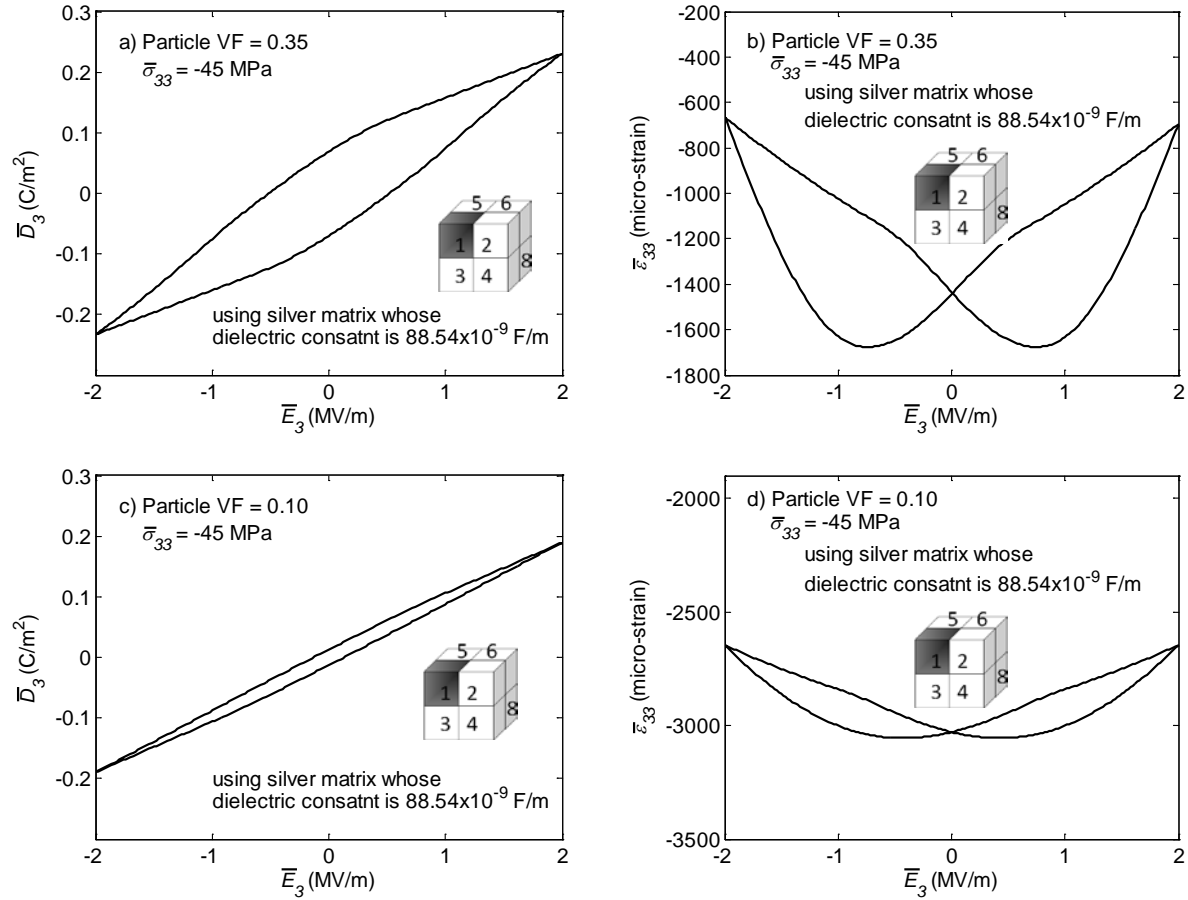


Figure 46 Effective hysteretic polarization and butterfly strain responses for the PZT-5A1/silver 0-3 active composite with PZT-5A1 particle undergoing both a cyclic electric field and a constant mechanical stress $\bar{\sigma}_{33} = -45$ MPa.

c) Response of active functionally graded materials

A piezoelectric bimorph beam, which is formed by bonding two thin layers of piezoelectric ceramic plates, is often used as actuators. An actuating mechanism is induced by applying electric fields through the thickness of the piezoceramics plate so that one of the piezoelectric ceramic plates would elongate in the longitudinal direction and the other plate would contract in the longitudinal direction. The relatively large differences in the deformations, i.e., tension and compression, in the longitudinal direction of the two piezoelectric ceramic plates lead to high stress discontinuities at the interfaces between the piezoelectric plates. The high stress discontinuities at the interface can cause debonding and eventually failure of the piezoelectric bimorph beam. Functionally graded piezoelectric beams (FGPBs) have been considered as one of the promising solutions to relieve the high stress discontinuities at the interface of the piezoelectric ceramic plates by introducing gradual changes in the compositions of the piezoelectric ceramic plates, see for example, Wu et al. (1996), Jin and Meng (2003), Takagi et al. (2002).

This study presents analyses of the nonlinear electro-mechanical response of polarized FGPBs and polarization switching behavior in FGPBs, undergoing small deformation gradients. The lateral deformations in the FGPBs are due to applications of electric fields through the thickness of the beams. The functionally graded beam is discretized into several graded layers through its thickness as shown in Fig. 47. The interfaces between layers are assumed perfectly bonded so that the charge continuously flows through the thickness, i.e., charges in every layer of the FGPBs are assumed uniform. Each layer is comprised of different compositions of the active (piezoelectric) inclusions and conductive matrix, i.e., metallic matrix. The microstructure in each layer is idealized as solid spherical inclusions randomly distributed in a homogeneous matrix and it is assumed that all particles are fully surrounded by homogeneous matrix without any contents of pores and defects. A unit-cell model consisting of eight inclusion and matrix subcells is then considered for obtaining the overall (homogenized) electro-mechanical properties and responses in each layer. The inclusions and the matrix are assumed perfectly bonded and the spatial variations of the field variables in each subcell are assumed uniform. Further discussion on the active functionally graded beams can be found in Lin and Muliana (2014b).

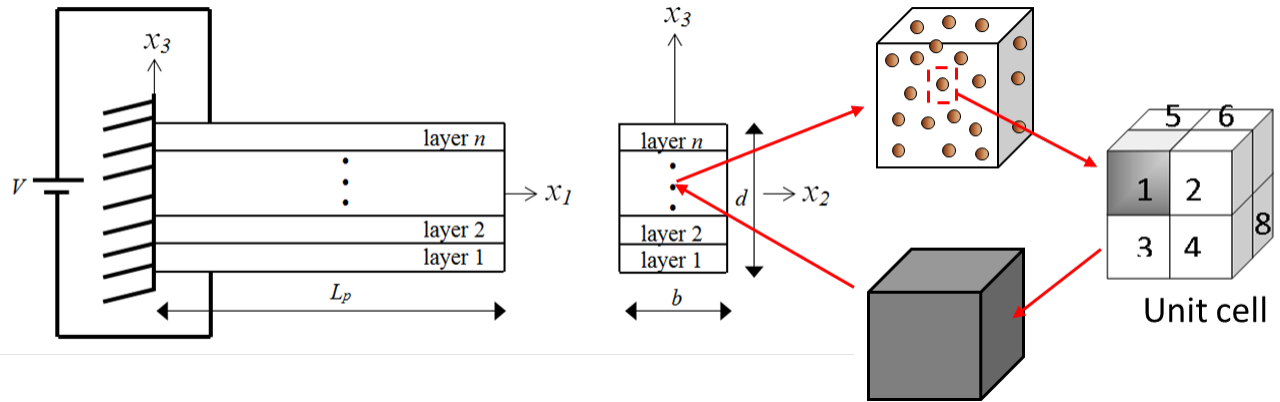


Figure 47 Schematic of a functionally graded piezoelectric beam and its microstructural approximation.

The predictions of the tip deflections and curvatures of the piezoelectric beams are first compared with existing experimental data, which is limited to responses of polarized piezoceramics. Parametric studies are also performed to study the effects of thickness of the beam, constituent volume fraction, and excitation frequency on the overall performance of the beams under cyclic electric field inputs. First, experimental data reported by Alexander and Brei (2005) are used for comparisons. The FGPB consists of PZT-856 and BT constituents with five piezocomposite layers, i.e., pure PZT-856, 0.95/0.05, 0.90/0.10, 0.85/0.15, and 0.80/0.20 VF of PZT-856/BT. Two sides of the beams were electroded with 1500 Å of AuPd. Two possible microstructures of the PZT-856/ barium titanate functionally graded beams are considered since their detailed microstructural morphologies are not discussed in the literature. The first microstructure considers PZT-856 inclusions dispersed in homogeneous barium titanate matrix, in which the PZT inclusions are fully surrounded by barium titanate. The second microstructure is the inverse of the first one. Figure 48 shows the comparisons between the predictions and experimental measurements of the tip deflection of the studied functionally graded beams. The predictions from the PZT-856 inclusions dispersed in the barium titanate matrix (solid lines) are

in good correlations with experimental results. The predictions of the piezocomposite with barium titanate inclusions dispersed in the PZT-856 matrix (dashed lines) underestimate the tip deflection. Another functionally graded piezoelectric beam considered here was developed by Takagi et al. (2002), which consists of platinum (Pt) particles dispersed in polarized PZT matrices. Figure 49 depicts the predictions and experimental data of the curvature of the functionally graded piezoelectric beam against the applied voltage. It is expected that for the low voltage linear theory works well.

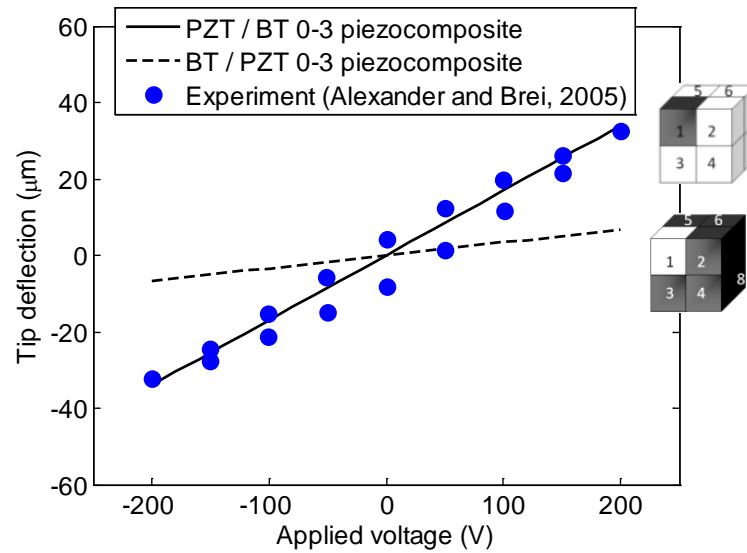


Figure 48 Relationships between a total applied voltage and the tip deflection of the five-layer functionally graded piezoelectric beam.

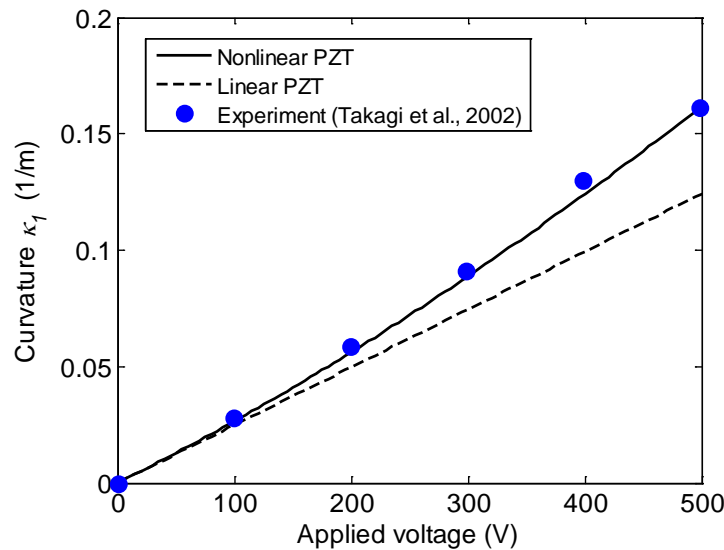


Figure 49 Relationships between a total applied voltage and the curvature of the functionally graded piezoelectric beam. The solid (Nonlinear PZT) and dashed (Linear PZT) lines show the predictions from the model while solid circle symbols are experimental measurements of curvatures.

Parametric studies are now conducted for a functionally graded piezoelectric cantilever beam with five piezocomposite layers undergoing cyclic electric fields in order to examine the effect of polarization switching response on the tip deflections. Each layer has different compositions of PZT-51 particle and Platinum matrix. Higher frequency results in smaller hysteretic responses, as seen in Fig. 50. This is because the PZT-51 constituent does not have enough time to experience “creep-like” behavior at higher frequency.

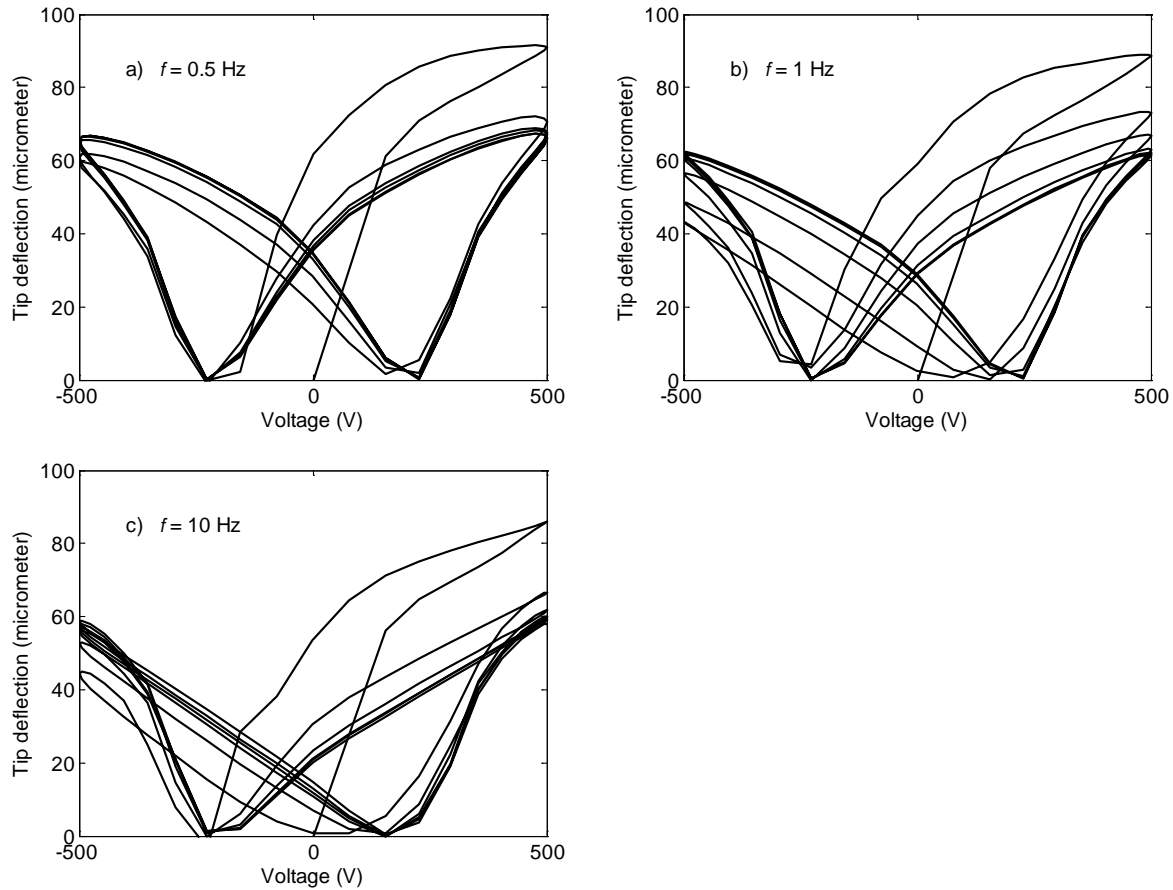


Figure 50 Effect of the excitation frequency, $f =$ a) 0.5, b) 1, and c) 10 Hz, on the tip deflection

4.3.3) Micromechanical models with detailed microstructural morphologies

Micromechanics models with idealized and simplified shapes of inhomogeneities, such as the ones discussed in **Sections 4.3.1** and **4.3.2**, have been widely used to obtain the average (macroscopic) mechanical response of different composite materials. One of the purpose of this study is to examine whether the composites with irregular shapes of inhomogeneities, such as in the aluminum-alumina ($\text{Al-Al}_2\text{O}_3$) and barium titanate-silver ($\text{BaTiO}_3\text{-Ag}$) composites, can be approximated by considering idealized and simplified shapes of inhomogeneities in determining their overall macroscopic mechanical responses. It is noted that $\text{Al-Al}_2\text{O}_3$ composites are often used as host structures in high temperature application, while $\text{BaTiO}_3\text{-Ag}$ composites are promising for active composites used at elevated temperatures.

For this purpose, two composite systems, i.e., Al-Al₂O₃ and BaTiO₃-Ag, are manufactured using powder metallurgy method and characterized for their thermo-mechanical and thermo-electro-mechanical properties.

a) Al-Al₂O₃ composite system

Al-Al₂O₃ composites with different Al₂O₃ contents and particle sizes have been manufactured and studied. Information on processing of the Al-Al₂O₃ composites can be found in Gudlur (2013). The effects of shapes of the inhomogeneities (inclusions and pores) that are randomly dispersed in a homogeneous ductile matrix on the overall thermo-mechanical response of Al-Al₂O₃ composites are examined. The micromechanical models with detailed microstructural morphologies are constructed from the microstructural images of the composites obtained from the scanning electron microscope (SEM). The SEM images of the composites are converted into finite element (FE) meshes using software OOF2¹ and ABAQUS FE code is used to analyze the overall response of the Al-Al₂O₃ composite. Figure 51 shows the SEM image of a composite with 20vol% Al₂O₃, where the alumina particles appear light in color, aluminum matrix in grey, and voids/pores appear dark in color. The size of the microstructural image is 217μm x 173μm. This micrograph image is divided into uniform sub-images (regions). As an example, the image is divided into 12 uniform regions with 50μm x 50μm. Four different 50 μm x 50 μm square regions having different microstructures are randomly chosen as representative microstructures of the composite. Four representative volume elements (RVEs) which are referred as FE meshes 1, 2, 3, and 4 are randomly selected. The overall linear elastic modulus of the composites from the selected RVEs is first studied. Convergence studies in terms of number of elements used in FE analyses and also the sizes of RVE, in which the RVE sizes are varied by selecting two regions with 100μm x 100μm, are performed. The two RVEs are referred as FE meshes 5 and 6. The elastic moduli, determined from different RVE sizes and number of elements, are compared. The FE simulation is carried out in two steps. The first step is prescribing a uniform temperature change from 200°C, which is considered as the stress-free temperature based on a previous work, Gudlur et al. (2014), to 25°C and examining the residual (remaining thermal) stresses.

The linear responses from the FE analyses are first studied and compared to the ones obtained from the experiment using nondestructive testing, resonant ultrasound spectroscopy (RUS). Table 10 presents the values of elastic moduli and Poisson's ratios from the six FE meshes considered. The first four FE meshes (FE-1, FE-2, FE-3, and FE-4) have 50μm x 50μm square region, while FE-5 and FE-5 have 100μm x 100μm square region. The average size of the element in the FE analyses with coarse elements is $3.27 \times 10^{-4} \times 3.27 \times 10^{-4} \text{ mm}^2$, while the one with finer elements is $1.96 \times 10^{-4} \times 1.96 \times 10^{-4} \text{ mm}^2$. The coarse elements are capable in capturing the overall properties of the composites while significantly reduce the computational cost. It is also seen that the smaller RVE size is capable in representing the heterogeneities in composites. For comparison, the overall elastic properties of composites without considering the thermal (residual) stress effect are shown in Table 11. The properties from four FE meshes are compared to the Mori-Tanaka micromechanics model. It is seen that the elastic moduli without the residual stress effect are about 12 GPa higher than the ones with the residual stress effect. It is also noted that the effective elastic properties from the four FE analyses are closed to the ones of Mori-Tanaka model with 20% alumina volume contents, in which an idealized microstructure of a composite with a solid sphere embedded in homogeneous matrix is considered. From the above

¹ <http://www.nist.gov/mml/ctcms/oof/index.cfm>

analyses one can observe that the existence of residual (thermal) stresses in the constituents significantly influence the macroscopic elastic properties of the composites.

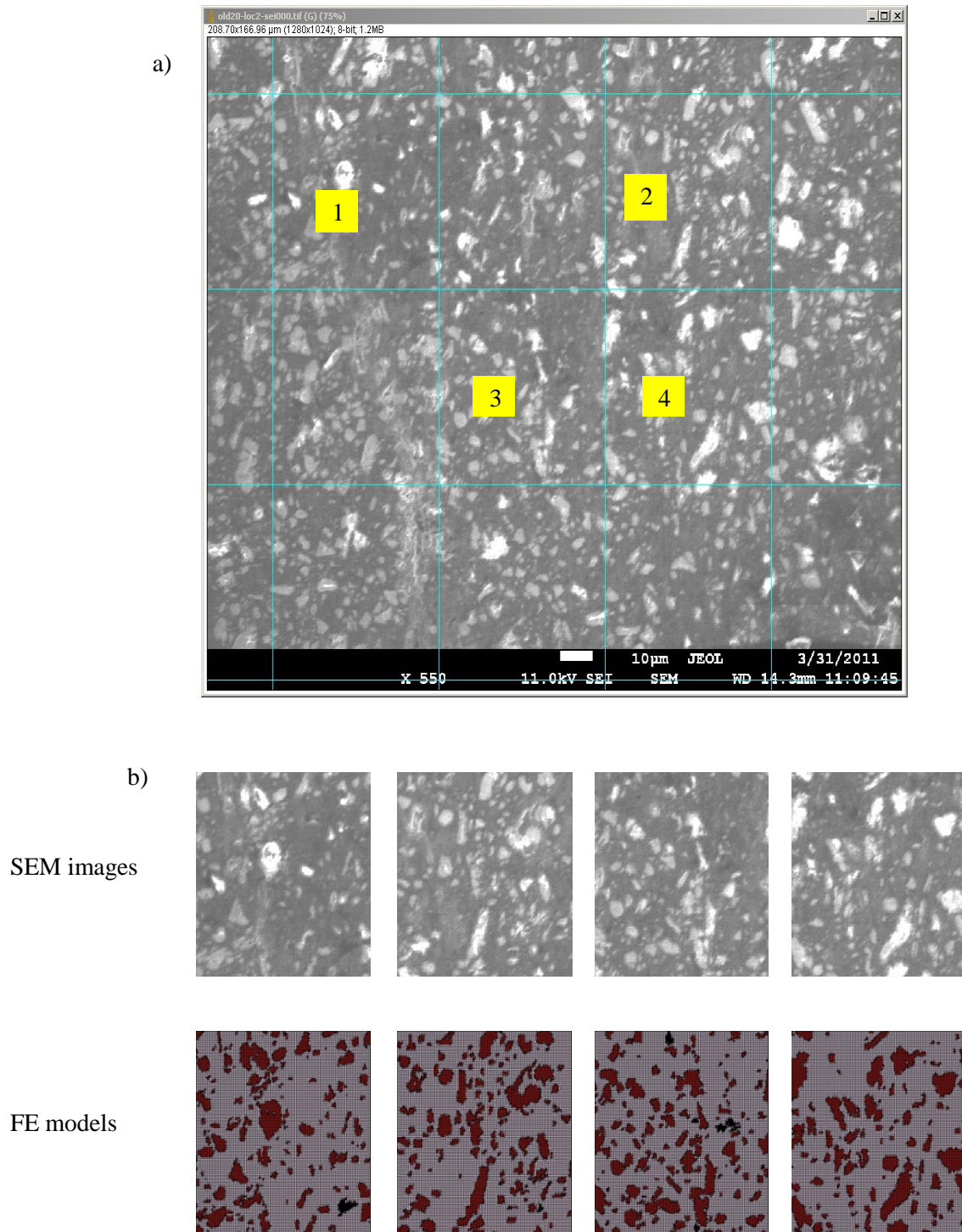


Figure 51 a) SEM Image of Al-Al₂O₃ composite sample with 20% alumina contents; b) Four random square micrographs of the composite sample and their corresponding FE microstructural models 1, 2, 3, and 4

Table 10. Area Fraction of Alumina (%AF), Porosity (%Pores), elastic modulus, and Poisson's ratio of the FE models generated from composite with 20% Volume Fraction (%VF) of alumina. For comparison, results of the experiment from the nondestructive testing, resonant ultrasound spectroscopy (RUS), are also provided in the table.

| Model | %AF of Alumina | %Pores | E (GPa) | ν |
|-------|----------------|--------|--|-------------|
| FE-1 | 20.2 | 0.4 | 71.23 ^a /70.82 ^b | 0.397/0.402 |
| FE-2 | 21.7 | 0.1 | 72.57/72.15 | 0.393/0.399 |
| FE-3 | 20.9 | 0.7 | 69.44/69.06 | 0.390/0.395 |
| FE-4 | 21.2 | 0.0 | 75.53/75.08 | 0.393/0.395 |
| FE-5 | 21.7 | 0.3 | 71.43 | 0.405 |
| FE-6 | 19.1 | 0.8 | 70.03 | 0.396 |
| RUS | 22.6 | 0.5 | 75.15 | 0.310 |

^ausing coarse meshes; ^busing finer meshes

Table 11 Effective elastic properties of composites with 20% VF of alumina, without residual (thermal) stress effect

| Model | E (GPa) | ν |
|-------------|-----------|-------|
| FE-1 | 83.28 | 0.313 |
| FE-2 | 86.67 | 0.311 |
| FE-3 | 83.70 | 0.314 |
| FE-4 | 88.05 | 0.315 |
| Mori Tanaka | 87.00 | 0.330 |

The second micromechanics model is constructed by considering idealized shapes of the inhomogeneities, while maintaining the same volume contents and locations of the inhomogeneities as the ones in the micromechanics model with microstructural details. In this case, the overall inelastic and degradation responses, incorporating the thermal stress effect, from the detailed microstructural characteristics is compared to the ones determined with idealized microstructures. The alumina is modeled as linear elastic while the aluminum is assumed to exhibit an elastic-plastic deformation following the Hencky-Ilyushin model. In order to incorporate the degradation in the ceramics caused by relatively high localized tensile stresses/strains, the following rate degradation model for the ceramics is used $\dot{d} = (1-d)f(\epsilon_{ij})$, where f is the general function of strains. The elastic property, i.e., elastic modulus, of the ceramics changes with the degradation, $E(d)$. It is noted that this study does not aim at rigorously model the degradation in the composite constituents, instead it is done to briefly examine the overall macroscopic response of composites in case of some localized degradation occurs in the constituents. Figure 52 illustrates the stress and degradation fields in FE meshed model #1. As seen in the figures, the composite with actual shapes of inhomogeneities shows stress and degradation fields with higher magnitude as compared to the composite with circular shapes of inhomogeneities, especially in the brittle inclusions. It is noted that sharp edges of the inhomogeneities in the microstructures with actual shapes of inhomogeneities lead to high localized stresses. Figure 53 presents the corresponding overall responses from the two micromechanics models, which show very close stress-strain behaviors.

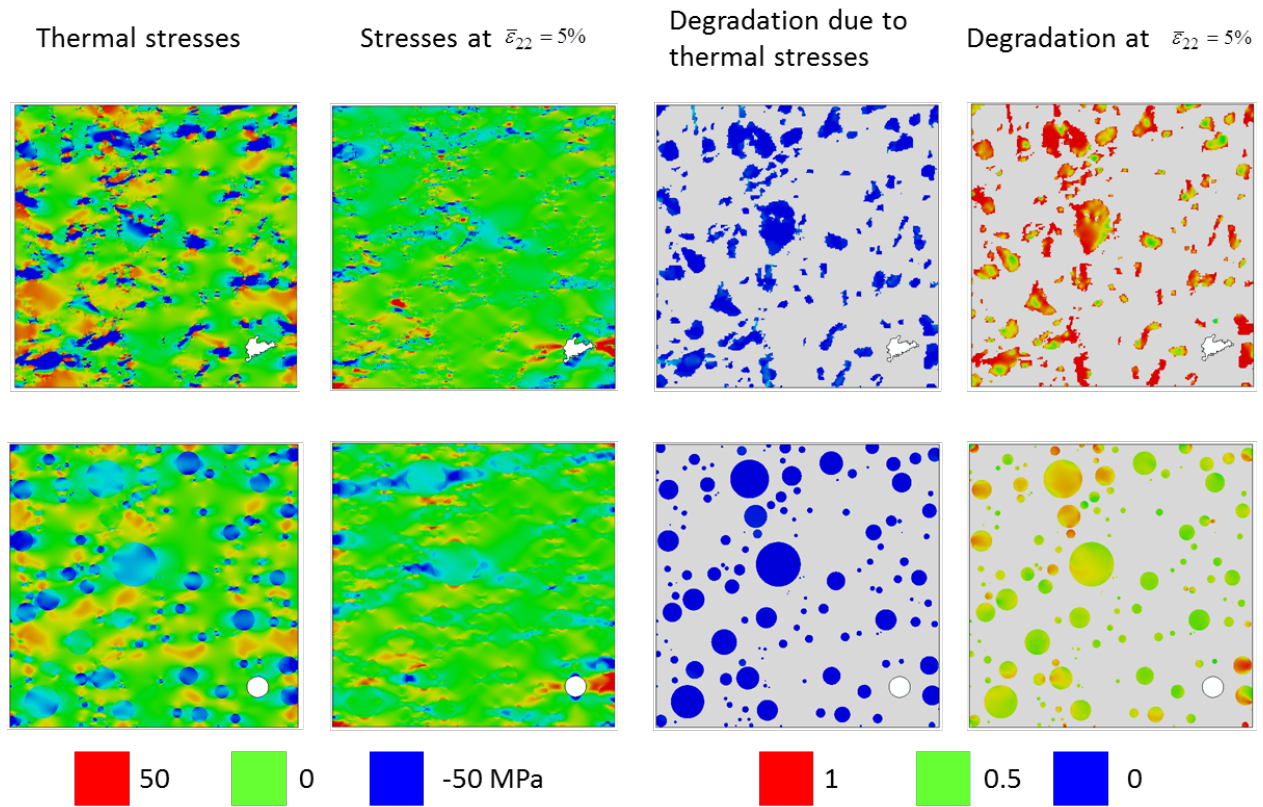


Figure 52 Transverse stress and degradation contours from FE meshed model#1 with actual (top) and idealized (bottom) inhomogeneities

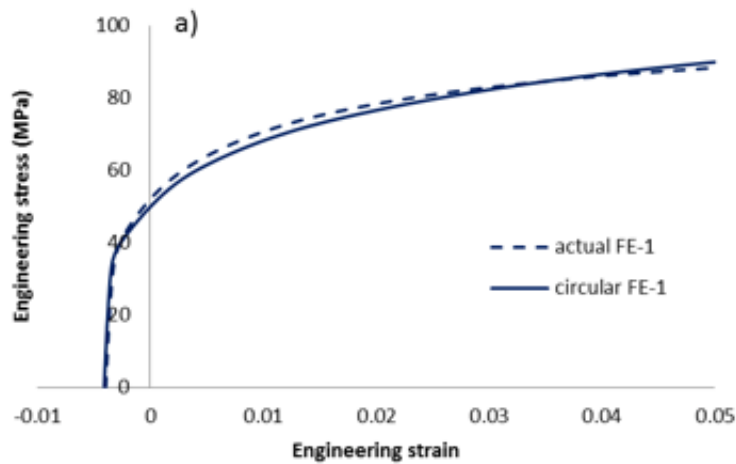


Figure 53 Macroscopic (effective) stress-strain responses of the Al-Al₂O₃ composite with actual and idealized microstructures.

b) BaTiO₃-Ag composite system

BaTiO₃-Ag composites with different silver contents have been manufactured and studied. Some information on the manufacturing and testing of BaTiO₃-Ag composites can be found in Xing et al. (2013). Similar to the Al-Al₂O₃ composites, micromechanics models of BaTiO₃-Ag composites with microstructural details are formulated, see Fig. 54 as an example. The micromechanics models are used to study the thermal, electrical, and mechanical properties of the composites at different temperatures: -50°C to 250°C. Phase transformations in the BaTiO₃ are observed around 25°C and 125°C. Figure 54 shows the thermal expansion coefficient of BaTiO₃-Ag composites with different silver contents and at three different phases, while Fig. 56 illustrates the thermal conductivity at room temperature. The micromechanical models are capable in capturing the overall thermal properties of composites. Similar predictions are done on the mechanical and electrical properties.

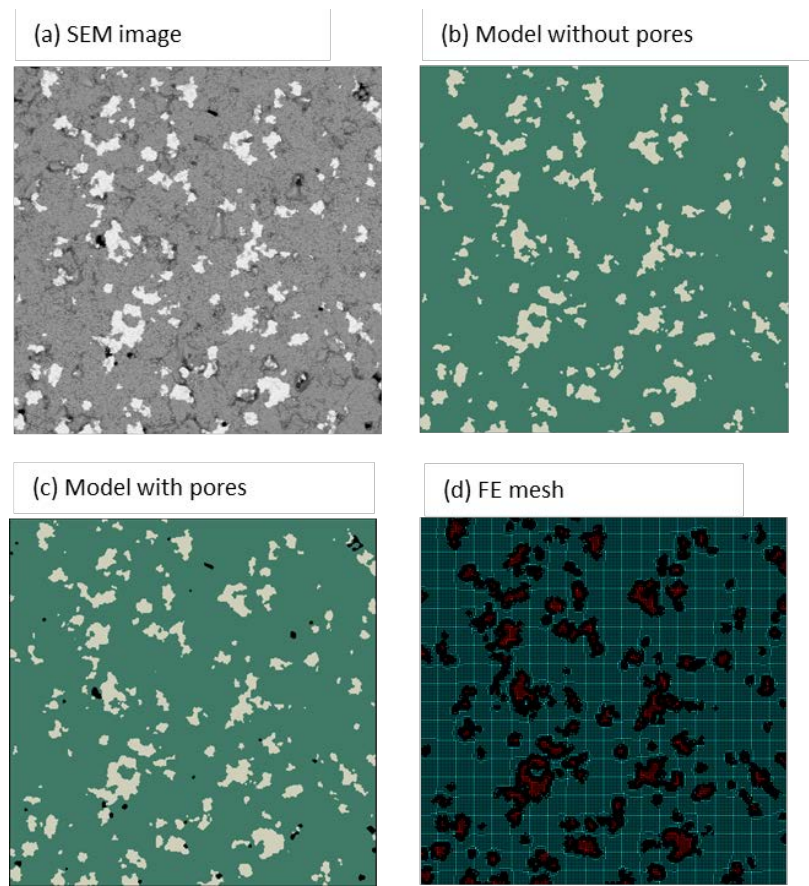


Figure 54 Example of microstructural model of BaTiO₃-Ag with 10% silver content

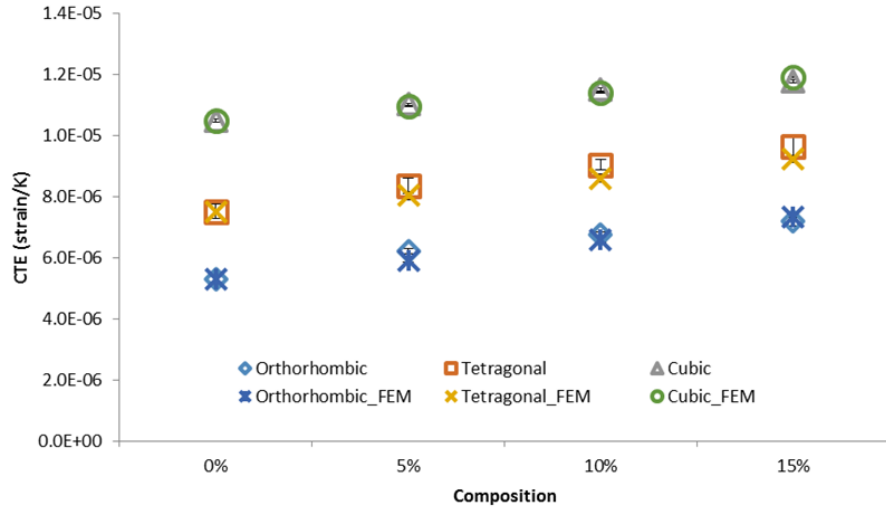


Figure 55 Thermal expansion coefficient of BaTiO₃-Ag at different phases and silver contents

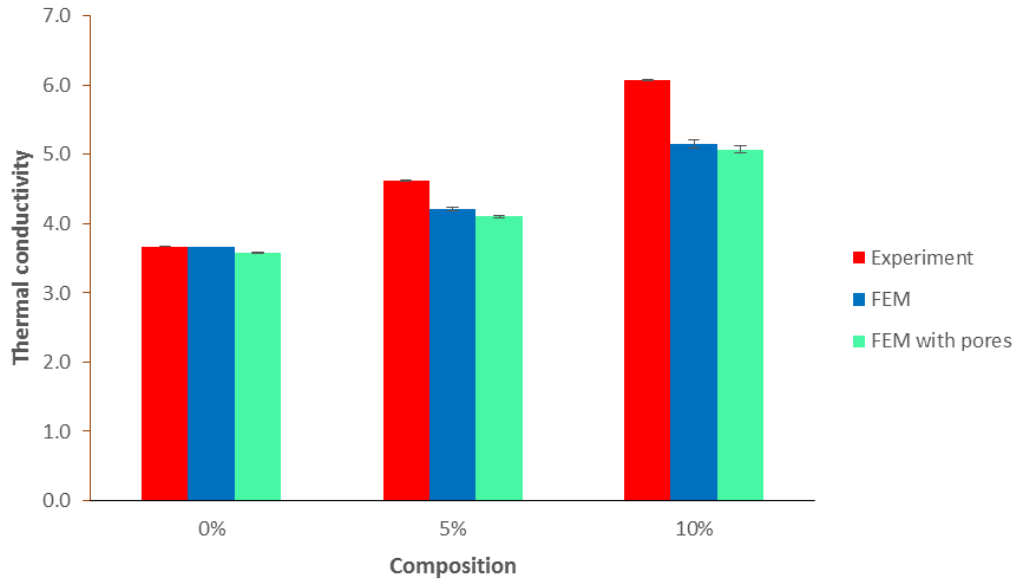


Figure 56 Thermal conductivity response of BaTiO₃-Ag at room temperature

4.4) Structural Analyses

Multi-level homogenization schemes that incorporate different constitutive material models of the constituents and microstructural details have been formulated for predicting the effective response of structures comprising of heterogeneous materials. In multi-scale models, numerical methods are often used to find solutions to boundary value problems (BVPs) at multiple length-scales. In this project, a multi-scale model is formulated based on an integrated simplified micromechanical model and FE framework, which is used to analyze nonlinear time-dependent

thermo-electro-mechanical responses of smart structures. The smart structures can comprise of a) composite host structures integrated with active materials made of piezoceramics or active composites, b) arrangements of active and inactive components of various materials. The purpose is to perform shape changes in the smart structures controlled by the electro-active components.

In this study, coupled transient heat conduction and thermo-electro-mechanical responses are considered. Finite element (FE) method is used to obtain solutions to BVPs in the active structures. It is assumed that the heat conduction influences the electro-elastic response, but the electro-elastic deformations do not influence the heat conduction in the active materials, allowing for sequentially coupled heat conduction and deformation analyses. When fully coupled heat conduction is considered, user subroutine materials UMAT and UMATH within ABAQUS FE are used in order to determine the solutions to field variables, see Khan and Muliana (2012b).

The multi-scale analyses of heat conduction and thermo-electro-mechanical deformations within 3D continuum finite elements are briefly summarized as follows. Let $\{\bar{\mathbf{T}}^n\}^T = \{\bar{T}^1, \bar{T}^2, \dots, \bar{T}^{Nd}\}^T$ be the nodal temperatures in a continuum element with number of nodes Nd . An overbar indicates the macro-scale quantities and \mathbf{T} denotes transpose of a vector or matrix. The temperature gradients at the macro-level, which are sampled at material (Gaussian) points, are given as:

$$\bar{\phi}_j = -\frac{\partial \bar{T}}{\partial x_j} = B_{jk}^T \bar{T}_k^n \quad \text{or} \quad \bar{\phi} = \mathbf{B}^T \bar{\mathbf{T}}^n \quad (28)$$

where \mathbf{B}^T is the gradient matrix. Using the principle of virtual work the energy balance equation when only heat conduction is considered, is:

$$\begin{aligned} \int_V \mathbf{N}^T \bar{C}_v \mathbf{N} dV \dot{\bar{\mathbf{T}}}^n + \int_V \mathbf{B}^{T^T} \bar{\mathbf{K}} \mathbf{B}^T dV \bar{\mathbf{T}}^n &= \int_V \mathbf{N}^T \bar{r} dV + \int_A \mathbf{N}^T \bar{f} dA \\ \bar{\mathbf{C}}^T \dot{\bar{\mathbf{T}}}^n + \bar{\mathbf{K}}^T \bar{\mathbf{T}}^n &= \bar{\mathbf{R}}^r + \bar{\mathbf{R}}^f; \quad \dot{\bar{\mathbf{T}}}^n = \frac{d\bar{\mathbf{T}}^n}{dt} \end{aligned} \quad (29)$$

where \mathbf{N} is the shape function matrix, \bar{C}_v is the macro-scale heat capacity; \bar{k}_{ij} is the component of the macro-scale (effective) thermal conductivity; and \bar{r} and \bar{f} are the rate of internal heat generation per unit volume and surface heat flux, respectively; V is the volume of the body, and A is the surface area where the heat flux is prescribed. A general element should be able of incorporating any orientation in a global coordinate system. This can be done through rotational tensor transformations. Macro-scale thermal and physical properties, i.e., \bar{k}_{ij} and \bar{C}_v are needed

in order to form $\bar{\mathbf{C}}^T$ and $\bar{\mathbf{K}}^T$ matrices. When homogeneous materials are considered, the heat conductivity and heat capacity of the homogeneous materials can be used directly. In case composite materials are considered, the effective properties discussed in **Section 4.3.1** are used. It is noted that if heat conduction through an active body causes significant temperature changes in the body, variations of the thermal conductivity and heat capacity with temperatures are not negligible, leading to a nonlinear problem. In order to obtain solutions for the temperature field at the macro-scale, backward difference method for the temporal integration and Gaussian quadrature method for the spatial integration are adopted. At each time increment, a linearized relation in Eq. (29) is used as a starting point for obtaining the temperature field at current time

and the Newton-Raphson iterative method is then used to correct for errors due to linearization. Let Δt be an incremental time and the temperature time derivative at current time $(t + \Delta t)$ is

approximated as: $\dot{\bar{\mathbf{T}}}_{t+\Delta t}^n \approx \frac{\bar{\mathbf{T}}_{t+\Delta t}^n - \bar{\mathbf{T}}_t^n}{\Delta t}$; where $\bar{\mathbf{T}}_t^n$ is the nodal temperature at previous time t and

$\bar{\mathbf{T}}_0^n$ refers to initial conditions for the nodal temperatures. If the internal heat generation is absent and the surface heat flux is the external stimuli, then $\bar{\mathbf{R}}^{ext} = \bar{\mathbf{R}}^f$. With material properties vary with temperatures, the linearized equilibrium equation for an entire structure is now written as:

$$\bar{\mathbf{C}}_{t+\Delta t}^T \dot{\bar{\mathbf{T}}}_{t+\Delta t}^n + \bar{\mathbf{K}}_{t+\Delta t}^T \bar{\mathbf{T}}_{t+\Delta t}^n = \bar{\mathbf{R}}_{t+\Delta t}^{ext} \quad (30)$$

A multi-scale time-integration algorithm is formulated to obtain solutions for nodal temperatures in Eq. (28), which is summarized as follows:

- 1) Input variables: Δt , $\bar{\mathbf{T}}_t^n$, $\bar{\mathbf{K}}_t^T$, $\bar{\mathbf{C}}_t^T$, and $\bar{\mathbf{R}}_{t+\Delta t}^{ext}$
 - 2) Calculate $\bar{\mathbf{T}}_{t+\Delta t}^{n,k}$ (linearized solution, iteration counter $k=0$): $\left(\frac{1}{\Delta t} \bar{\mathbf{C}}_t^T + \bar{\mathbf{K}}_t^T\right) \bar{\mathbf{T}}_{t+\Delta t}^{n,0} = \bar{\mathbf{R}}_{t+\Delta t}^{ext} + \frac{1}{\Delta t} \bar{\mathbf{C}}_t^T \bar{\mathbf{T}}_t^n$
 - 3) Iterate for $k=0,1,2, \dots$
 - 3.1) Evaluate: $\bar{\mathbf{T}}_{t+\Delta t}^{n,k} = \mathbf{N} \bar{\mathbf{T}}_{t+\Delta t}^{n,k}$; $T_{t+\Delta t}^{(m),k} = \bar{T}_{t+\Delta t}^{n,k}$ where (m) indicates subcell's number;
 $\mathbf{k}_{t+\Delta t}^{(m),k} \equiv \mathbf{k}^{(m)}(T_{t+\Delta t}^{(m),k})$; $\bar{\mathbf{k}}_{t+\Delta t}^k$ from Eq. (3.5)
 $C_{v,t+\Delta t}^{(m),k} \equiv C_v^{(m)}(T_{t+\Delta t}^{(m),k})$; $\bar{C}_{v,t+\Delta t}^k$ from Eq. (3.6)
 $\bar{\mathbf{C}}_{t+\Delta t}^{T,k}$ and $\bar{\mathbf{K}}_{t+\Delta t}^{T,k}$ from Eq. (3.2)
 - 3.2) Define residual vector: $\bar{\mathbf{R}}_{res}^k = \bar{\mathbf{R}}_{t+\Delta t}^{ext} - \bar{\mathbf{C}}_{t+\Delta t}^{T,k} \frac{\bar{\mathbf{T}}_{t+\Delta t}^{n,k} - \bar{\mathbf{T}}_t^n}{\Delta t} - \bar{\mathbf{K}}_{t+\Delta t}^{T,k} \bar{\mathbf{T}}_{t+\Delta t}^{n,k}$

IF $\|\bar{\mathbf{R}}_{res}^k\| \leq Tol$ THEN proceed to step 4), ELSE
 - 3.3) Correct for $\bar{\mathbf{T}}_{t+\Delta t}^{n,k+1} = \bar{\mathbf{T}}_{t+\Delta t}^{n,k} + \left[\frac{\partial \bar{\mathbf{R}}_{res}^k}{\partial \bar{\mathbf{T}}_{t+\Delta t}^n}\right]^{-1} \bar{\mathbf{R}}_{res}^k$ and go back to step 3.1)
- where $\left[\frac{\partial \bar{\mathbf{R}}_{res}^k}{\partial \bar{\mathbf{T}}_{t+\Delta t}^n}\right] = -\frac{1}{\Delta t} \bar{\mathbf{C}}_{t+\Delta t}^{T,k} - \frac{\partial \bar{\mathbf{C}}_{t+\Delta t}^{T,k}}{\partial \bar{\mathbf{T}}_{t+\Delta t}^n} \frac{1}{\Delta t} (\bar{\mathbf{T}}_{t+\Delta t}^{n,kT} - \bar{\mathbf{T}}_t^n) - \bar{\mathbf{K}}_{t+\Delta t}^{T,k} - \frac{\partial \bar{\mathbf{K}}_{t+\Delta t}^{T,k}}{\partial \bar{\mathbf{T}}_{t+\Delta t}^n} \bar{\mathbf{T}}_{t+\Delta t}^{n,kT}$
- In order to define the above Jacobian matrix, the variations of the macro-scale thermal conductivity and heat capacity with nodal temperatures are needed:
- $$\frac{\partial \bar{\mathbf{k}}_{t+\Delta t}^k}{\partial \bar{\mathbf{T}}_{t+\Delta t}^n} = \frac{1}{V} \sum_{m=1}^N V^{(m)} \left(\frac{\partial \mathbf{k}_{t+\Delta t}^{(m),k}}{\partial T_{t+\Delta t}^{(m),k}} \mathbf{F}_{t+\Delta t}^{(m),k} + \mathbf{k}_{t+\Delta t}^{(m),k} \frac{\partial \mathbf{F}_{t+\Delta t}^{(m),k}}{\partial T_{t+\Delta t}^{(m),k}} \right)$$
- $$\frac{\partial \bar{C}_{v,t+\Delta t}^k}{\partial \bar{\mathbf{T}}_{t+\Delta t}^n} = \frac{1}{V} \sum_{m=1}^N V^{(m)} \frac{\partial C_{v,t+\Delta t}^{(m),k}}{\partial T_{t+\Delta t}^{(m),k}}$$
- 4) Output variables: $\bar{\mathbf{T}}_{t+\Delta t}^n$, $\bar{\mathbf{K}}_{t+\Delta t}^T$, $\bar{\mathbf{C}}_{t+\Delta t}^T$

The above time-integration algorithm is formulated to solve for the nonlinear heat conduction equations at multiple length scales: homogeneous constituents, microscopic structures of active composites, and global active structures.

Similar to the heat conduction analyses, the corresponding thermo-electro-elastic response of the structure subjected to external mechanical and non-mechanical stimuli can be determined. Let $\{\bar{\mathbf{U}}^n\}^T = \{\bar{u}_1^1, \bar{u}_2^1, \bar{u}_3^1, \dots, \bar{u}_1^{Nd}, \bar{u}_2^{Nd}, \bar{u}_3^{Nd}\}$ and $\{\bar{\Phi}^n\}^T = \{\bar{\phi}^{-1}, \bar{\phi}^{-2}, \dots, \bar{\phi}^{-Nd}\}$ be the nodal displacement and electric potential vectors, respectively. The strain and electric field at the macro-level are defined as:

$$\bar{\varepsilon}_{ij} = \frac{1}{2}(\bar{u}_{i,j} + \bar{u}_{j,i}) = B_{ijm}^u \bar{U}_m^n \quad \text{or} \quad \bar{\boldsymbol{\varepsilon}} = \mathbf{B}^u \bar{\mathbf{U}}^n \quad (31-1)$$

$$\bar{E}_i = -\frac{\partial \bar{\phi}}{\partial x_i} = B_{im}^\phi \bar{\Phi}_m^n \quad \text{or} \quad \bar{\mathbf{E}} = \mathbf{B}^\phi \bar{\Phi}^n \quad (31-2)$$

where \mathbf{B}^u and \mathbf{B}^ϕ are the spatial derivative of shape functions related to the macro-scale strain and electric field, respectively. The energy balance equations related to the mechanical and electrical components in linearized forms are (in absences of body forces and body charges):

$$\int_V \left(\mathbf{B}^{uT} \left[\bar{\mathbf{C}} \mathbf{B}^u \bar{\mathbf{U}}^n - \bar{\mathbf{e}}^T \mathbf{B}^\phi \bar{\Phi}^n - \bar{\boldsymbol{\beta}} \mathbf{N} \bar{\mathbf{T}}^n \right] \right) dV = \int_A \mathbf{N}^T \bar{\mathbf{t}} dA \quad (32-1)$$

$$\begin{aligned} \bar{\mathbf{K}}^{uu} \bar{\mathbf{U}}^n - \bar{\mathbf{K}}^{u\phi} \bar{\Phi}^n &= \bar{\mathbf{F}}^{uT} + \bar{\mathbf{R}}^{ts} \\ \int_V \left(\mathbf{B}^{\phi T} \left[\bar{\mathbf{e}} \mathbf{B}^u \bar{\mathbf{U}}^n + \bar{\mathbf{\kappa}} \mathbf{B}^\phi \bar{\Phi}^n + \bar{\mathbf{p}} \mathbf{N} \bar{\mathbf{T}}^n \right] \right) dV &= \int_A \mathbf{N}^T \bar{q}^s dA \\ \bar{\mathbf{K}}^{\phi u} \bar{\mathbf{U}}^n + \bar{\mathbf{K}}^{\phi\phi} \bar{\Phi}^n &= -\bar{\mathbf{F}}^{\phi T} + \bar{\mathbf{R}}^q \end{aligned} \quad (32-2)$$

where \bar{t}_i and \bar{q}^s denote the components of the surface traction and surface charge, respectively, prescribed at the macro-scale. The components of the electro-elastic coupling $\bar{\mathbf{K}}^{u\phi}$ and dielectric $\bar{\mathbf{K}}^{\phi\phi}$ stiffness matrices depend on the potential gradient at current time. The nodal temperatures

$\bar{\mathbf{T}}^n$ are obtained by first solving the heat conduction equation. Since this study consider nonlinear time-dependent thermo-electro-mechanical responses, the linearized relations in Eq. (32) are obtained at each time increment in order to provide trial solutions of the nodal displacements and electric potential and the Newton-Raphson iterative method is then used to correct for errors from the linearization. The multi-scale analyses at current time ($t_{t+\Delta t} = t + \Delta t$) after assembling of elements are summarized as follows.

1) Input variables are Δt , $\bar{\mathbf{T}}_{t+\Delta t}^n$, $\bar{\mathbf{K}}_t^{uu}$, $\bar{\mathbf{K}}_t^{u\phi}$, $\bar{\mathbf{K}}_t^{\phi u}$, $\bar{\mathbf{K}}_t^{\phi\phi}$, $\bar{\mathbf{R}}_{t+\Delta t}^{ts}$ and $\bar{\mathbf{R}}_{t+\Delta t}^q$

2) Evaluate $\bar{T}_{t+\Delta t} = \mathbf{N} \bar{\mathbf{T}}_{t+\Delta t}^n$; $T_{t+\Delta t}^{(m)} = \bar{T}_{t+\Delta t}$ where (m) indicates subcell's number;

$$\mathbf{C}_{t+\Delta t}^{(m)}, \mathbf{e}_{t+\Delta t}^{(m)}, \hat{\mathbf{b}}_{t+\Delta t}^{(m)}, \hat{\mathbf{\kappa}}_{t+\Delta t}^{(m)}, \boldsymbol{\chi}_{t+\Delta t}^{(m)}, \boldsymbol{\beta}_{t+\Delta t}^{(m)}, \mathbf{p}_{t+\Delta t}^{(m)}$$

$$\bar{\mathbf{F}}_{t+\Delta t}^{uT} \text{ and } \bar{\mathbf{F}}_{t+\Delta t}^{\phi T}$$

$$\bar{\mathbf{K}}_{t+\Delta t}^{uu} \text{ and } \bar{\mathbf{K}}_{t+\Delta t}^{\phi u}$$

3) Calculate $\bar{\mathbf{U}}_{t+\Delta t}^{n,k}$ and $\bar{\Phi}_{t+\Delta t}^{n,k}$ for $k=0$ (trial solutions):

$$\bar{\mathbf{K}}_t^{uu} \bar{\mathbf{U}}_{t+\Delta t}^{n,0} - \bar{\mathbf{K}}_t^{u\phi} \bar{\Phi}_{t+\Delta t}^{n,0} = \bar{\mathbf{F}}_{t+\Delta t}^{uT} + \bar{\mathbf{R}}_{t+\Delta t}^{ts}$$

$$\bar{\mathbf{K}}_t^{\phi u} \bar{\mathbf{U}}_{t+\Delta t}^{n,0} + \bar{\mathbf{K}}_t^{\phi\phi} \bar{\Phi}_{t+\Delta t}^{n,0} = -\bar{\mathbf{F}}_{t+\Delta t}^{\phi T} + \bar{\mathbf{R}}_{t+\Delta t}^q$$

4) Iterate for $k=0,1,2, \dots$

4.1) Evaluate: $\bar{\mathbf{e}}_{t+\Delta t}^k = \mathbf{B}^u \bar{\mathbf{U}}_{t+\Delta t}^{n,k}$, $\bar{\mathbf{E}}_{t+\Delta t}^k = \mathbf{B}^\phi \bar{\Phi}_{t+\Delta t}^{n,k}$, $\bar{\mathbf{K}}_{t+\Delta t}^{u\phi,k}$ and $\bar{\mathbf{K}}_{t+\Delta t}^{\phi\phi,k}$

4.2) Define residual vector: $\bar{\mathbf{R}}_{res}^k = \begin{Bmatrix} \bar{\mathbf{F}}_{t+\Delta t}^{uT} + \bar{\mathbf{R}}_{t+\Delta t}^{ts} - \bar{\mathbf{K}}_{t+\Delta t}^{uu} \bar{\mathbf{U}}_{t+\Delta t}^{n,k} + \bar{\mathbf{K}}_{t+\Delta t}^{u\phi,k} \bar{\Phi}_{t+\Delta t}^{n,k} \\ -\bar{\mathbf{F}}_{t+\Delta t}^{\phi T} + \bar{\mathbf{R}}_{t+\Delta t}^q - \bar{\mathbf{K}}_{t+\Delta t}^{\phi u} \bar{\mathbf{U}}_{t+\Delta t}^{n,k} - \bar{\mathbf{K}}_{t+\Delta t}^{\phi\phi,k} \bar{\Phi}_{t+\Delta t}^{n,k} \end{Bmatrix}$

IF $\|\bar{\mathbf{R}}_{res}^k\| \leq Tol$ THEN proceed to step 5), ELSE

4.3) Correct for $\{\bar{\mathbf{X}}^{k+1}\} = \{\bar{\mathbf{X}}^k\} + \left[\frac{\partial \bar{\mathbf{R}}_{res}^k}{\partial \bar{\mathbf{X}}} \right]^{-1} \bar{\mathbf{R}}_{res}^k$; $\{\bar{\mathbf{X}}^k\} = \begin{Bmatrix} \bar{\mathbf{U}}_{t+\Delta t}^{n,k} \\ \bar{\Phi}_{t+\Delta t}^{n,k} \end{Bmatrix}$ and go back to step 4.1)

$$\text{where } \left[\frac{\partial \bar{\mathbf{R}}_{res}^k}{\partial \bar{\mathbf{X}}} \right] = \begin{bmatrix} -\bar{\mathbf{K}}_{t+\Delta t}^{uu} + \bar{\mathbf{K}}_{t+\Delta t}^{u\phi,k} + \frac{\partial \bar{\mathbf{K}}_{t+\Delta t}^{u\phi,k}}{\partial \bar{\Phi}_{t+\Delta t}^{n,k}} \bar{\Phi}_{t+\Delta t}^{n,k} \\ -\bar{\mathbf{K}}_{t+\Delta t}^{\phi u} - \bar{\mathbf{K}}_{t+\Delta t}^{\phi\phi,k} - \frac{\partial \bar{\mathbf{K}}_{t+\Delta t}^{\phi\phi,k}}{\partial \bar{\Phi}_{t+\Delta t}^{n,k}} \bar{\Phi}_{t+\Delta t}^{n,k} \end{bmatrix}$$

5) Output variables: $\bar{\mathbf{U}}_{t+\Delta t}^n$, $\bar{\Phi}_{t+\Delta t}^n$, $\bar{\mathbf{K}}_{t+\Delta t}^{uu}$, $\bar{\mathbf{K}}_{t+\Delta t}^{u\phi}$, $\bar{\mathbf{K}}_{t+\Delta t}^{\phi u}$, $\bar{\mathbf{K}}_{t+\Delta t}^{\phi\phi}$

Structural analyses are performed in order to simulate the overall performance of several active structures subjected to various histories of thermo-electro-mechanical behaviors. Analytical and numerical methods have been used.

a) Shape changes in active beams due to electric field inputs

Deformations in a fiber reinforced laminated composite plate bonded with four piezoelectric patches due to electric field inputs are analyzed. The composite plate is first assumed linear elastic with the following elastic material properties: $E=36000$ MPa, $\nu=0.25$ in the longitudinal fiber axis. The plate is clamped along one of its 50 mm side surface and the PZT patches are bonded perfectly to the host structure. The potential on the surfaces of the PZT patches that are in contact to the host structure is grounded to zero. The PZT patches are uniformly subjected to a potential gradient through their thickness $E_3(t) = 1.2 \sin(2\pi ft)$ MV/m so that they experience expansion in their planar direction, thus inducing bending to the composite plate. Figure 57 depicts the lateral displacement measured at the mid-section of the free end due to the input electric field applied uniformly to the four PZT patches, which show vibration of the composite

plate. It is seen that the highest deformation occurs at the first quarter cycle, when the electric field reaches 1.2 MV/m (point A). Upon removal of the electric field, the remanent deformation is shown (point B) and when the electric field reaches the coercive limit of the PZT patches no deformation is shown in the plate (point C) due to depolarization of the PZT patches. Continuing applying the electric field till it reaches the lowest peak -1.2 MV/m (point D) trigger bending in the composite plate. It is also seen that due to the time-dependent effect, the highest displacement is at the first quarter cycle and after several cycles, saturation in the butterfly displacement loop is achieved. The corresponding deformed shapes of the composite plate at several instant of times during the first cycle are illustrated in Fig. 58. It is also possible to create different deformed shapes by considering various histories of electric field inputs. For example, to induce twisting of the plate different electric field inputs can be applied to the four patches. The tip-deflection, illustrated in Fig. 59, is generated by prescribing the following electric field input $E_3(t) = 1.2 \sin(2\pi ft)$ MV/m to the two PZT, and $E_3(t) = 1.2 \sin(2\pi ft - \pi/2)$ MV/m to the other two patches.

The effect of time dependent response of a viscoelastic host structures with piezoelectric patches on the overall mechanical deflection is also examined. Figure 60 illustrate the lateral deflection in smart beams activated by applying electric field to the patches. The patches are activated with the same time function with the frequency of 0.1Hz. Elastic and viscoelastic host structures are considered. It is seen that responses of the lateral deflections of the elastic and viscoelastic host structure are quite different. A delayed response of the viscoelastic host structure due to the electric field inputs is observed. It is noted that small loops are seen in the response at the highest amplitude of electric field, which could be due to a superimposed of two different hysteresis behaviors from the mechanical response of host structure and cyclic electric field of the patches. The small loops near the peaks of the hysteresis responses are experimentally observed in piezoelectric micro fiber composite (MFC) actuators (Usher et al., 2013) and are also observed as distortion of hysteresis loop while resistor is added to the actuation circuit of BaTiO₃ (Jaffe 2012).

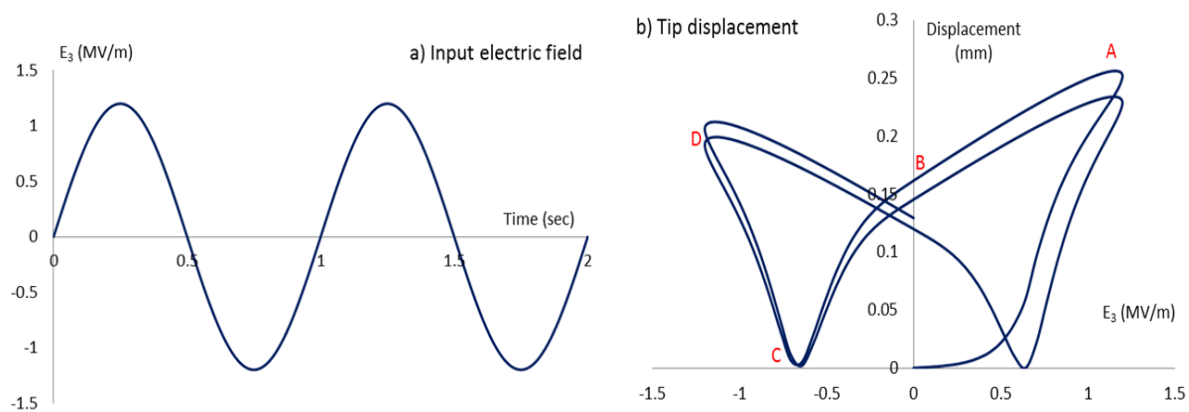


Figure 57 Shape changing performance in a glass/fiber laminated composite plate subjected to a hysteretic electric field input. The deformation is controlled through the use of piezoelectric ceramics patches.

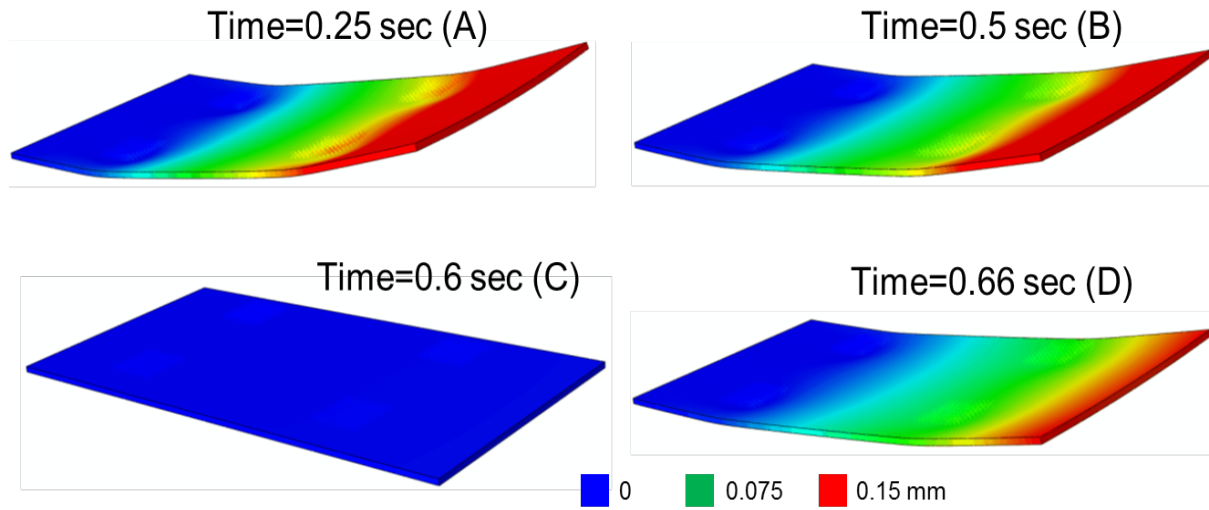


Figure 58 Deformed shapes of smart beams due to electric field inputs applied to the piezoelectric patches.

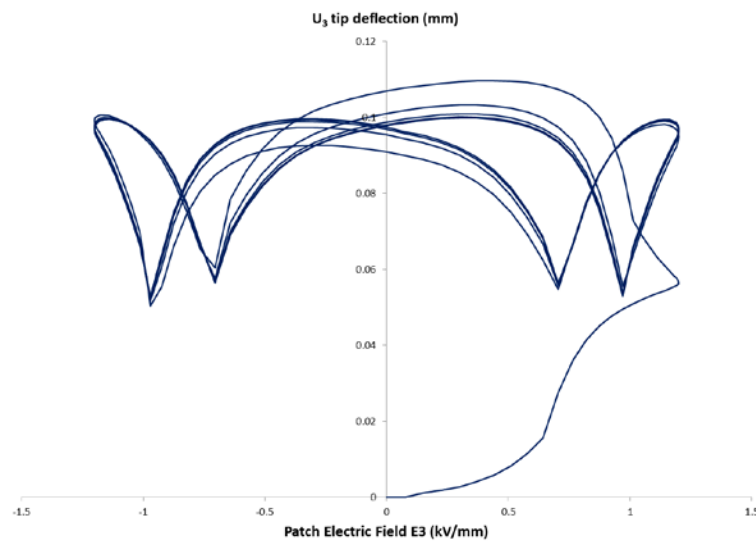


Figure 59 Tip deflection of the cantilever plate due to a non-uniform cyclic electric field applied to the piezoelectric patches

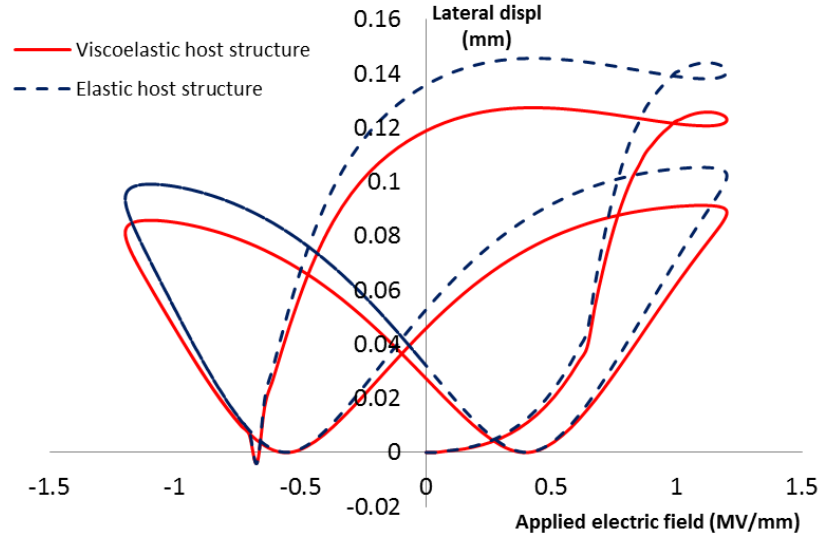


Figure 60 Lateral deflections in smart composites with elastic and viscoelastic host structures

A nonlinear electro-mechanical response of bimorph beam subjected to cyclic electric field input with frequency of 1Hz is also considered, following an experimental test reported by Li and Fang (2004). The beam consists of three layers with piezoelectric layers attached to the top and bottom surfaces. The nonlinear electro-mechanical coupling, discussed in **Section 4.2.**, is adopted, which give the following electro-mechanical relation $\sigma_{11} = e_{311}E_3 + h_{33311}E_3E_3E_3$, and the time-dependent kernel function is taken as $K(t) = K_0 + K_1 \exp^{-\lambda_1 t}$. The beam is under simply supported. Analytical solution, using the Laplace transform method, is considered in predicting the bending deformation of the beam due to the electric field input. Figure 61 illustrates the electro-mechanical response of the beam obtained from analytical and experimental results. Good correlations between the model and experiment are observed.

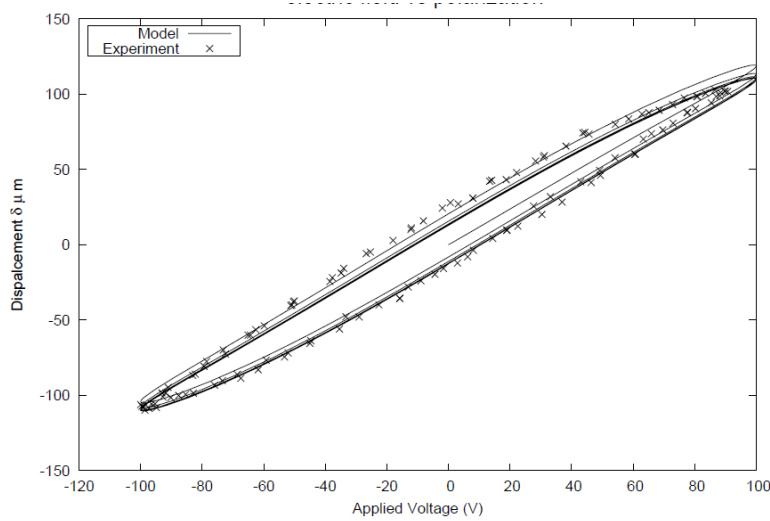
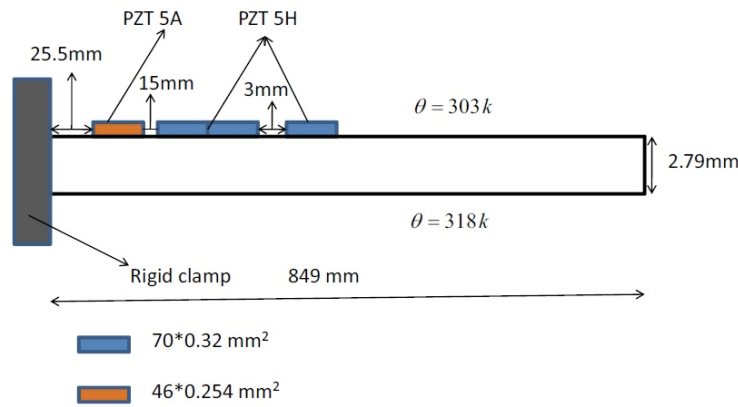
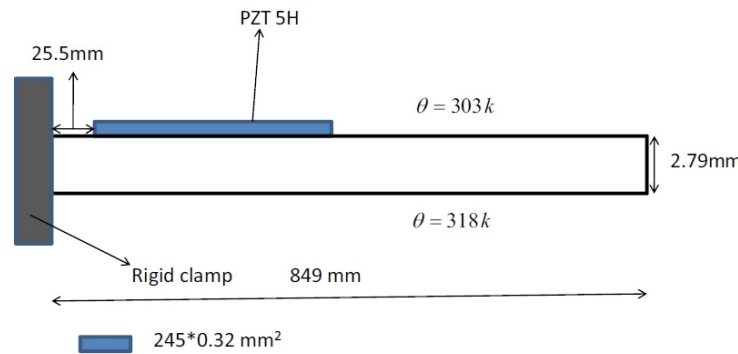


Figure 61 Analytical and experimental results of bending deformation in active beam due to electric field.

Piezoelectric materials can also be used for sensing and actuating, such as detecting and suppressing the deformation in a beam. Song et al. (2004) conducted a test on a smart beam with PZT sensor and actuator (Fig. 62a), in which the PZT is used to sense an excessive deformation in the beam due to a temperature change and the PZT actuator is used to minimize the lateral deformation. In this study, the suppression of the lateral deformation in the beam using PZT actuator is simulated. For this purpose, the placement of the PZT patches is slightly modified (Fig. 62b). The steady state temperature field is assumed in the composite beam. Figure 63 compares the numerically evaluated vertical displacement of the beam due to temperature gradient, for both the actuated and the unactuated states. The tip displacement of the unactuated beam, predicted numerically, is 11.46 mm compared to 11 mm as reported in Song et al. (2004). Hence, there is good agreement between both the theoretical predictions and experimental results. The numerically calculated actuating voltage is 45V as compared to 150V experimentally. The difference in the magnitudes of both the voltages could be attributed to the modified geometry, since the length of actuator in the modified geometry is greater than that of the original.



(a) Composite beam with 3 PZT 5H actuators and one PZT 5A sensor



(b) Composite beam with PZT 5H surface bonded actuator

Figure 62 A smart composite beam with PZT patches: (a) the geometry used by Song et al. ; (b) the modified geometry used in the current numerical study

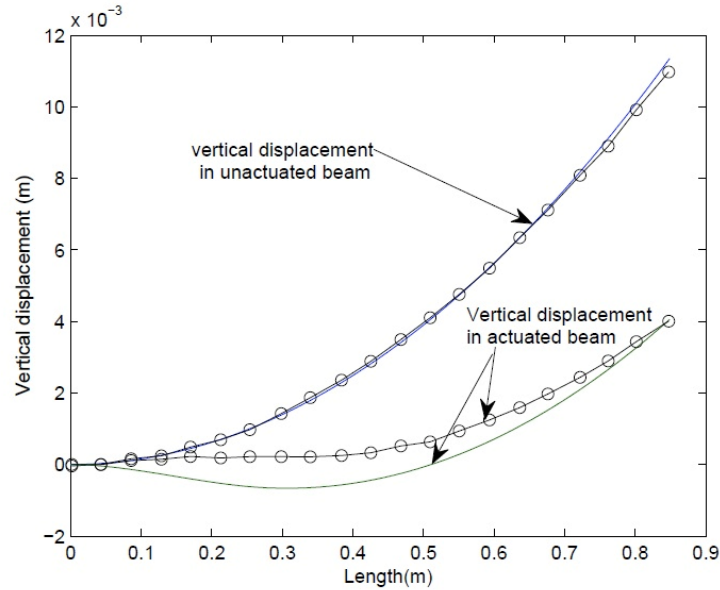


Figure 63 Comparison of the vertical displacement obtained numerically to that reported in Song et al. (2004) for the beam in actuated and unactuated states. Curves highlighted by ('o') depict the experimental results

Next, the integrated micromechanical and FE analyses are used to study the deformation in smart sandwich composites having polyurethane foam core and piezoelectric sensors embedded in the laminated facesheets (Fig. 64). The simplified micromechanical model for fiber composites discussed in **Section 4.3** is implemented in continuum finite element and used to obtain the overall response of facesheets (see Kim et al. 2011 for detailed discussion). Viscoelastic constitutive models are considered for the polyurethane foam and epoxy matrix in the facesheet. Linear electro-mechanical response is assumed for the piezoelectric wafers. It is noted than in this example, the piezoelectric wafers are used to monitor deformation in the thick-section sandwich beam. Relatively small magnitude of electrical and mechanical inputs are experienced by the piezoelectric wafers since the thick-section of sandwich beam undergoes relatively small deformations. The piezoelectric wafers can be used to monitor time-dependent performances in the sandwich composites. The smart sandwich beam is first subjected to a temperature change from room temperature to 80°C, once the beam is under isothermal temperature at 80°C, a mechanical load is prescribed in order to simulate three point bending deformation. Figure 64 (top right) shows the creep responses of the sandwich composites obtained from the multi-scale model and experiments. Good correlations are observed. The corresponding lateral displacement and axial stress fields are shown in Fig. 64 (bottom left). Finally, the recorded electric potentials in the piezoelectric wafers during creep deformation are also reported.

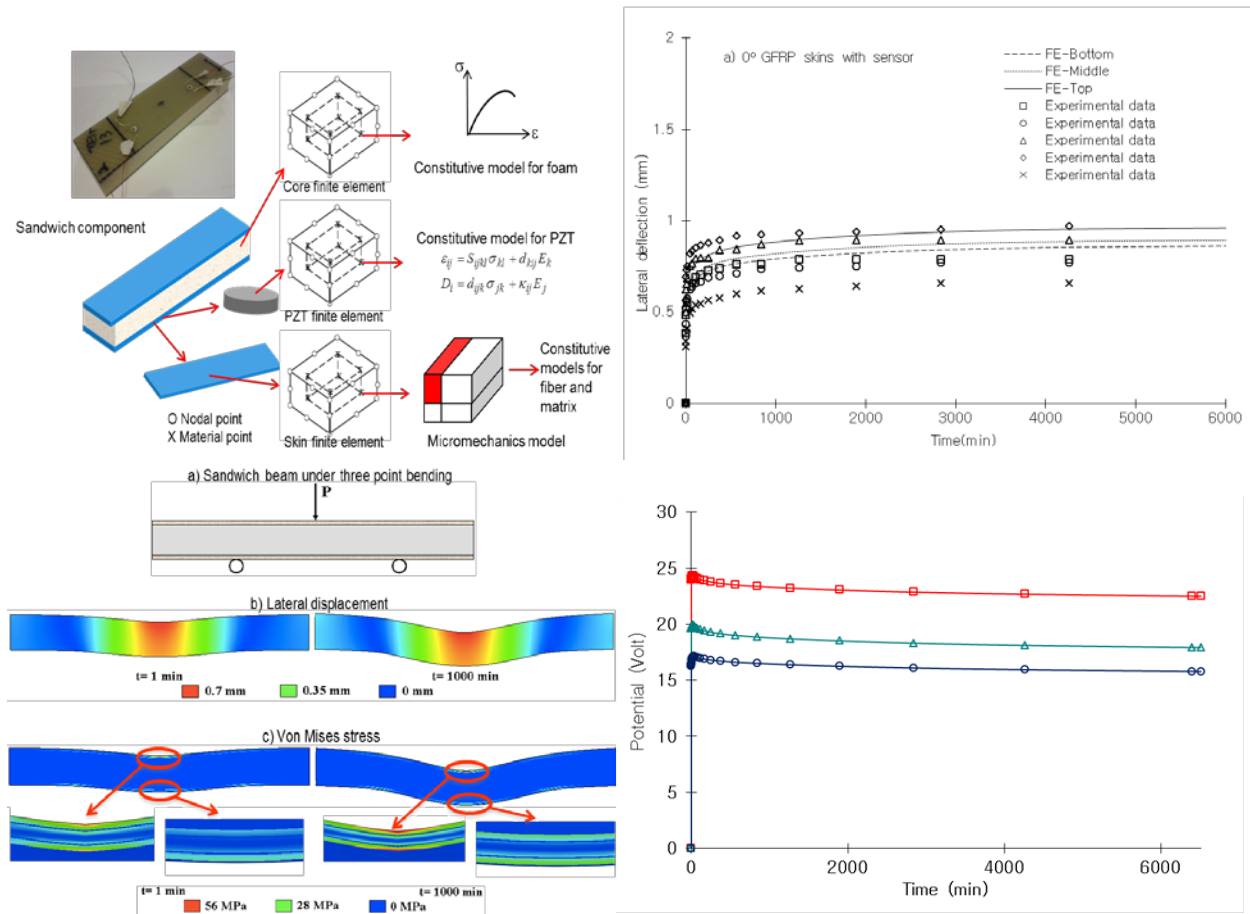


Figure 64 A multi-scale model for predicting time-temperature dependent response of smart sandwich composites: a multi-scale framework (top left); overall creep response in smart sandwich beam at 80°C (top right); overall displacement and stress fields at two different times (bottom left); and electric potential reading from the piezoelectric sensor during the creep deformation (bottom right).

b) Active fiber composite

The nonlinear time-dependent electro-mechanical and viscoelastic constitutive models, which are implemented in FE, are also used to study the overall electro-mechanical responses of AFCs, comprising of PZT fibers, epoxy matrix, and electrode fingers, as illustrated in Fig. 1. The AFC specimens are subjected to cyclic electric fields with different amplitude and frequencies, and the overall electro-mechanical responses are monitored. A representative unit-cell model of AFCs is considered, as shown in Fig. 65, and 3D continuum elements are used to generate the unit-cell model of AFCs. Electric field lines are obtained through the positive and negative electric potentials applied to the electrodes, as illustrated in Fig. 65. The nonlinear time-dependent electro-mechanical constitutive model (**Section 4.2**) is considered for the PZT, while a viscoelastic model is used for the epoxy. The mechanical responses of the electrode fingers are modeled as linear elastic, while a linear electro-static model is considered for the electrical behavior of the electrode fingers. Figure 66 illustrates the hysteretic responses of the AFCs from experiments and FE analyses.

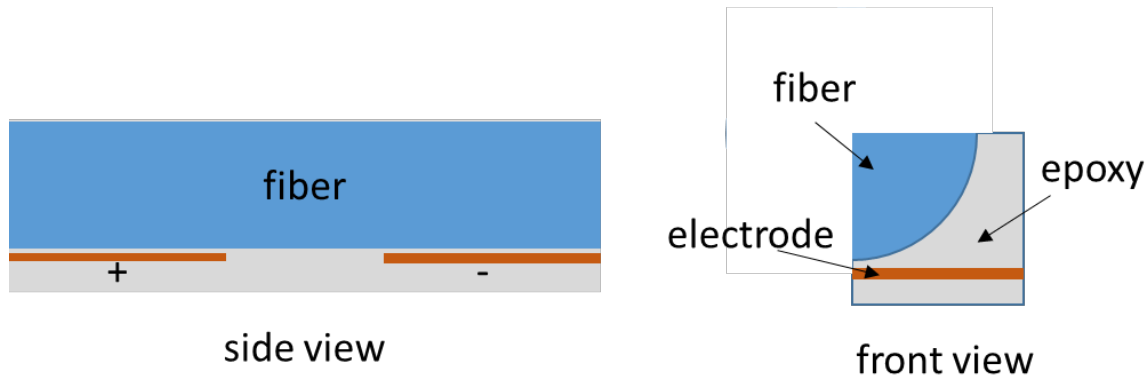


Figure 65 AFC unit-cell

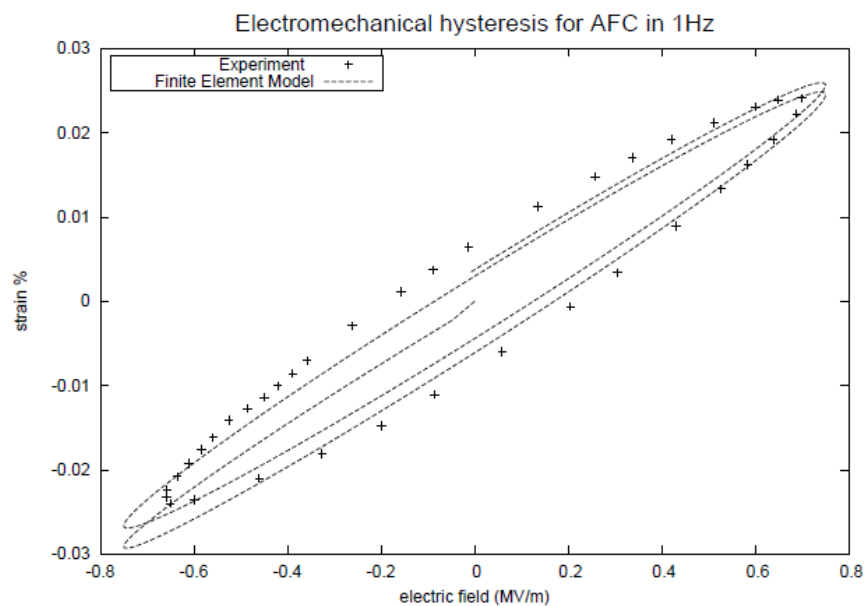


Figure 66 Electro-mechanical hysteretic responses

c) Active truss systems

The finite element analyses for electro-active materials and structures are also presented to study shape changes in smart structures comprising of 3D active truss systems. Trusses are known as load bearing components in many structures. Truss systems consist of relatively slender members connected by flexible joints with rotational and translational motions, making them appealing for compliant structures. Recent advances in active materials, such as shape memory and electro-active materials, allow for generating compliant structures that can sense and adapt to various stimuli by controllable configurations into various shapes. There have been several studies on understanding the geometry of the truss systems for certain applications. Sofla et al. (2009) studied morphing hinged truss structures, where they have used shape memory wires in order to activate their structure. Macareno et al. (2008) considered a linear truss made of 3D tetrahedral units for Variable Geometry Trusses (VGTs). Avilés et al. (2000) investigated the position problems in the open-loop variable geometry trusses. An optimization scheme is

designed in order to minimize the actuator's displacement and consequently its energy. This method has been used for different truss architectures in specific to modular tetrahedral linear truss. Reconfiguration of the shape of structures can change the way and even intensity of the load that the structures can withhold. Shape changing capability can improve the performance of the structures and is expected to enhance durability of the structures by continuously minimizing stresses in the structures.

This study focuses on theoretical and computational methods on controlling shape changes in compliant truss systems comprising of electro-active (piezoelectric) materials. An elastic response is considered for the mechanical behavior of the truss, while a nonlinear electro-mechanical coupling is used for the piezoelectric components. A desired shape is determined through the deformation paths, and the corresponding strains and stresses are calculated. The stresses are then prescribed by applying electric field through the piezoelectric materials, and as a result the truss system undergoes the desired shape changes. The procedure is summarized as:

- 1) Define equations that form shape changes from reference configuration (X_i) to deformed configuration (x_i)

- 2) The deformation gradient and strain are defined as: $\mathbf{F} = \frac{\partial \mathbf{x}}{\partial \mathbf{X}}$ and $\boldsymbol{\varepsilon} = \frac{1}{2}(\mathbf{F}^T \mathbf{F} - \mathbf{I})$

- 3) Unit vector direction for each truss element is determined from the current location

- 4) Determine the amount and direction of electric field that should be prescribed to the individual active member from the unit-vector and constitutive relation $G(\boldsymbol{\varepsilon}, \mathbf{E}) = 0$

The first example that has been considered in this study is a linear tetrahedral truss. The desired shape of the truss is considered to be a curve that is clamped at the origin and it passes the points $(L/4, L/8)$, $(3L/4, -L/8)$, $(L, L/8)$ with L being the total length of the linear truss. This shape is shown in Fig 67 (top). This truss consists of 70 tetrahedral units, 72 nodes and 213 truss members. The beam theory approximation for the stresses induced in the beam is used to actuate shape changing in the truss, as shown in Fig. 67. Another example is done on generating a sinusoidal shape change by electrically activated piezoelectric components in the truss system, as illustrated in Fig. 68. It is seen that a relatively large displacement can be attained while maintaining a relatively small strain in each truss component. The amount of voltage needed is based on the electro-mechanical properties of a piezoelectric tube actuator.

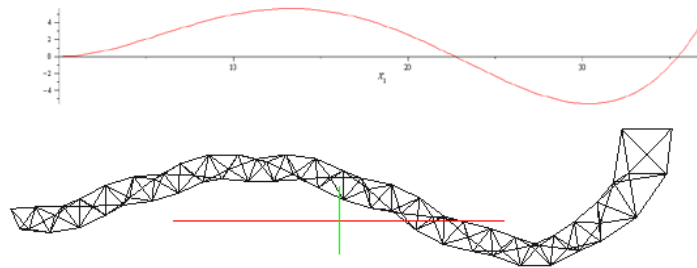


Figure 67 Beam like truss: Reference configuration (top) and deformed configuration (bottom)

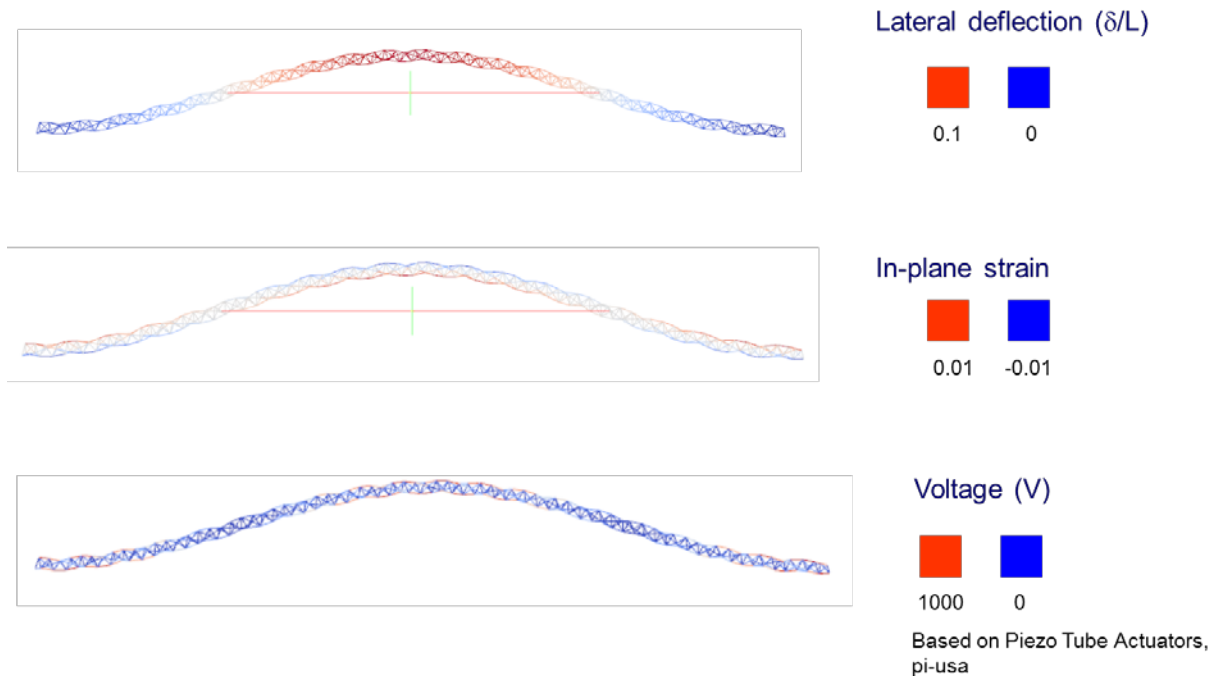


Figure 68 Sinusoidal shape changes produced by actuating a tetrahedral truss system

d) Pinching of a slender honeycomb structure

Another example of inducing lateral deflections (shape changes) in a slender structure is by deforming a mid-section of a slender plate or beam comprising of honeycomb-like structures, as illustrated in Fig. 69. FE analyses of smart structures are used to study the lateral deflection of the plate. Consider a plate with actuators placed in its mid-section, which can be activated in the transverse direction of the plate. The honeycomb-like microstructures of the plate results in lightweight and compliant systems. By deforming the mid-section of the plate, in this case through the piezoelectric actuators, the plate experiences flapping (bending). The amount of lateral deflection at the free end that can be gained by laterally deforming the mid-section is shown in Fig. 70. It is seen that a relatively small deformation induced on the mid-section can generate a relatively large lateral displacement. Different microstructural designs of the active slender plate can also be considered in order to achieve bending/flapping of the plate. One of the advantages of this plate design is that it is relatively easy to control the deformation through electric field inputs prescribed at one location, instead of applying different electric field inputs at various locations in order to achieve desired shapes, like in the active truss systems or composite beams with piezoelectric patches.

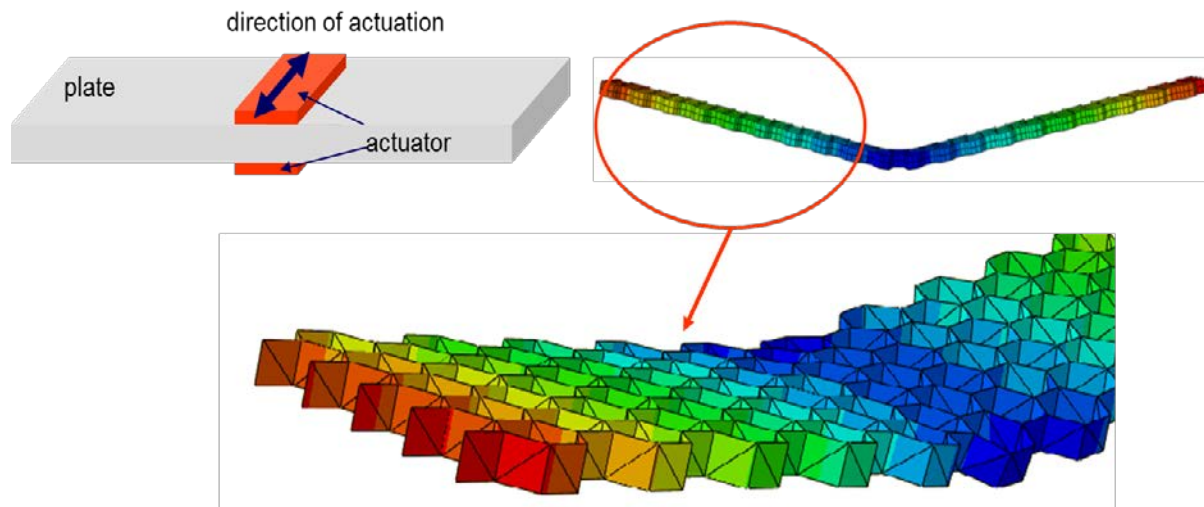


Figure 69 A slender honeycomb structure undergoing bending due to pinching

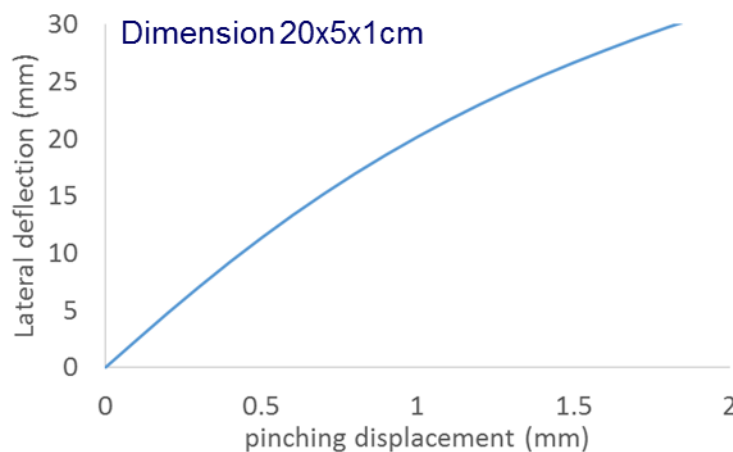


Figure 70 Lateral deflection obtained from pinching the mid-point of the beam

4.5) Concluding Remarks

Smart composites comprising of piezoelectric materials as the electro-active component are promising for multifunctional systems such as morphing structures. Lightweight and flexible active structures are necessary for generating morphing systems with the ability to respond to various external stimuli. Various types of electro-active lightweight and flexible composites have been considered, such as piezocomposites comprising of piezoelectric ceramics inclusions and ductile matrix (polymers and metals), laminated composites with integrated piezoelectric materials, arrangements of flexible systems with active components, etc. Several experimental evidences show that piezoelectric ceramics can experience nonlinear and time-dependent responses when subjected to electro-mechanical responses. High electric field inputs and compressive stresses can lead to polarization switching, disrupting the electro-mechanical coupling performance of the multifunctional systems. Furthermore, polymers are promising for

generating flexible and lightweight systems; however, they experience significant viscoelastic responses. Both piezoelectric ceramics and polymers dissipate energy when subjected to mechanical and non-mechanical stimuli, which is converted into heat and thus increasing the temperatures of the systems. It is also known that the electro-mechanical performances of piezoelectric ceramics and polymers change with temperatures. The differences in the nonlinear time-dependent thermo-electro-mechanical responses of piezoelectric ceramics and polymers, together with various microstructural morphologies will have significant effects on the overall performance of multifunctional morphing systems.

This project is aimed at understanding the effect of coupled thermal, electrical, and mechanical responses, including loading rate (time) effect, of the constituents (piezoelectric ceramics and polymers) on the overall multi-field responses of electro-active composites. For this purpose, a multi-scale framework that consists of constitutive models for constituents incorporating coupled deformation, heat conduction, and piezoelectric analyses with stress, temperature, electric field, and time dependent responses; nonlinear micromechanical models for various composite reinforcements including functionally graded composites; and large scale multifunctional structural analyses has been formulated. Limited experiments on piezocomposites have been conducted in order to study micro-scale response of the composite and provide useful insight into the effect of microstructural morphologies on the overall (macroscopic) multi-field response of composites.

Phenomenological models within continuum mechanics and thermodynamics approaches have been formulated for ferroelectric ceramics undergoing various levels of electric field inputs and mechanical stresses, and for polymers under various histories of mechanical loadings. For the ferroelectric ceramics, the responses from the constitutive models have been successfully compared with available experimental data, incorporating time (rate), temperature, and electric field dependent behaviors. Fully coupled thermo-viscoelastic models have been formulated, and shown capable in capturing the overall heat conduction and deformation in polymers and polymeric composites. Furthermore, efficient numerical integration algorithms have been developed in order to simulate the overall performance of ferroelectric ceramics and polymers under various histories of external stimuli. The numerical integration algorithms are easily implemented within finite element and finite difference numerical methods, and integrated to various micromechanics models.

Several micromechanics models, i.e., simplified unit-cell methods and micromechanics models with microstructural details, have been considered in order to determine the overall nonlinear time-dependent behaviors of composites undergoing couple heat conduction and electro-mechanical deformations. The micromechanical models incorporate different nonlinear time- and field dependent constitutive models for the inclusions and matrix. Efficient numerical algorithms have been formulated for different micromechanical models, and implemented in finite element analyses. The effective (macroscopic) responses determined from the unit-cell models have been compared with the overall responses from available experimental data and micromechanics models with microstructural details. The unit-cell models are shown capable in capturing the macroscopic responses of the composites under various histories of loadings, even though relatively crude approximations are considered in formulating the unit-cell models. The micromechanics studies also reveal the importance of thermal stress effects, which occurs due to

temperature changes during either processing of the composites or in-service conditions, on the overall electro-mechanical responses of composites. It is noted that relatively high thermal stresses in the constituents of the composites often lead to significant nonlinear responses, including possibilities of damage/degradation, and accelerate the time-dependent deformations, and thus affecting the overall responses of the composites. The unit-cell models, however, are limited in capturing the discontinuities of field variables at the interfaces between the inclusions and matrix, and localized field variables, such as stress concentrations. Discontinuities and localized field variables often cause debonding and damage of the composites. One of the major advantages in using the simplified unit-cell models over the micromechanical models with microstructural details is in cutting the computational cost, while reasonably predicting the overall nonlinear and time-dependent responses of the composites. Thus, the unit-cell models are promising for analyzing large-scale structures under various histories of mechanical and non-mechanical stimuli, and at the same time incorporating the nonlinear and time-dependent responses of the constituents.

A multi-scale framework has been formulated by integrating nonlinear time-dependent constitutive models, micromechanics models, and structural analyses via finite element and finite difference methods. The multi-scale framework is used to study the overall performance of active structures or structural components undergoing various histories of external stimuli, and perform active controls using the active materials, i.e., piezoelectric ceramics and piezoelectric composites, in order to achieve desired performance of the structures. Several examples have been presented on the ability of the multi-scale framework in simulating time-dependent multi-field responses of active structures or structural components. It is noted that for precisely controlling the deformed shapes of structural components using electro-active composites, it is necessary to take into account the different time-dependent behaviors of the constituents and microstructural morphologies in the active composites since they significantly affect the overall performance of the smart structures.

4.6) References:

1. Aboudi, J. (2005), Micromechanically Established Constitutive Equations for Multiphase Materials with Viscoelastic-Viscoplastic Phases, *Mech. of Time-dependent Mat.*, 9, pp. 121-145
2. Alexander P, Brei D, Miao W, Halloran J, Gentilman R, Schmidt G, McGuire P, Hollenbeck J (2001), Fabrication and experimental characterization of d31 telescopic piezoelectric actuators, *Journal of materials science* 36 (17), pp. 4231-4237
3. Alexander P and Brei D (2003), "Piezoceramic Telescopic Actuator Quasi-static Experimental Characterization," *J. Intelligent Material Systems and Structures*, 14, pp. 643-655
4. Alexander, P. W., and Brei, D (2005), "The Fabrication and Material Characterization of PZT Based Functionally Graded Piezoceramics," *Proceedings of SPIE-The International Society for Optical Engineering*, 5764:57-70

5. Aviles R, Ajuria G, Amezuza E, and Gomez-Garay V (2000), "A finite element approach to the position problems in openloop variable geometry trusses," *Finite Elements in Analysis and Design*, vol. 34, no. 34, pp. 233 – 255
6. Ben-Atitallah H, Ounaies Z and Muliana AH (2014), "On the Temperature and Time-dependence of the Electro-mechanical Properties of Flexible Active Fiber Composites," in review
7. Bent, A.A. (1994), "Piezoelectric fiber composites for structural actuation," PhD Dissertation, Dept. of Aeronautics and Astronautics. Massachusetts Institute of Technology
8. Chan, H. L. W., and J. Unsworth. (1989), "Simple Model for Piezoelectric Ceramic/Polymer 1-3 Composites Used in Ultrasonic Transducer Applications," *IEEE. Tran. Ultrason., Ferroelectr. Freq. Control*, 36(4), pp. 434-441
9. Crawley, E.F. and Anderson, E.H. (1990), "Detailed Models of Piezoceramic Actuation of Beams" *J. Intell. Mater. Syst. Struct.*, 1, pp. 4-25
10. Fang, D. and Li, C (1999), "Nonlinear Electric-Mechanical Behavior of a Soft PZT-51 Ferroelectric Ceramic," *J. Materials Sci.*, 34, pp. 4001-4010
11. Furukawa, T., Fujino K, and Fukada, E (1976), "Electromechanical Properties in the Composites of Epoxy Resin and PZT Ceramics," *Jap. J. Appl. Phys.*, 15(11), pp. 2119-2129
12. Hagood, N.W., Kindel R., Ghandi K., and Gaudenzi P (1993), "Improving transverse actuation of piezoceramics using interdigitated surface electrodes," *Proceeding SPIE* 1917, 12 pages
13. Hooker, M.W. (1998), "Properties of PZT-based Piezoelectric Ceramics between -150 and 250°C," *NASA Contract Report, NASA/CR-1998-208708*
14. Gudlur P (2013), "Experimental and Numerical Studies of Aluminum-Alumina Composites," *Texas A&M University, PhD Dissertation*
15. Gudlur, P., Muliana, A., and Radovic, M (2014), "Thermo-mechanical Properties of Aluminum-Alumina Composites based on its Microstructural Characteristics," *Composite Part B*, 58C, pp. 534-543
16. Jaffe, B (2012) *Piezoelectric ceramics*, volume 3. Elsevier
17. Jeon J. and Muliana, A. (2012), "A Simplified Micromechanical Model for Analyzing Viscoelastic-Viscoplastic Response of Unidirectional Fiber Composites" *ASME J Engineering Materials and Technology*, 134, 031003
18. Jin D and Meng Z (2003), "Functionally Graded PZT/ZnO Piezoelectric Composites," *J. Materials Science Letters*, 22, pp. 971-974
19. Karadeniz, Z.H., and Kumlutas, D. (2007), "A Numerical Study on The Coefficients of Thermal Expansion of Fiber Reinforced Composite Materials," *Composite Structures*, Vol. 78, pp. 1-10
20. Khan, KA and Muliana, A (2012a), "Fully Coupled Heat Conduction and Deformation Analyses in Viscoelastic Structures" *Mechanics Time-dependent Materials*, 16(4), pp. 461-489
21. Khan, K and Muliana, A. (2012b), "Fully Coupled Heat Conduction and Deformation Analyses of Viscoelastic Composites" *Composite Structures*, 94(6), pp. 2025-2037
22. Kim, J.S. and Muliana, A. (2010), "A Combined Viscoelastic-Viscoplastic Behavior of Particle Reinforced Composites," *Int. J. Solids and Structures*, 47, pp. 580-594
23. Kim JS, Arronche L, Farrugia A, Muliana A, La Saponara, V (2011), "Multi-scale Modeling of Time-dependent Response of Smart Sandwich Constructions" *Composite Structures*, 93, pp. 2196-2207

24. Li F and Fang D (2004), "Simulations of domain switching in ferroelectrics by a three-dimensional finite element model" *Mechanics of Materials*, 36, pp. 959-973
25. Lin, CH and Muliana, AH (2013), "Micromechanics Models for the Effective Nonlinear Electro-mechanical Responses of Piezoelectric Composites" *Acta Mechanica*, 224, pp. 1471–1492
26. Lin CH and Muliana A (2014a), "Polarization Switching Responses of 1-3 and 0-3 Active Composites" *Composite Structures*, 116, pp. 535-551
27. Lin CH and Muliana AH (2014b), "Nonlinear Electro-mechanical Responses of Functionally Graded Piezoelectric Beams," *Composites Part B*, in press
28. Lines, M.E. and Glass, A. E. (2009) *Principles and Applications of Ferroelectrics and Related Materials*, Oxford University Press, New York
29. Macareno LM, Agirrebeitia J, Angulo C, and Avils R (2008), "fFEMg subsystem replacement techniques for strength problems in variable geometry trusses," *Finite Elements in Analysis and Design*, vol. 44, no. 67, pp. 346 – 357
30. McIvor, S.D., Darby, M.I., Wostenholm, G.H., and Yates, B. (1990), "Thermal Conductivity Measurements of some Glass and Carbon Fiber Reinforced Plastics," *J. Materials Science*, 25, pp. 3127-3123
31. Megnis, M. and Varna, J. (2003), "Micromechanics based modeling of nonlinear viscoplastic response of unidirectional composite," *Composites Science and Technology* 63, pp.19–31
32. Muliana, A.H., Khan, K.A. (2008), "A time-integration algorithm for thermorheologically complex polymers," *Computational Materials Science* **41**(4), 576-588
33. Muliana, A. and Kim, J.S. (2010), "A Two-scale Homogenization Framework for the Effective Thermal Conductivity of Laminated Composites" *Acta Mechanica*, 212(3-4), pp. 319-347
34. Muliana, A and Lin CH (2011), "A Multi-scale Formulation for Predicting Nonlinear Thermo-electro-mechanical Response in Heterogeneous Bodies," *J. Intelligent Material Systems and Structures*, 22, pp. 723-738
35. Perzyna, P. (1971), "Thermodynamic of rheological materials with internal changes," *J. Mech*, Vol. 10, pp. 391–408
36. Schapery, R.A. (1969), "Further development of a thermodynamic constitutive theory: stress formulation," *Purdue University Report No. AA & ES. 692*
37. Sofla A, Elzey D, and Wadley H (2009), "Shape morphing hinged truss structures," *Smart Materials and Structures*, vol. 18, no. 6, p. 065012
38. Sohrabi, A. and Muliana, AH (2013), "Rate-dependent and Electro-mechanical Coupling Response of Ferroelectric Materials: A Finite Element Formulation" *Mechanics of Materials (MOM)*, 62, pp. 44-59
39. Sohrabi A and Muliana AH (2014), "Nonlinear and Time-dependent Behaviors of Piezoelectric Materials and Structures," in review
40. Song G, Zhou X, and Binienda W (2004), "Thermal deformation compensation of a composite beam using piezoelectric actuators," *Smart Mater. Struct.*, vol. 13, pp. 30-37
41. Takagi, K., J.-F. Li, S. Yokoyama, R. Watanabe, A. Almajid, and Minoru Taya. (2002), "Design and Fabrication of Functionally Graded PZT/Pt Piezoelectric Bimorph Actuator," *Sci. Technol. Adv. Mater.*, 3(2), pp. 217-224
42. Timothy D Usher, Kenneth R Ulibarri, and Gilberto S Camargo (2013), "Piezoelectric microfiber composite actuators for morphing wings," *ISRN Materials Science*

43. Valanis, K.C., (1971), "A theory of viscoplasticity without a yield surface, Part 1. General theory," *Arch. Mech.* 23, pp. 517–533
44. Wu, C. C. M., Kahn M, and Moy W (1996), "Piezoelectric Ceramics with Functional Gradients: A New Application in Material Design," *J. Am. Ceram. Soc.*, 79(3), pp. 809-812
45. Xing J, Jang A, Radovic M, and Muliana A (2013), "Thermal properties of BaTiO₃/Ag Composites undergoing Phase Transformation due to Temperature Changes" American Society for Composites, 28th Technical Conference (ASC), September 9-11
46. Zhou, D. and Kamlah, M. (2006), "Room-temperature Creep of Soft PZT under Static Electrical and Compressive Stress Loading," *Acta Materialia*, 54, pp. 1389-1396

5) Listing of Publication and Report

Book chapter and book:

1. Muliana, A., "A Multi-scale Formulation for Smart Composites with Field Coupling Effects" part of Advances in Mathematical Modeling and Experimental Methods for Materials and Structures. The Jacob Aboudi Volume, Vol. 168, pp. 73-87, 2010
2. Sohrabi, A and Muliana, AH, "Nonlinear Hysteretic Response of Piezoelectric Ceramics" part of Ferroelectrics: Characterization and Modeling, Ed. Mickael Lallart, Intech 2011
3. Li, K.A. and Muliana, A.H., "Time-dependent Behavior of Active Polymer Matrix Composites", part of Creep and Fatigue in Composites, Ed. RM Guedes, pp. 70-112, Woodhead Publishing 2011
4. Doshi, S., Sohrabi, A, Muliana, AH, and Reddy, JN "Analyses of Multifunctional Layered Composite Beams" part of Mechanics and Design of Smart Composites, Ed. Elhajjar et al., CRC Press, Boca Raton, Florida 2013
5. El-Hajjar, R, Law, C, and Muliana, AH, "Behavior and Characterization of Magnetostrictive Composites," part of Mechanics and Design of Smart Composites, Ed. Elhajjar et al., CRC Press, Boca Raton, Florida 2013
6. Elhajjar R, La Saponara V, and Muliana AH, Smart Composites: Mechanics and Design, CRC Press, Boca Raton, Florida 2013

Master theses and PhD dissertations

1. Li, K.A., "Modeling Time-dependent Responses of Piezoelectric Fiber Composites", Department of Mechanical Engineering, Texas A&M University, Master Thesis 2009.
2. Zeaid Hasan, "Controlling Performance of Laminated Composites using Piezoelectric Materials", Texas A&M University, Master Thesis 2010
3. Ramachandran Kuravi, "Analyzing Coupled Heat Conduction, Moisture Diffusion, and Deformation in Smart Structures", Texas A&M University, Master Thesis 2010
4. Kamran Khan, "A Multi-scale Model for Coupled Heat Conduction and Deformations of Viscoelastic Composites," Texas A&M University, PhD Dissertation 2011
5. Sukanya Doshi, "Study of Thermo-electro-mechanical Coupling in Functionally Graded Metal-Ceramic Composites," Texas A&M University, Master Thesis 2012
6. Pradeep Gudlur, "Experimental and Numerical Studies of Aluminum-Alumina Composites," Texas A&M University, PhD Dissertation 2013
7. Jaehyeuk Jeon, "A Viscoelastic-viscoplastic Analysis of Fiber Reinforced Polymer Composites undergoing Mechanical Loading and Temperature Changes," Texas A&M University, PhD Dissertation 2013
8. Chien Hong Lin, "Micromechanics modeling of nonlinear and time-dependent responses of piezoelectric 1-3, 0-3, and hybrid Composites," Texas A&M University, PhD Dissertation 2014

9. Amir Sohrabi, "Nonlinear and rate-dependent hysteretic electro-mechanical responses of ferroelectric materials," Texas A&M University, PhD Dissertation expected May 2015

Journal paper published and accepted:

1. Khan, K. A. and Muliana, A., "A Multi-scale Model for Coupled Heat Conduction and Deformations in Functionally Graded Materials," Special Issue on Blast resistance of Nano-engineered Composites" Composite part B, 40, pp. 511-521, 2009
2. Muliana, A. and Kim, J.S., "A Two-scale Homogenization Framework for the Effective Thermal Conductivity of Laminated Composites" Acta Mechanica, 212(3-4), pp. 319-347, 2010
3. Kim, J.S. and Muliana, A., "A Combined Viscoelastic-Viscoplastic Behavior of Particle Reinforced Composites," Int. J. Solids and Structures, 47, pp. 580-594, 2010
4. Muliana, A.H., "A Micromechanical Formulation for Piezoelectric Fiber Composites with Nonlinear and Viscoelastic Constituents" Acta Materialia, 58, pp. 3332-3344, 2010
5. Muliana, AH and Li, K.A., "Time-dependent Response of Active Composites with Thermal, Electrical, and Mechanical Coupling Effect" Int. J. Engineering Science, 48, pp. 1481-1497, 2010
6. Muliana, A and Lin CH, "A Multi-scale Formulation for Predicting Nonlinear Thermo-electro-mechanical Response in Heterogeneous Bodies," J. Intelligent Material Systems and Structures, 22, pp. 723-738, 2011
7. Muliana, A., "Time-temperature Dependent Behavior of Ferroelectric Materials undergoing Cyclic Electric Field" Int. J. Solids and Structures, 48 (19), pp. 2718-2731, 2011
8. Khan, KA, Barello, R., Muliana, AH., and Levesque, M., "Coupled Heat Conduction and Thermal Stress Analyses in Particulate Composites," Mechanics of Materials, 43, pp. 608-625 2011
9. Kim JS, Arronche L, Farrugia A, Muliana A, La Saponara, V, "Multi-scale Modeling of Time-dependent Response of Smart Sandwich Constructions" Composite Structures, 93, pp. 2196-2207, 2011
10. Farrugia, A., Winkelman, C., La Saponara, V., Kim, J.S. and Muliana, A. "Creep Responses of Smart Sandwich Composites at Multiple Length Scales: Experiments and Modeling" ASME, J of Engineering Materials and Technology, JEMT, Vol. 133, pp. 1-6, 2011
11. Hasan, Z. and Muliana, A., "Analyzing Deformation and Failure of Smart Laminated Composites" Mechanics of Composite Materials, 48(4), pp. 391-404, 2012
12. Khan, K and Muliana, A., "Fully Coupled Heat Conduction and Deformation Analyses of Viscoelastic Composites" Composite Structures, 94(6), pp. 2025-2037, 2012
13. Muliana, A "The Effects of Residual Stresses and Degradation on the Response of Viscoplastic Functionally Graded Materials" Composite Structures, 11, pp. 3354-3363, 2012
14. Khan, KA and Muliana, A, "Fully Coupled Heat Conduction and Deformation Analyses in Viscoelastic Structures" Mechanics Time-dependent Materials, 16(4), pp. 461-489, 2012

15. Jeon J. and Muliana, A. "A Simplified Micromechanical Model for Analyzing Viscoelastic-Viscoplastic Response of Unidirectional Fiber Composites" ASME J Engineering Materials and Technology, 134, 031003, 2012
16. Gudlur, P, Forness, A., Lentz, J., Radovic, M., and Muliana, A. "Thermal and Mechanical Properties of Al/Al₂O₃ at Elevated Temperatures" Material Science and Engineering A, 531, pp. 18-27, 2012
17. Chaitanya, KRS, Muliana, A., and Rajagopal, KR, "Controlling Deformation in Linearly Elastic and Viscoelastic Structures due to Temperature and Moisture Changes using Piezoelectric Actuator" J. Intelligent Material Systems and Structures, 23(17) pp. 1949–1967, 2012
18. Jeon, J., Kim, J., and Muliana, AH, "Modeling Time-dependent and Inelastic Response of Fiber Reinforced Polymer Composites" Computational Material Science, 70, pp. 37-50, 2013
19. Sohrabi, A. and Muliana, AH, "Rate-dependent and Electro-mechanical Coupling Response of Ferroelectric Materials: A Finite Element Formulation" Mechanics of Materials (MOM), 62, pp. 44-59, 2013
20. Lin, CH and Muliana, AH, "Micromechanics Models for the Effective Nonlinear Electro-mechanical Responses of Piezoelectric Composites" Acta Mechanica, 224, pp. 1471–1492, 2013
21. Reddy, JN, Doshi, S., and Muliana, A., "Theoretical Formulations for Finite Element Models of Functionally Graded Beams with Piezoelectric Layers," Journal of Solid Mechanics, Vol. 3, No. 4, 2013
22. Gudlur, P, Muliana, A, and Radovic, M, "Thermo-mechanical Properties of Aluminum-Alumina Composites based on its Microstructural Characteristics," Composite Part B, 58C, pp. 534-543, 2014
23. Lin CH and Muliana A, "Micromechanical Models for the Effective Time-dependent and Nonlinear Electro-mechanical Responses of Piezoelectric Composites" Journal of Intelligent Material Systems and Structures, 25, pp. 1306-1322, 2014
24. Tajeddini V, Lin CH, Muliana AH, and Lévesque M, "Average Electro-mechanical Properties and Responses of Active Composites" Computational Material Science, 82, pp. 405-414, 2014
25. Jeon J, Muliana A, and La Saponara V, "Thermal Stress and Deformation Analyses in Fiber Reinforced Polymer Composites undergoing Heat Conduction and Mechanical Loading" Composite Structures, 111, pp. 31-44, 2014
26. Tajeddini V, Ben Attitalah H, Muliana A, and Ounaies Z, "Nonlinear viscoelastic behavior of active fiber composites", ASME Journal Engineering Materials and Technology, 136, p.021005, 2014
27. Gudlur P, Muliana A, and Radovic M, "The Effect of Microstructural Morphology on the Elastic, Inelastic, and Degradation Behaviors of Aluminum - Alumina Composites" Mechanics Research Communications, 57, pp. 49-56, 2014
28. Lin CH and Muliana A, "Polarization Switching Responses of 1-3 and 0-3 Active Composites" Composite Structures, 116, pp. 535-551, 2014

29. La Saponara V, Farrugia A, Lestari W, and Muliana A, "Analysis of ultrasonic waveforms from smart sandwich composite structures under creep bending at elevated temperature" Journal of Intelligent Material Systems and Structures, in press 2014
30. Ben-Atitallah H, Ounaies Z and Muliana AH, "A Parametric Study on Flexible Electro-Active Composites: Importance of Geometry and Matrix properties" Journal of Intelligent Material Systems and Structures, in press 2014
31. Lin CH and Muliana AH, "Nonlinear Electro-mechanical Responses of Functionally Graded Piezoelectric Beams," Composites Part B, in press 2014

Journal paper under review and preparation:

1. Sohrabi A and Muliana AH, "Nonlinear and Time-dependent Behaviors of Piezoelectric Materials and Structures," in review
2. Ben-Atitallah H, Ounaies Z and Muliana AH, "On the Temperature and Time-dependence of the Electro-mechanical Properties of Flexible Active Fiber Composites," in review
3. Xing J, Radovic M, and Muliana A, "Thermal Properties of BaTiO₃/Ag Composites at Different Temperatures" in preparation

Conference proceedings and abstract:

1. Khan, K.A, Gudlur, P., Barelo, R., Muliana, A.H., and Lévesque, M., "Heat Conduction and Thermal Stresses in Particulate Composites," Int. Congress on Thermal Stress, June 1-4, 2009 at the University of Illinois at Urbana-Champaign.
2. Muliana, A.H. and Li, K.A., "A Micromechanical Formulation for Active Fiber Composites with Field Coupling Effects," ASME International Mechanical Congress and Exposition, Orlando, FL, 2009
3. Ben Atitallah, H., Ounaies, Z., and Muliana, A., "Temperature and Time Effects in the Electro-mechanical Coupling Behavior of Active Fiber Composites" 16th US National Congress on Theoretical and Applied Mechanics, June 27 - July 2, 2010, State College, Pennsylvania, USA
4. Muliana, A., Li, KA, and Lin, CH, " A Multi-scale study for active fiber composites with field coupling effects," 9th World Congress on Computational Mechanics, July 19-23 2010, Sydney, Australia
5. Muliana, A. and Lin CH, "A micromechanical model for active polymer matrix composites," ASME International Mechanical Congress and Exposition, Nov 12-18 2010, Vancouver, CA
6. Farrugia, A., Winkelman, C., La Saponara, V., Kim, J.S. and Muliana, A. "Investigation on creep response of smart sandwich composite at multiple length scales," ASME International Mechanical Congress and Exposition, Nov 12-18 2010, Vancouver, CA
7. Forness, A., Gudlur, P., Muliana A, and Radovic M, "Thermomechanical Characterization of Al/Al₂O₃ Composites at Elevated Temperature" Undergraduate Student Research Grant Program, College of Engineering, Texas A&M University

8. Lin, CH and Muliana, A. "Analyzing Thermo-electro Mechanical Response of Active Composites" 26th ASC and 8th CANCOM, Montreal Canada, September 26-28 2011
9. Hasan, Z and Muliana, A. "Analysis and Control of Smart Composite Laminates using Piezoelectric Materials" 26th ASC and 8th CANCOM, Montreal Canada, September 26-28 2011
10. Ben Atitallah, H., Muliana, A., and Ounaies, Z., "Time-dependent Response of Active Composites with Thermal, Electrical, and Mechanical Coupling Effect" SPIE Smart Structures and Materials + Nondestructive Evaluation and Health Monitoring Proceeding, March 2011
11. Lin CH and Muliana A, "A Multi-scale Model for Analyzing Nonlinear Response of Active Composites," 16th International Conference on Composite Structures ICCS16, Porto, Portugal June 2011
12. Kim JS, Arronche L, Farrugia A, Muliana A, La Saponara, V, "Time-dependent Response of Smart Sandwich Composites," 16th International Conference on Composite Structures ICCS16, Porto, Portugal May 31-June 2 2011
13. Jeon J and Muliana A, "A Micromechanics Model for Viscoelastic-Viscoplastic Response of Polymer Fiber Composites," ASME Applied Mechanics and Materials Conference, McMat, Chicago Illinois May 31-June 2, 2011
14. Gudlur, P, Forness, A., Lentz, J., Radovic, M., and Muliana, A. "Thermal and Mechanical Properties of Al/Al₂O₂ at Elevated Temperatures," ASME Applied Mechanics and Materials Conference, McMat, Chicago Illinois May 31-June 2, 2011
15. Lin CH and Muliana A, "Micromechanics Model for Nonlinear Multi-field Response of Active Composites," ASME Applied Mechanics and Materials Conference, McMat, Chicago Illinois May 31-June 2, 2011
16. Ben Atitallah, H., Ounaies, Z., Khadimalla, A and Muliana, A "Parametric study on the geometry and matrix properties impact on the performance of the AFCs" SPIE Smart Structures and Materials + Nondestructive Evaluation and Health Monitoring Proceeding, March 2012
17. Khan KA and Muliana A, "A Multiscale Model for Fully Coupled Nonlinear Thermoviscoelastic Analyses of Particulate Composites," Mechanics of Nano, Micro and Macro Composite Structures Politecnico di Torino, 18-20 June 2012
18. Muliana A, "A Time-dependent Micromechanical Model of Ferroelectric Composites," Mechanics of Nano, Micro and Macro Composite Structures Politecnico di Torino, 18-20 June 2012
19. Sohrabi A and Muliana A, "The Time Dependent Behavior of Active Composite Beams," American Society for Composites 27th Technical Conference, 15th US-Japan Conference on Composite Materials, ASTM-D30 Meeting, October 1-3, 2012, Arlington, Texas
20. Lin CH and Muliana A, "Effective Nonlinear Responses of Piezoelectric Fibrous and Hybrid Composites" ASME 2012 International Mechanical Engineering Congress & Exposition (IMECE), Houston, 2012
21. Tajeddini V, Lin CH, Muliana A, and Levesque M, "The effect of Microstructural Morphologies on the Effective Electro-mechanical Properties of Piezoelectric Particle Composites," ASME 2012 International Mechanical Engineering Congress & Exposition (IMECE), Houston

22. Sohrabi A and Muliana A, "Finite Element Analysis for Nonlinear Time Dependent Response of Piezoelectric Materials" ASME 2012 International Mechanical Engineering Congress & Exposition (IMECE), Houston
23. Jeon J and Muliana, A "Time-dependent and Inelastic Response of Fiber Reinforced Polymer Composites" ASME 2012 International Mechanical Engineering Congress & Exposition (IMECE), Houston
24. Xing J, Jang A, Radovic M, and Muliana A, "Thermal properties of BaTiO₃/Ag Composites undergoing Phase Transformation due to Temperature Changes" American Society for Composites, 28th Technical Conference (ASC), September 9-11, 2013
25. Lin CH and Muliana A, "A Micromechanical Model for Analyzing Responses of A Piezoelectric Hybrid Composite" American Society for Composites, 28th Technical Conference (ASC), September 9-11, 2013
26. Sohrabi A and Muliana A, "Nonlinear Time Dependent Finite Element Analysis for Active Composites" American Society for Composites, 28th Technical Conference (ASC), September 9-11, 2013
27. Ben Atitallah, H., Ounaies, Z., and Muliana, A "Non-uniform electric field and nonlinear piezoelectric behavior in active fiber composites" American Society for Composites, 28th Technical Conference (ASC), September 9-11, 2013
28. Lin CH and Muliana A, "Rate-dependent Hysteretic Response of Electro-active Composites: A Micromechanical Analysis" 9th International Conference on Mechanics of Time Dependent Materials, Montreal CA, May 27th to 30th 2014
29. Sohrabi A and Muliana A, "Non Linear Time Dependent Responses of Ferroelectric Materials," 17th U. S. National Congress on Theoretical and Applied Mechanics, June 15-20, 2014 at Michigan State University, East Lansing, Michigan

6) List of participating scientific personnel

Principal Investigator: Anastasia Muliana

Graduate Students:

- a) Master students:
 - 1. Kuo-An Li
 - 2. Ramachandran Kuravi*
 - 3. Zeaid Hasan
 - 4. Sukanya Doshi
- b) PhD students:
 - 1. Kamran Khan
 - 2. Pradeep Gudlur*
 - 3. Jaehyeuk Jeon
 - 4. Chien-Hong Lin
 - 5. Hassene Ben Attitalah*
 - 6. Amir Sohrabi
 - 7. Vahid Tajeddini
 - 8. Junwei Xing*

* co-advised with other faculty members (Drs. Zoubeida Ounaies, Miladin Radovic, and KR Rajagopal) and partially supported by this AFSOR grant